基于编织结构的折展器械臂
刚柔转化机理与设计方法研究

Study on Rigid-flexible Transformation Mechanism and Design Method of a Deployable Manipulator Based on Braided Structure

一级学科：机械工程

研究方向：机械设计及理论

作者姓名：尚祖峰

指导教师：王树新　教授

天津大学机械工程学院

二〇二一年五月

摘要

自然腔道手术以人体腔道为入路，力求最小的切口和最少的组织损伤，具有更佳的治疗效果。为了通过曲折的人体腔道，手术中需采用细长的柔性器械完成相关操作。柔性器械刚度低，位姿锁定能力有限，力传递效果差，因而其操作力大小与操作精度难以保障。此外，手术器械的多功能性，涉及切割、止血、照明等，使其径向轮廓难以降低，在进入、撤出狭小体腔时容易造成组织损失，增加患者不适感。

采用具有可变直径、可变刚度的管状器械臂作为辅助工具，是解决上述问题的有效手段。器械臂的柔顺、小直径状态可方便其插入与撤出，而刚性、大直径状态可为后续器械提供稳固的大通路，对器械进行导引与支撑。现阶段，已有多种刚柔转化机制被提出并应用于器械臂设计中，包括丝张紧法、相变材料法、颗粒挤压法、负压摩擦法等，并取得了良好的变刚度效果。然而，上述器械臂自身轮廓尺寸不可调，因而仅解决了刚度问题，在进出人体时的尺寸干涉问题仍有待解决。

为同时解决器械臂设计上的刚度、尺度问题，本文以具有径向折展性能的编织管结构作为基体设计器械臂，提出基于负压的变刚度策略以及基于电热的双向变直径驱动设计；面向所设计器械臂潜在的失效模式，对其骨架力学性能、刚柔转化机理、直径变化能力等开展系统性分析；依据分析结果，提出器械臂的设计准则与操作方法，完成样机试制与演示实验。本文的主要研究内容如下：

面向器械臂应用，研究了编织管结构的力学行为特征。探究了几何及驱动力约束下的径向折展性能，得到了直径可达区间估计式。研究了弯曲垮塌行为，发现编织角度与编织丝股数为垮塌程度的关键影响因素，并进一步确定了保障完整截面轮廓的临界编织角度为 48.5 度。分析了轴向刚度，提出具有混合编织角度的编织模式，通过编织丝间相互干涉，其轴向刚度提升了 57.1%，具有更好的轮廓稳定性。

提出并研究了通过负压调控实现器械臂变刚度的控制方法。将密封膜包覆于编织管内外表面形成密封腔，施加负压将薄膜压紧于编织管表面以限制丝、膜间的相对运动，进而提升结构的刚度。实验结果表明，相比于柔态，器械臂在刚态下抗弯刚度提升至 6.85 倍，径向刚度提升至 3.90 倍。建立了丝-膜摩擦理论模型以及数值仿真模型，揭示了其刚柔转化机理与刚度提升机制，发现增加摩擦力及薄膜刚度是提升器械臂变刚度能力的最佳手段。

提出并研究了基于形状记忆材料的器械臂双向变直径的驱动方法。器械臂骨架在电热激励下展开至预设的大直径状态，自然冷却后在橡胶圈作用下回收至小

直径状态。实验结果表明该方法可用 20 秒实现 1.46 倍的直径转换比例。基于弹簧理论建立其组分间的交互受力模型，从理论上确定了直径变化范围。基于传热学原理对其热响应行为进行研究，发现使用前将器械臂预热至 37 摄氏度，响应时间可缩短至 10 秒以内。

试制了样机系统并进行演示实验。首先，提出编织式器械臂的设计准则，并据此设计、搭建了器械臂样机及其控制系统；提出了器械的刚度、尺度的耦合控制策略，使器械臂在术中无需持续通电。采用所开发的物理样机进行演示实验，体外模拟了包括插入、径向展开、刚化保形、软化折叠、撤出的完整操作流程，并对样机刚度、尺度指标进行对比分析，验证了该器械臂的可行性与有效性。

本文设计、分析并试制了一款基于编织结构的折展变刚度器械臂，验证了器械臂的可行性与有效性。所设计器械臂为解决柔性手术器械在刚度、尺度上的问题提供了新方法。

关键词：自然腔道手术，器械臂，编织管结构，可变刚度，可变直径，负压方法，形状记忆方法

ABSTRACT

Natural orifice transluminal endoscopic surgery (NOTES) novelly takes a body orifice as its operation channel. It strives for the smallest cut and the least tissue damage, thus having a better treatment effect. A slender, flexible surgical instrument is adopted to pass through the tortuous human body orifice in the operation. However, the low stiffness makes the instrument show low efficiency in shape locking and force transmission, thus causing problems in force capability and manipulation accuracy. In addition, the multiple functions to be integrated with including cutting, hemostasis and lighting make it difficult to reduce the radial size of the instrument. As a result, it is easy to cause tissue damage and increase patient discomfort during insertion and withdrawal via the narrow orifice.

Using a tubular manipulator with a tunable diameter and variable stiffness as an assistant device is an efficient solution to the problem. The flexible, small-diameter state of the manipulator can facilitate its insertion and withdrawal, while the rigid, large-diameter state can provide a path that is rigid and large enough to guide and support the following instrument. Up to now, a variety of tunable stiffness mechanisms have been proposed and applied in manipulator design, involving wire tensioning, phase change material, granular jamming, negative pressure friction, etc., which have achieved good tunable stiffness results. However, these manipulators have a non-tunable profile, which only satisfy the requirement for stiffness. They only solve the problem of stiffness, and the size interference during entering and leaving the human body is still unsolved.

To solve the problems in stiffness and size simultaneously, in this dissertation, a braided tube with great radial deployability is adopted as the basis to design the manipulator. A tunable stiffness method based on negative pressure as well as a bi-directional tunable diameter actuation design have been proposed. Considering the potential failure modes of the proposed manipulator, mechanical behaviors of the braided skeleton, the tunable stiffness and the tunable diameter of the manipulator have been systematically analyzed. Finally, based on the analytical results, design rule and workflow of the manipulator have been proposed, and prototype fabrication and demonstration experiment have been carried out. The main contents of this dissertation are as follows:

Mechanical characteristics of the braided tube have been analyzed for the application as manipulator skeleton. Deployability in radial direction of the tube under constraints of geometry and actuation force is firstly analyzed, and the equation to estimate the researchable diameter range has been derived. Bending collapse behavior is studied next, and it is found that the braiding angle and the fiber number are the key

parameters affecting the collapse behavior. It further declares that a bending angle less than 48.5 degree can guarantee an intact profile. Longitudinal stiffness is finally tested, and a new braiding configuration with a hybrid braiding angle has been proposed. Due to the interference between the braiding fibers, the longitudinal stiffness has been increased by 57.1% times compared with that of a normal one, allowing a better profile stability under longitudinal load.

A tunable-stiffness mechanism based on the braided tube and the negative pressure has been proposed and analyzed. Sealing membranes are dressed which cover both the inner and outer surfaces of the braided tube and form a sealed cavity. Negative pressure is applied to the membranes to restrict the relative sliding between the braiding fibers and the membranes and limit their deformations, thereby enhancing the overall stiffness. Experimental results show that the bending stiffness and the radial stiffness are respectively increased to 6.85 times and 3.90 times as those in the flexible state. A theoretical fiber-membrane interaction model and the numerical simulation models have been established, with which the stiffness enhancing mechanism is further declared. It finds that frictional condition and membrane stiffness are the most efficient in tuning the stiffening capability.

A bi-directional tunable-diameter method based on shape memory material has been proposed and analyzed. The skeleton deploys to the memorized shape and presents a large-diameter profile at electrical heating. When cooled it folds to a slim configuration under the compression of rubber bands. Experimental results show that it can achieve a diameter range up to 1.46 times within a response time of 20 seconds. Based on the spring theory, a mechanical model of the interaction between the components of the skeleton has been established, which theoretically determines the tunable diameter range. Based on heat-transfer analysis, heat-response behavior of the manipulator has been analyzed. It finds a preheating to 37 degrees Celsius can reduce the response time to be less than 10 seconds.

A prototype system is fabricated and put in a demonstration experiment. Design rules are firstly summarized, following which a prototype together with a control system is established. The workflow of the manipulator has been proposed, which integrates the tunable stiffness and tunable diameter mechanisms, making the manipulator still function at no electric current. A demonstration test has also been carried out, which simulates the operation processes of the manipulator in vitro, which involving insertion, deploying, stiffening, shape-locking, returning flexible and withdrawal. Together with the comparison of diameter and stiffness ranges between the prototype and the commercial endoscopes, it verifies the feasibility of the designed manipulator.

This dissertation designs, analyzes and fabricates a deployable tunable-stiffness manipulator based on a braided tube. The tunable-stiffness mechanism and tunable-diameter actuation method are revealed, and the feasibility and efficiency of the

manipulator are verified. The work provides a new idea for solving the problems of stiffness and size of flexible surgical instruments.

KEYWORDS： Natural orifice transluminal endoscopic surgery, surgical manipulator, braided tube, tunable stiffness, tunable diameter, negative pressure method, shape memory material

Contents

摘要 I
ABSTRACT III
Contents VII
List of Figures XI
List of Tables XV
Notation XVII
Chapter 1 Introduction 1
1.1 Background and Significance 1
1.2 Development of NOTES and Its Surgical Platforms 2
1.2.1 Development of NOTES 2
1.2.2 Development of Multi-tasking Platforms 3
1.3 Review of Tunable-stiffness Manipulators 5
1.3.1 Tendon Tension Method 6
1.3.2 Phase Change Material Method 6
1.3.3 Granular Jamming Method 8
1.3.4 Fluid Pressure Method 8
1.3.5 Other Cases 9
1.4 Braided Tube 10
1.4.1 Equations for Deployment 11
1.4.2 Deployment Actuation 13
1.4.3 Mechanical Analysis Review 14
1.4.4 Potential Failure Modes 15
1.5 Aim and Scope 17
1.6 Outline of Dissertation 17
Chapter 2 Mechanical Behaviors of the Braided Tube 19
2.1 Introduction 19
2.2 Deployability 19
2.2.1 Fabrication and Experiment 19
2.2.2 Numerical Model 21
2.2.3 Results 23
2.3 Bending Collapse 25
2.3.1 Experimental Setup and Numerical Model 25

2.3.2 Results.. 27
2.3.3 Effects of Structural Parameters 30
2.4 Hybrid Braiding 33
2.4.1 Concept and Mechanism of the Hybrid Braiding 33
2.4.2 Experimental Setup and Numerical Model.. 36
2.4.3 Results and Discussions... 37
2.5 Conclusion 42
Chapter 3 Tunable Stiffness Mechanism 43
3.1 Introduction... 43
3.2 Tunable Stiffness Design 43
3.3 Bending Stiffness 44
3.3.1 Experimental Setup and Numerical Model.. 44
3.3.2 Results.. 45
3.3.3 Theoretical Model... 48
3.3.4 Parametric Analysis 50
3.4 Radial Stiffness 53
3.4.1 Experimental Setup and Numerical Model.. 53
3.4.2 Results.. 55
3.4.3 Parametric Analysis 58
3.5 Conclusion 61
Chapter 4 Tunable Diameter Actuation 63
4.1 Introduction... 63
4.2 Tunable Diameter Design 63
4.3 Diameter Range 65
4.3.1 Theoretical Model... 65
4.3.2 Experimental Setup... 67
4.3.3 Results.. 67
4.4 Heat Response 69
4.4.1 Theoretical Model: steady state 70
4.4.2 Numerical Model 72
4.4.3 Experimental Setup... 73
4.4.4 Results.. 73
4.5 Conclusion 77
Chapter 5 Prototype and Performance Test 79
5.1 Introduction... 79

5.2 Prototype Fabrication 79
5.2.1 Parameter Design 79
5.2.2 Prototype Assembly 83
5.2.3 Workflow 84
5.3 Performance 85
5.3.1 Demonstration Test 85
5.3.2 Tunable properties 86
5.3.3 Discussions 88
5.4 Conclusion 89
Chapter 6 Achievements and Future Work 91
6.1 Main Achievements 91
6.2 Future Work 92
References 95
Appendix 105
中文大摘要 109
Publications and Research Projects during PhD’s Study 115
Acknowledgements 117

List of Figures

Figure 1-1 (a) EndoSAMURAI system and (b) its tip devices [40]. 4
Figure 1-2 Direct Drive Endoscopic System [42]...4
Figure 1-3 (a) Overview of the TJU platform, (b) control box, (c) tip devices and (d) working views in polypectomy [37]. 5
Figure 1-4 The variable neutral-line manipulator [45]. 6
Figure 1-5 Tunable stiffness manipulators using (a) low-melting-point alloy [47], (b) shape memory alloy (SMA) [50], thermoplastic polymers (c) totally [51] and (d) partly [52]. 7
Figure 1-6 Overall sketch of the granular jamming manipulator [59]......................8
Figure 1-7 Fluid-pressure based manipulators using (a) positive air pressure [61], (b) liquid pressure [62], negative air pressure through (c) friction [63] and (d) shape locking [65]. 9
Figure 1-8 Tunable-stiffness manipulators based on (a) multiple coaxial tubes [66] and (b) polyvinyl formal sponge [67]. 10
Figure 1-9 Geometry of the braided tube...11
Figure 1-10 (a) Deployability of the braided tube; (b) spreading of one fiber in plane; (c) relationship of the three distinct diameters.....................................12
Figure 1-11 Deformations of the braided tube at (a) longitudinal load and (b) radial load...13
Figure 1-12 Tunable-diameter mechanisms in stenting: (a) self-expandable stent [83] and (b) balloon-expandable stent [85]..14
Figure 1-13 Potential failure modes: (a) insufficient deployment, (b) bending collapse, (c) improper deployment, (d) large deflection, and (e) radial indentation. 16
Figure 2-1 Automatic braiding process of the braided tube. 20
Figure 2-2 Experimental stain-stress curves of the nylon fibers.............................20
Figure 2-3 Experimental setup for longitudinal tensile test...................................21
Figure 2-4 (a) The path of the braiding fibers on the cylindrical mandrel and its (b) side view; (c) crimp path of one braiding fiber [108]. 22
Figure 2-5 Numerical model of longitudinal tensile test. 23
Figure 2-6 Numerical configuration of the tensioned braided tube. 23
Figure 2-7 Outer diameter versus change of pitch curves. 24
Figure 2-8 Longitudinal force versus change of pitch curves.................................25

Figure 2-9 (a) Schema of the bending tester and (b) the experimental setup. 26
Figure 2-10 (a) Numerical model of bending test based on solid elements and (b) its boundary condition. 27
Figure 2-11 Bending angle versus profile height curves. 28
Figure 2-12 Experimental bent configuration at bending angles of (a) 57^{o} and (b) 150^{o}, and (c-d) the numerical ones. 28
Figure 2-13 Changes of the braiding angles in the collapsed profile. 29
Figure 2-14 Collapse process of the tube: (a) original state, (b) intact-profile state, (c) slightly collapsed and (d) completely collapsed states. 29
Figure 2-15 Bending configurations of (a) a normal braided tube, (b) a longer tube and (c) a fatter tube. 31
Figure 2-16 Effects of the braiding angle on collapse: profile height versus braiding angle curve. 33
Figure 2-17 Geometrical configurations of (a) uniform braided tube and (b) hybrid braided tube. 34
Figure 2-18 Units of (a) (b) uniform braided tubes with $\underline{\beta_1}$, $\underline{\beta_2}$, (c) hybrid braided tube, and (d)-(f) their deformed configurations at a longitudinal tensile ratio of 20%. 35
Figure 2-19 Experimental setup for longitudinal stiffness. 36
Figure 2-20 Force versus longitudinal displacement curves of the uniform and hybrid braided tubes. 38
Figure 2-21 Normal contact force (CNORMF) distributions of (a) uniform braided tube and (b) hybrid braided tube 2, and shear contact force (CSHEARF) distributions of (c) uniform braided tube and (d) hybrid braided tube 2 at a tensile ratio of 5%. 38
Figure 2-22 Mises stress distributions of (a) the uniform braided tube and (b) the hybrid braided tube 2 at a tensile ratio of 5%. 38
Figure 2-23 Effects of (a) hybrid ratio, (b) weighted average of braiding angle, (c) fiber number, (d) fiber diameter on the longitudinal stiffness of the hybrid braided tube. 40
Figure 2-24 Bending deformations of (a) uniform braided tube and (b) hybrid braided tube. 41
Figure 2-25 Effects of (a) weighted average of braiding angle and (b) hybrid ratio on the bending moment of the hybrid braided tube. 41
Figure 3-1 The tunable stiffness design of the manipulator. 43
Figure 3-2 Physical model of the tunable stiffness manipulator. 44
Figure 3-3 Numerical model of the manipulator bending. 45

Figure 3-4 Experimental bent configurations of (a) the manipulator and (b) the stand-alone braided tube, and the numerical ones of (c) the manipulator and (d) the stand-alone braided tube. 46
Figure 3-5 Moment versus bending angle curves of both the manipulator and the braided tube. 47
Figure 3-6 (a) Longitudinal and (b) circumferential strain contours of the outer membrane in bending simulation. 48
Figure 3-7 Geometry of the bent manipulator: (a) global bending of the manipulator; (b) cross section; (c) a single unit. 49
Figure 3-8 Effects of membrane stiffness and friction: (a) M_{30} versus E_m curves at different p; (b) M_{30} versus p curves at different E_m. 52
Figure 3-9 Effects of the properties of the braided skeleton: relationships between M_{30} and (a) E_f, (b) n, (c) β, (d) d. 53
Figure 3-10 (a) Experimental setup and (b) numerical model for radial stiffness test. 54
Figure 3-11 Experimental results: deformed configurations of (a) the stand-alone braided tube, (b) the manipulator, and (c) the welded braided tube; (d) reaction force versus indentation displacement curves. 55
Figure 3-12 Mises stress contours of the (a) stand-alone braided tube, (b) the braided skeleton in the manipulator, and (c) the welded braided tube; changes in braiding angle at intersection points in the (d) circumferential direction and (e) longitudinal direction for the stand-alone braided tube and the manipulator. 57
Figure 3-13 (a) Mises stress and (b) contact shear force contours of the inner membrane. 58
Figure 3-14 Effects of the braid parameters on the radial stiffness: (a) E_f, (b) d, (c) n and (d) β 59
Figure 3-15 Effects of (a) membrane stiffness and (b) friction on the radial stiffness. 60
Figure 4-1 Tunable diameter mechanism of the manipulator: (a) folding state and (b) deploying state. 63
Figure 4-2 Experimental specimen: (a) experimental strain-stress curves of the NiTi fibers at different electric currents; (b) physical model of the braided tube with tunable diameter. 65
Figure 4-3 Diameters of (a) fully deployed braided tube, (b) deployed skeleton and (c) folded skeleton. 66
Figure 4-4 Experimental setup for the tunable diameter. 67

Figure 4-5 Diameter range: experimental (a) maximum diameter and (b) minimum diameter; (c) theoretical relationships between the outer diameter and the radial load of the ring and tubes. 68
Figure 4-6 Effects of (a) the elasticity, (b) the distribution and (c) the circumference of the rubber band on the diameter range. 69
Figure 4-7 (a) Actual and (b) simplified profiles of the braiding fiber. 70
Figure 4-8 Diagram of the heat transfer on the braiding fiber profile. 70
Figure 4-9 Numerical model for the heat transfer. 73
Figure 4-10 Steady temperature in the braiding fiber profile: (a) theoretical temperature versus radial position curve; (b) numerical temperature distribution in the profile. 74
Figure 4-11 Electric current versus steady temperature curve. 74
Figure 4-12 Experimental response time determination: force versus time curve under tip load. 75
Figure 4-13 Heating time versus temperature curve. 75
Figure 4-14 Electric current versus response time curve. 76
Figure 4-15 Response time versus initial temperature curve at a constant electric current of 2A. 77
Figure 5-1 Relationship between the application requirements and design parameters of the manipulator. 82
Figure 5-2 Parameter determination process. 82
Figure 5-3 The manipulator prototype and its control system. 84
Figure 5-4 Control strategy of the manipulator with coupled tunable stiffness and tunable diameter. 85
Figure 5-5 The process of the demonstration test: (a) insertion of the manipulator; (b) slim state at negative pressure, (c) large-diameter state at negative pressure and (d) withdrawal of the manipulator. 86
Figure 5-6 The stiffness determination process of the manipulator. 87

List of Tables

Table 2-1 Geometrical parameters of the physical specimen for deployment analysis 21

Table 2-2 Parameters of the physical specimen for bending collapse test 26

Table 2-3 Orthogonal table for bending collapse analysis 31

Table 2-4 Calculation of the orthogonal test results 32

Table 2-5 F-examination results 32

Table 2-6 Parameters of the physical specimen in hybrid braid analysis....................36

Table 2-7 Parameters of the numerical models in hybrid braid analysis....................39

Table 3-1 Parameters of the physical specimen for bending stiffness experiment.....44

Table 3-2 Moments at a bending angle of 60^{o} of both the manipulator and the braided tube 46

Table 3-3 Parameters of the theoretical models for bending stiffness analysis..........51

Table 3-4 Skeleton parameters of the specimens for radial compression experiment53

Table 3-5 Energy distribution in the structures in radial compression experiment 56

Table 3-6 Parameters of the numerical models for radial stiffness 59

Table 4-1 Parameters of the physical model for tunable diameter 65

Table 4-2 Results of the diameter range 68

Table 4-3 Thermal parameters in the heat transfer simulation 73

Table 5-1 Parameters of the manipulator prototype 83

Table 5-2 Outer diameter of the existing devices 88

Notation

Parameters

b	Thickness of sealing membrane
c	Coil number of the helical fiber
cr	Rubber band circumference
d	Fiber diameter
d'	Inner diameter of the tubular fiber
d_c	Tubular coat outer diameter
d_i	Tubular coat inner diameter
$\mathrm{d}l$	Infinitesimal longitudinal length
$\mathrm{d}s$	Infinitesimal circumferential length
f	Friction between fibers and membrane on each unit area
f_{max}	The largest friction between fibers and membrane on each unit area
h	Coefficient of heat transfer
he	Height of the units in Figure 2-18
hr	Hybrid ratio
k	Curvature of a bent tube
k_{1j}	Average results at level 1 in Table 2-4
k_{2j}	Average results at level 2 in Table 2-4
l	Fiber length in uniform braided tube
l_1	Fiber length in one direction in hybrid braided tube
l_2	Fiber length in the other direction in hybrid braided tube
m	Number of the rubber bands
n	Fiber number
p	Negative pressure
pi	Pitch of the helical fiber
q	Heat flux
r	Radial position in braiding fiber
r'	Inner radius of the tubular fiber
r_c	Tubular coat outer radius
r_i	Tubular coat inner radius
r_p	Radius of the pulley in bending test

r_w	Radius of the transmission wire in bending test
$r(\psi)$	Crimp of braiding fiber as a sine wave
t	Temperature in braiding fiber
t_0	Room temperature
t_1	Temperature in tubular NiTi fiber
t_2	Temperature in tubular coat
v	Take-up speed of the mandrel
w	Width of the units in Figure 2-19
x, y, z	Coordinate of the node
C_1, C_2, C_3, C_4	Constants to be determined in heat transfer equations
D	Tube middle diameter
D_1	Diameter of fully deployed SMA braided tube
D_2	Diameter of the heated SMA skeleton
D_3	Diameter of the cooled SMA skeleton
D_b	Diameter of SMA skeleton
D_i	Tube inner diameter
D_o	Tube outer diameter
D_r	Diameter of rubber band
E_1	Young’s modulus of heated SMA fiber
E_2	Young’s modulus of cooled SMA fiber
E_f	Young's modulus of the braiding fiber
E_m	Young’s modulus of sealing membrane
EI_{braid}	Bending stiffness of the braided tube
E_t	Total energy stored in the manipulator
E_w	Rubber band elasticity
F	Longitudinal tensile force on the tube
F_j	F statistical result of j list
F_{wire}	Force on the transmission wire in bending test
G	Rigidity modulus of the fiber
H	Vertical distance between the two pulleys shown in Figure 2-9(a)
I	Electric current
I_f	Moment of inertia of the fiber
L	Tube length
M_{30}	Moments at a bending angle of 30^o

M_b	Bending moment on the tube
M_f	Bending moment on one helical fiber
M_m	Bending moment on the manipulator
N	Number of fiber segments highlighted in red in Figure 3-7(a)
P	Radial compression pressure on the tube
P_b	Radial pressure on SMA skeleton
P_r	Radial pressure from rubber bands
R	Radius of the tube
Ra	Difference the results at the two levels in Table 2-4
S_E	Variances of error list
S_j	Variances of j list
W	Work conducted by bending moment

Symbolic Variables

α	Shift angle between the fibers in the same direction
β	Braiding angle
β_0	Weighted average of braiding angle
β_1	Braiding angle in one direction in hybrid braided tube
β_2	Braiding angle in the other direction in hybrid braided tube
γ	Bending angle
ε_1	Strain in longitudinal direction
ε_1'	Critical longitudinal strain
ε_c	Strain in circumferential direction
ε_c'	Critical circumferential strain
θ	An angle shown in Figure 2-9(a)
ν	Electrical resistivity of the NiTi fiber
μ	Coefficient of friction
ρ	Radius of curvature in tube bending
λ	Heat conductivity coefficient
λ_1	Heat conductivity coefficient of NiTi fiber
λ_2	Heat conductivity coefficient of PTFE coat
ϕ	Heat generated in a NiTi fiber
ϕ_v	Heat generated in unit volume
φ	Circle angle shown in Figure 3-7(a)

ψ	Wrapping angle
ω	Angular speed of the bobbins

Abbreviations

ASGE	the American Society for Gastrointestinal Endoscopy
DOF	Degree of freedom
NiTi	Nickel- titanium
NOSCAR	Natural Orifice Surgery Consortium for Assessment and Research
NOTES	Natural orifice transluminal endoscopic surgery
PTFE	Poly tetra fluoroethylene
SAGES	the Society of American Gastrointestinal and Endoscopic Surgeons
SMA	Shape Memory Alloy

Chapter 1 Introduction

1.1 Background and Significance

Surgery is a medical method using specialized instrument to cure illness or injury of patients. In these years, its procedure develops steadily from laparotomy to multiple/single-site surgery, and finally to natural orifice transluminal endoscopic surgery (NOTES), which explains a new surgical procedure during which the instrument is inserted into body cavity via body orifices [1, 2]. In a traditional laparotomy, to make the organ presented in front of the doctor, a large wound has to be caused to the skin of the patient [3, 4]. One step forward, a multiple/single-site surgery only leaves one or several small incisions and thus reduces the suffering of the patient [5, 6]. This method has been widely used in clinic application at present. By comparison, a NOTES owns advantages involving no visible scars, low risk of infection, less postoperative pain, shorter hospitalization and earlier rehabilitation [7-10] by accessing the lesion via natural orifice with less trauma. The NOTES successfully carries forward the benefits of a multiple/single-site surgery, and is steping out of the laboratory into the clinic. A NOTES can assess the lesion via a transoral [11], transanal [12], transurethral, transgastric [13] or transvaginal [14] route. The multiple selections of routine also widen the applications of NOTES [10, 15].

Despite the great promise of NOTES [16], there are still technical challenges in the design of its instrument [17]. No matter which body orifice is selected, the routine is tortuous, long and narrow. The complicate geometrical conditions make conflicting requirements on stiffness and size of the instrument. To start with, the instrument has to be flexible enough [18] to adapt to the tortuous orifice, but the flexibility brings about difficulties in force transmission and shape-locking capability [8]. As a result, the motion precision and the force capability of the distal device are reduced, thus affecting the surgery result greatly [19, 20]. In addition, a surgical instrument should integrate with multiple functions such as energy, lighting, watering, cutting, suturing, and stapling [21]. Although the wire transmission system adopted helps save space [22], the channels to realize these functions make it difficult to reduce the instrument profile. The large profile size is not ideal [23, 24] which may generate tissue damage and discomfort to the patient during the insertion and withdrawal of the instrument.

To tackle the problems brought by the flexibility and size of the instrument, a snake-like manipulator with tunable stiffness [8] and tunable diameter is supposed to serve as an assistant device. Before the surgery, the manipulator should be flexible and slim to guarantee a safe insertion. When reaching the lesion, it deploys to a large-profile state and tunes its stiffness to a higher level. In this state, the manipulator provides a large-profiled, rigid path to accommodate and guide the following instrument, thus reducing the danger and discomfort during the instrument insertion. The surgical operation follows the insertion, during which the high stiffness of the manipulator helps support the instrument to improve the accuracy and force output. After the surgery, the manipulator returns to its slim, flexible state to ease its withdrawal.

Up to now, a variety of tunable stiffness mechanisms have been proposed and applied in manipulator design, involving wire tensioning, phase change material, particle extrusion, fluid pressure, etc., which have achieved good tunable stiffness results. However, these manipulators have a non-tunable profile. As a result, they just deal with the conflict in stiffness, remaining the conflict in size unsolved.

As a deployable structure, braided tube is able to tune its diameter dramatically and exert great flexibilty to adapt to the tortuous natural orifice. But, its stiffness is non-tunable and low. This dissertation aims at designing a deployable manipulator with tunable stiffness based on the braided tube to solve the conflicts of the surgical instrument in both stiffness and size.

1.2 Development of NOTES and Its Surgical Platforms

1.2.1 Development of NOTES

NOTES has been developing fastly since this decade, but its inspiration can be dated back to an endoscopic polypectomy case in 1955 [25]. The surgery was far from modern NOTES and a rigid endoscope was adopted. Next in 1973, a snare polypectomy on a sessile colonic polyp was reported [26]. Since the first success in endoscopic surgery, the technology of endoscopy has boomed and new methods and trials in different kinds of illness have been proposed [27]. In 2000, Kalloo et al [28] carried out the first NOTES case on a swine model, which validated the feasibility, efficacy and safety of the endoscopic transgastric approach. In 2002, this technology was successfully applied in clinical practice, which completed a kidney removal experiment on an animal via vagina [29]. A step forward in 2003, Rao and Reddy successfully removed the appendix of a male patient through a transgastric NOTES, which was the first NOTES procedure in humans [30]. Seeing the rapid progress and great promise of NOTES, in 2005, a working group named Natural Orifice Surgery Consortium for Assessment and Research (NOSCAR) was established by the Society of American Gastrointestinal and Endoscopic Surgeons (SAGES) and the American Society for Gastrointestinal Endoscopy (ASGE) [31]. This authoritative group works on the barriers, baselines and future plans of NOTES, and believes NOTES might represent the next major advancement in minimally invasive therapy [18]. Since then, NOTES has become a hot research topic and the work about it has increased dramatically. As of 2015, more than 1900 NOTES cholecystectomies in human and animal studies had been reported [27].

Researches on NOTES are also being carried out in China, and relevant publications started to appear in late 2000s. Zhu et al. performed a transumbilical endoscopic surgery for liver cysts in 2007 and completed 40 cases in total in the following two years [32]. In 2009, Hu et al. successfully performed a polypectomy on a male patient [33]. With the developing technology and experience in NOTES, more and more clinic cases have been reported. Wang had completed 180 rectal tumor cases through NOTES by 2016 [34], and Li had reported 564 peroral endoscopic myotomy cases by 2017 [35]. In 2018, Wang et al. used their independently developed surgical instrument with tunable stiffness on a swine model [36], and peformed a transesophageal gastric polyp resection experiment and a transenteral cholecystectomy experiment [37]. In 2020, Li et al. validated the feasibility of gallbladder exploration through a transgastric NOTES on swine models [38].

Up to now, most NOTES cases in humans were carried out via vagina because this route is well established for gynecologic operations, and the vaginal closure is easy to perform [39]. Transgastric access is also appealing because of its universal availability and acceptability to patients [39]. No matter which access is selected, the route is tortuous, long and narrow, and there are still technical barriers in instrument design, which holds back a wide application of NOTES. According to the White Paper released by NOSCAR [18], a manipulating platform is required which should exert good triangulation and stability and integrate with multiple functions [8].

1.2.2 Development of Multi-tasking Platforms

a) EndoSAMURAI

EndoSAMURAI was invented by Olympus Corporation, which has a working length of 103mm and presents a diameter of 15.7mm [40, 41]. Its main part is a long, flexible manipulator with two working arms running within it and connected to its tip. The devices are exchangeable, allowing the platform to be multi-functioned and complete different surgical tasks. In addition, a steerable overtube is designed on the manipulator, which improves the stability of the platform during surgery. The system is preferably operated by an active surgeon and a camera assistant. It has been put on a in vitro test and a in vivo study. The high leak pressure in the test and the performance in a transgastric small bowel resection surgery have verified the superiorities of the platform.

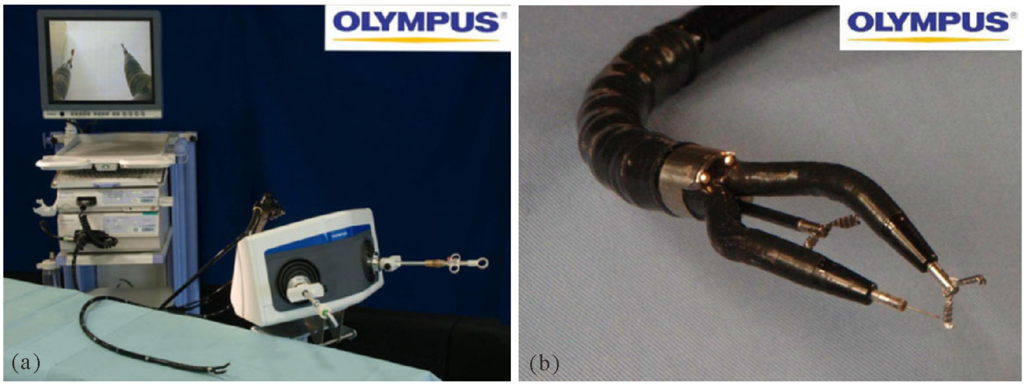

Figure 1-1 (a) EndoSAMURAI system and (b) its tip devices [40].

b) Direct Drive Endoscopic System (DDES)

This system was invented by Boston Scientific [42], which consists of a rail platform and a flexible sheath. The sheath is 55cm in length, 22mm in diameter, and has three channels for an endoscope and two instruments, whose diameters vary between 4mm and 6mm. It handles house mechanisms for force transmission, thus imparting five degrees of freedom (DOFs) to the tip instrument. In addition, the sheath has another two DOFs, making seven DOFs of the whole system in total. Similar to EndoSAMURAI, the acceptable instruments of DDES are interchangeable, widening the surgical functions of the platform. Its flexible sheath can also be locked into a desired posture. The platform can be managed by a single surgeon. The basic functionality of the DDES platform has been tested through an ex vivo study. Successful completion of tasks including suturing and knot tying has validated its promise.

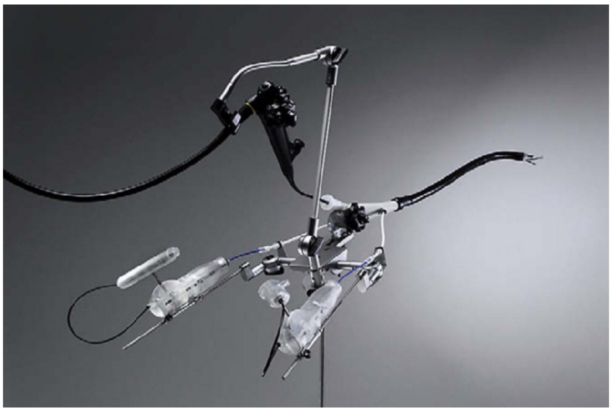

Figure 1-2 Direct Drive Endoscopic System [42].

c) Tianjin University (TJU) Platform

In 2018, a manual NOTES platform was invented by Tianjin University [37]. Its manipulator has two large channels for instruments and three small routes for light, water, gas or camera, which only presents an overall diameter of 20mm. What makes it significant is that the manipulator has a passively deformed proximal section and a transmission-wire-controlled distal end, which simplifies the control system greatly. In addition, it uses an adjustable scafflold to achieve a suitable posture of the platform. There is a mechanism at the manipulator tip which can tune the oriention of the instrument, thus widening the triangulation to a range of 60 degree. The platform has been put on an ex vivo experiments, in which cutting, grasping, suturing and tying functions have been successfully validated. Polypectomy and gallbladder removal surgerys have also been carried out through a transoral NOTES on a swine model.

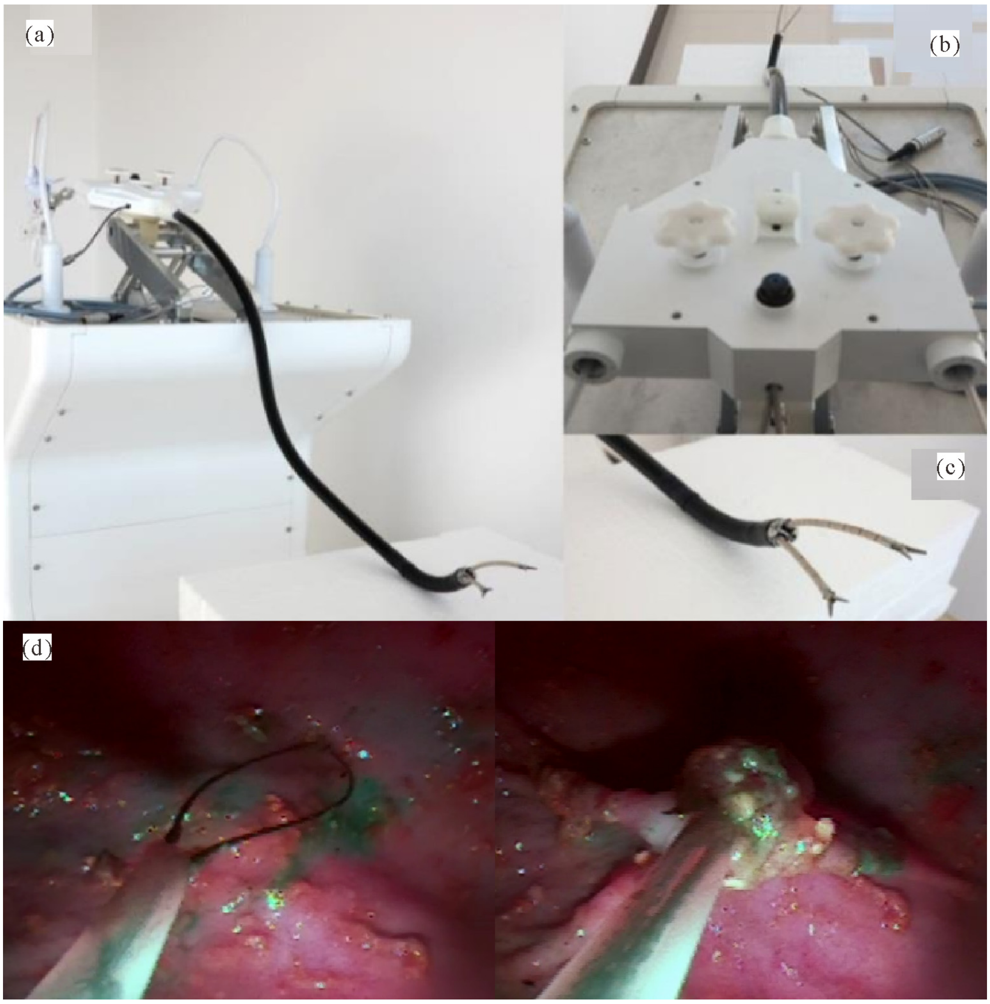

Figure 1-3 (a) Overview of the TJU platform, (b) control box, (c) tip devices and (d) working views in polypectomy [37].

1.3 Review of Tunable-stiffness Manipulators

Some NOTES platforms have integrated with steerable overtubes to improve the stability, but the locking capability is limited. Tubular manipulators with tunable stiffness are still needed and a series of designs have been proposed. The manipulators are reviewed in this subsection and classified according to the tunable stiffness mechanisms.

1.3.1 Tendon Tension Method

One method to tune the stiffness is based on controllable tension on tendons [43-46], and one example named variable neutral-line manipulator [45] is listed as shown in Figure 1-4. Its backbone is composed of a series of discrete links, which are passed through tendons. One end of each tendon is tied to the tip of the manipulator, and the other is driven by a motor. When the tendons are stressed, the discrete links are pressed together and the friction between the links restricts the overall deformation, thus increasing the stiffness. When the tendons are relaxed, the manipulator returns to the flexible state instantly. This method is easily controlled, providing a good stiffness ratio and a fast response. Nevertheless, high stiffness requires high tension, and the links need to be large enough to sustain the load, making it difficult to create a compact manipulator.

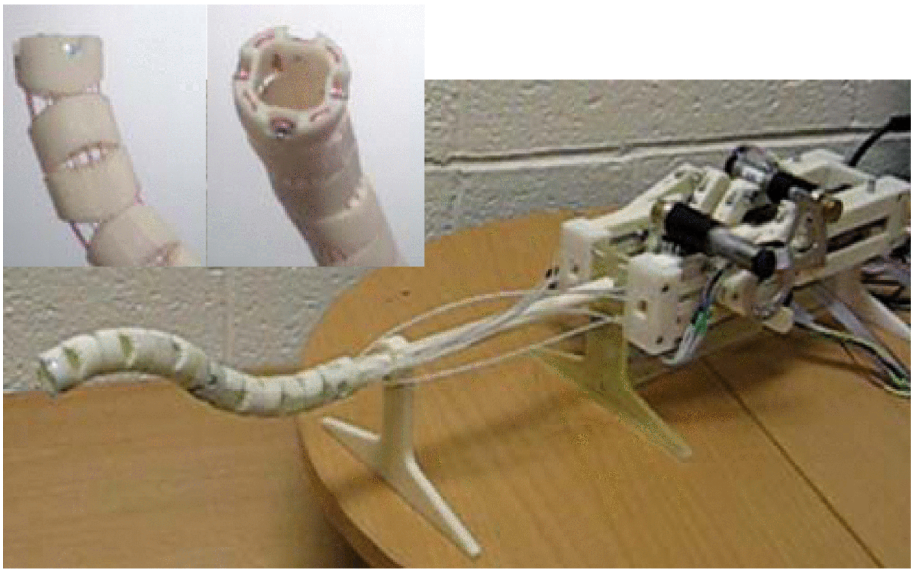

Figure 1-4 The variable neutral-line manipulator [45].

1.3.2 Phase Change Material Method

Phase change materials, with a Young's modulus varying greatly with temperature, present different stiffness states. Based on this superiority, materials such as low-melting-point alloy [47, 48], shape memory alloy (SMA) [49, 50] and thermoplastic polymers [51-54] have been applied in tunable stiffness manipulator design.

Figure 1-5(a) shows an application of low-melting-point alloy [47], which is filled in the inner chambers of the soft manipulator. The manipulator has another several channels for injection of hot or cold water to achieve heat transmission. The alloy is rigid and provides support in normal state, while it turns to be liquid when heated, making the manipulator very flexible. The low-melting-point alloy can achieve a very large stiffness ratio between the two phases, but it should be sealed carefully to avoid leakage, which may lead to manipulator failure and even safety problem.

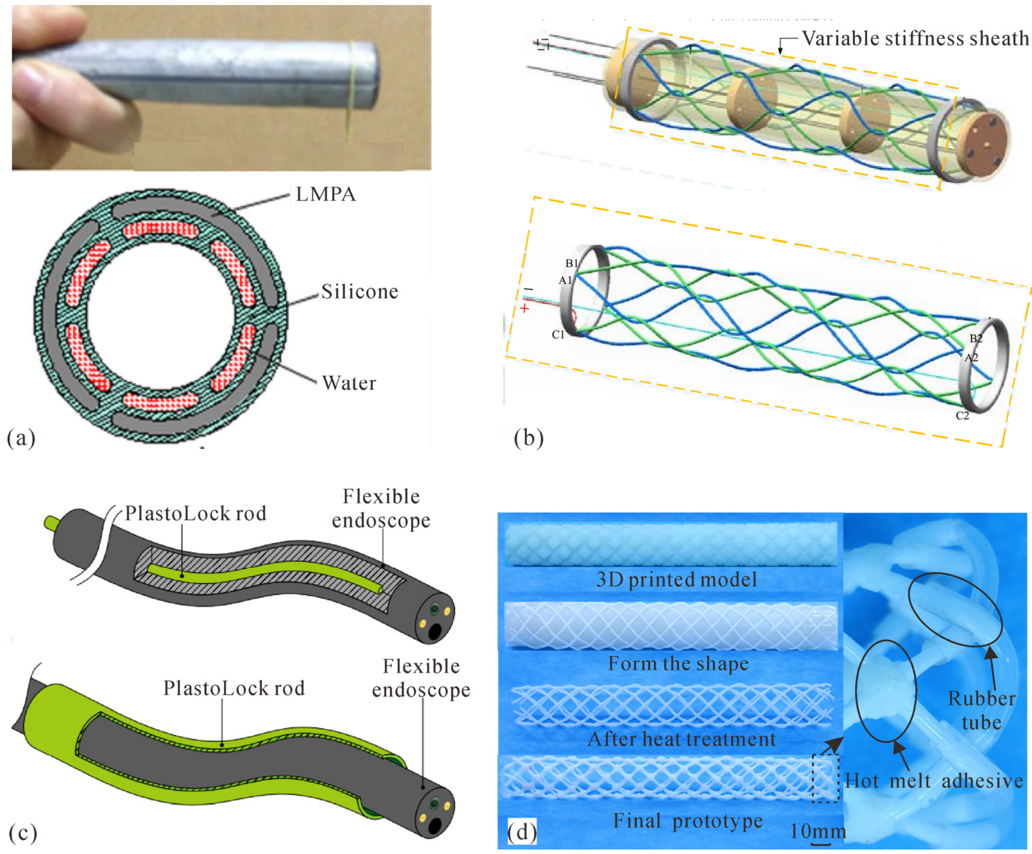

Figure 1-5 Tunable stiffness manipulators using (a) low-melting-point alloy [47], (b) shape memory alloy (SMA) [50], thermoplastic polymers (c) totally [51] and (d) partly [52].

Nickel-titanium (NiTi) material is a kind of shape memory alloy, which shows a moduli difference between austenitic and martensitic phases [50, 55]. A manipulator design case based on this is shown in Figure 1-5(b). Its backbone is a mesh structure formed with eight NiTi fibers [50]. The mesh configuration helps improve the flexibility in flexible state and makes it easy to be electrically charged. When the backbone is charged, the heated fibers get stiffer, so does the manipulator. However, the stiffness ratio between the rigid and the flexible states is only around 3.2, which is less efficient.

Thermoplastic polymer processes a tunable stiffness by transferring between glassy state and rubbery state at different temperatures. It has a much higher stiffness ratio than that of the SMA and does not flow in flexible state. A manipulator can be fabricated merely using thermoplastic polymer to realize tunable stiffness [51], which is shown in Figure 1-5(c). The substantial material is beneficial to a good load capacity in rigid state, but it takes more time to heat the whole structure. In contrast, Zhang et al. [52] uses thermoplastic polymer at finite intersections to speed up the stiffness tuning process, and the design is shown in Figure 1-5(d). The manipulator backbone is a braided tube fabricated with tubular fibers. The fibers not only serve as the load bearing, but also act as passage for cold and hot water. Hot melt adhesive at the intersections is heated or cooled by the injected water, and it restricts the relative motion of fibers differently, thus tuning the overall stiffness.

1.3.3 Granular Jamming Method

Jamming mechanism represents another stiffening method, which is based on a bag of granules [56, 57]. It is soft in normal state, whereas when negative pressure is applied, the granules jam together and improve the overall stiffness obviously. The mechanism has been widely applied in robotic gripper finger [58] and surgical manipulator [59, 60]. Taking a granular jamming manipulator [59] as an example, it has a stiffening channel, which presents a diameter of 8mm and is full of granules, and another there are three actuation chambers, which are driven by air pressure to bend the manipulator. Because the space in the manipulator is occupied by the channel and chambers, the instruments are installed on the tip. The biggest problem of this method is that the jamming part needs a large volume to stiffen, making it difficult to form a compact configuration. As a result, it presents an outer diameter of 30mm.

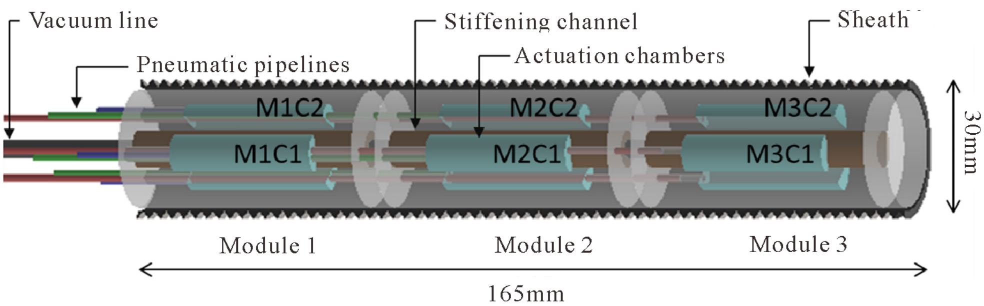

Figure 1-6 Overall sketch of the granular jamming manipulator [59].

1.3.4 Fluid Pressure Method

Fluid pressure adjustment is the most common method in stiffness tuning. A case using positive air pressure is the Slinder Linkage manipulator [61], which has a series of modules. There is a lock between two adjacent modules. The relative movement between the modules is locked when air pressure is applied, and returns unlocked when the pressure is removed. Positive pressure can also be acquired using water, and an example is “FORGUIDE” mechanism proposed by Arjo et al. [62]. It rigidifies due to the friction between a ring of cables, which are situated between a spring and an inflated tube actuated by water pressure. Compared with compressed air, water can provide a much higher pressure, thus providing a higher stiffness increment. However, the water takes up nearly all the inner space, leaving insufficient space for the following instruments. In addition, a positive pressure leaves a potential security risk.

In contrast, the negative air pressure method seems ideal because of its good safety and fast response [63-65]. In this kind of manipulator, there are discrete parts or links on its outer surface, which are sealed by membranes. When negative pressure is applied to the sealing cavity, the discrete components are pressed together tightly. The components get coupled with each other through friction [63, 64] or shape locking [65], thereby increasing the overall stiffness. When the pressure is cancelled, the components fall apart automatically, and the overall stiffness drops instantly.

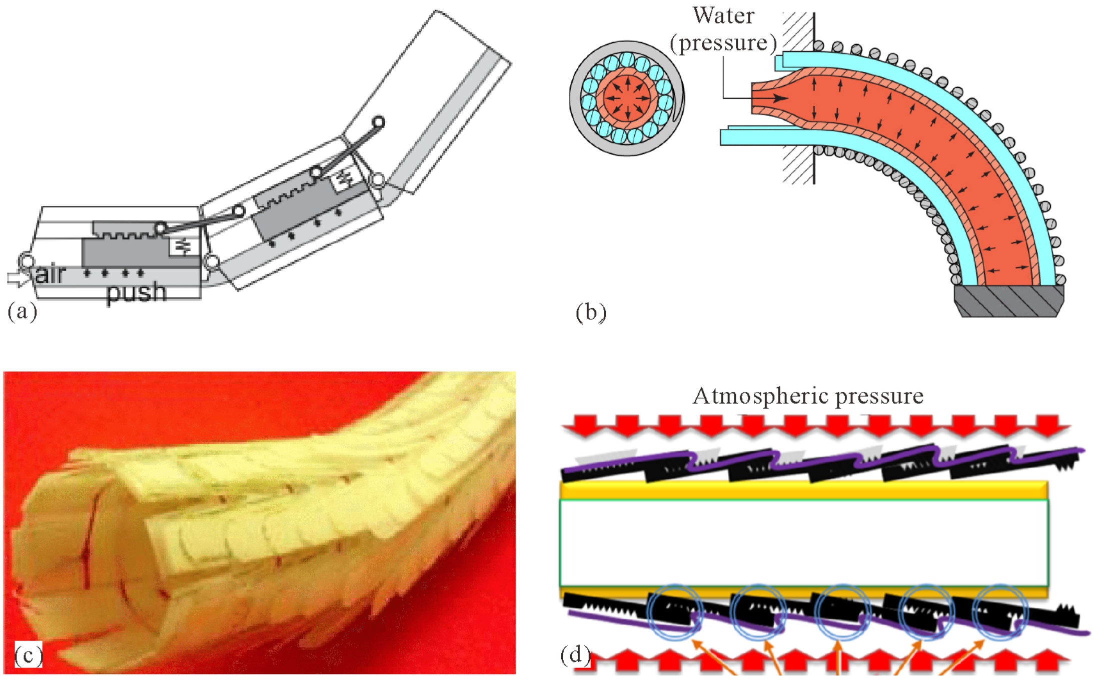

Figure 1-7 Fluid-pressure based manipulators using (a) positive air pressure [61], (b) liquid pressure [62], negative air pressure through (c) friction [63] and (d) shape locking [65].

1.3.5 Other Cases

An interesting case concerns a structural method [66]. The manipulator is composed of multiple coaxial tubes, each of which has several uneven through-hole patterns on its surface to obtain an anisotropic distribution of flexural stiffness along circumferential direction. Relative rotation and translation among the tubes can be adjusted, which causes a variable structural configuration, thereby tuning the overall bending stiffness.

Another case is a material-based solution [67]. Ren et al. designed a tubular manipulator, which uses polyvinyl formal sponge as the backbone material. It is embedded with a helical spring, which is to provide a radial stiffness to avoid structural collapse. The rigid sponge turns to be soft when gets wet and returns to rigid state when it is dry. Under the actuation of water vapor and compressed air, it can tune its stiffness quickly.

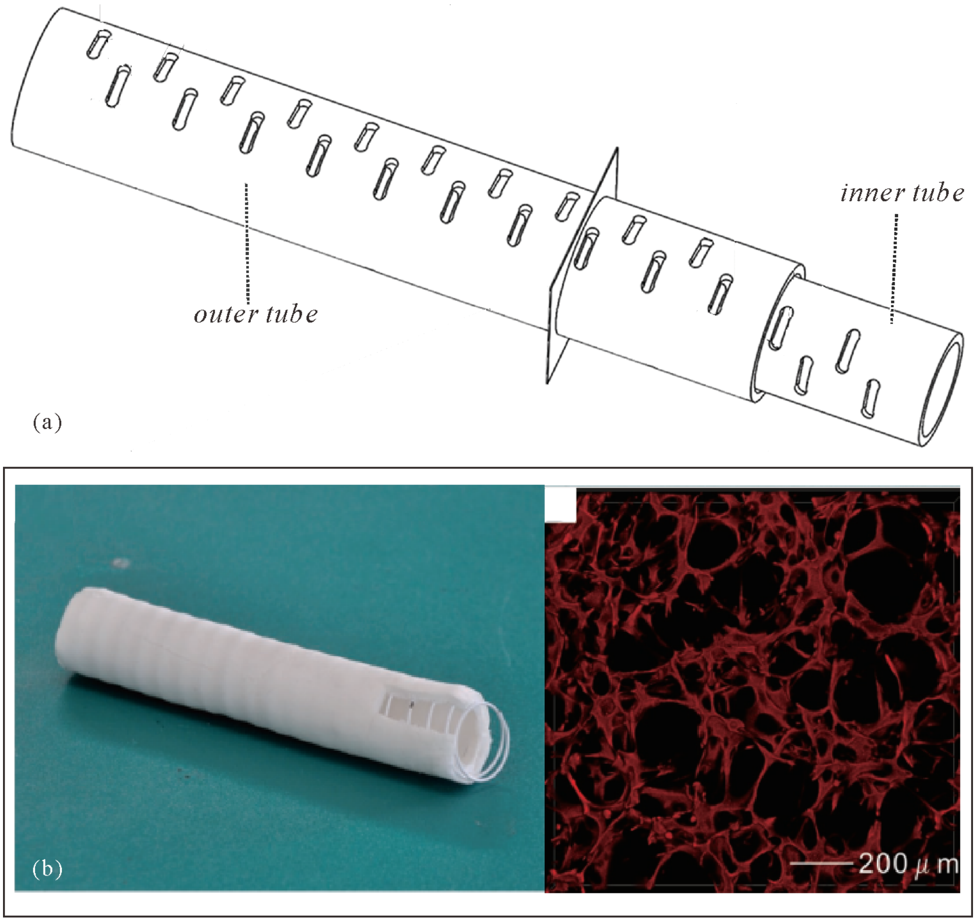

Figure 1-8 Tunable-stiffness manipulators based on (a) multiple coaxial tubes [66] and (b) polyvinyl formal sponge [67].

The efforts above have established a systematic framework for the tunable stiffness design of the manipulator. However, every manipulator presents a constant diameter and the other pair of conflict in manipulator design, that is, the size, has not been solved.

1.4 Braided Tube

Deployable structure, which can dramatically tune its size through varying its configuration [68], could provide a solution to the conflict in size. Especially, the braided tube, made of fibers interwoven in a crisscross pattern to form a tubular mesh configuration [69], can significantly vary its diameter when longitudinally tensioned and compressed. Geometry of the braided tube is shown in Figure 1-9. Thanks to the superior deployability, light weight, flexibility, fatigue resistance, and dimensional stability [70], it is widely used in engineering applications such as piping industry [71], [72], soft robotics [73, 74], smart materials [75, 76] and medicine [77, 78]. All these superiorities contribute to its great adaptability in vivo. If a delicate tunable stiffness capability is designed, the braided tube has a promise as the skeleton in a deployable manipulator.

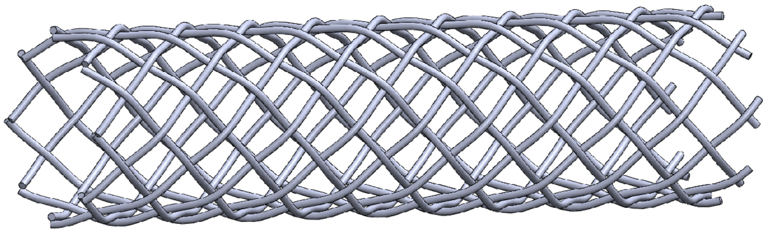

Figure 1-9 Geometry of the braided tube.

1.4.1 Equations for Deployment

Geometrical configuration of the braided tube is shown in Figure 1-10(a), which is determined by braiding angle β, tube middle diameter D, tube length L, diameter and number of fibers, d and n, respectively. In fact, a tube has three distinct diameters including middle diameter D, inner diameter D_i and outer diameter D_o, as shown in Figure 1-10(b). The middle diameter D is commonly used in calculation, whereas the other two are more related to fabrication. Their relationship is as

$$\begin{cases} D_{\mathrm{o}} = D + 2d \\ D_{\mathrm{i}} = D - 2d \end{cases} \tag{1-1}$$

Braiding angle is the helical angle of each braiding fiber. Compared with the helical angle of the traditional mechanical springs, the braiding angle is much larger, which contributes to the great deployability. Theoretical equations for the deployability were given by Jedwab and Clerc [79]. In their analysis, each braiding fiber is regarded as a helix, and its spreading in a plane is shown in Figure 1-10(c). Under a longitudinal or radial load, the tube length L and tube diameter D will change with the braiding angle. In the figure, it shows as a line rotates in the plane. Since the fiber is nearly inextensible, the fiber length can be considered unchanged during deformation and calculated by

$$\begin{aligned} &l = c\pi D / \cos\beta = c\pi D' / \cos\beta' \\ &c = L / pi = L' / pi' \end{aligned} \tag{1-2}$$

where c is the coil number of the helical fiber; pi is the pitch of the helical fibers, and the parameters of the deformed tube are denoted with a prime. Simplifying Eq. (1-2), the diameter and the length of the deformed tube can be acquired as

$$\begin{aligned} &D' = D\cos\beta' / \cos\beta \\ &L' = L\sin\beta' / \sin\beta \\ &pi' = pi\sin\beta' / \sin\beta \end{aligned} \tag{1-3}$$

During deformation, β' theoretically ranges between 0 degree and 90 degree. At a large β' approximate to 90 degree, the fibers huddle together, and the tube enters a slim state with a middle diameter about 2*d*. When β' tends to 0 degree, the tube middle diameter approaches to its upper limit $D/\cos\beta$. Thus, the reachable diameter of a braided tube can be theoretically estimated as $2d \sim D/\cos\beta$.

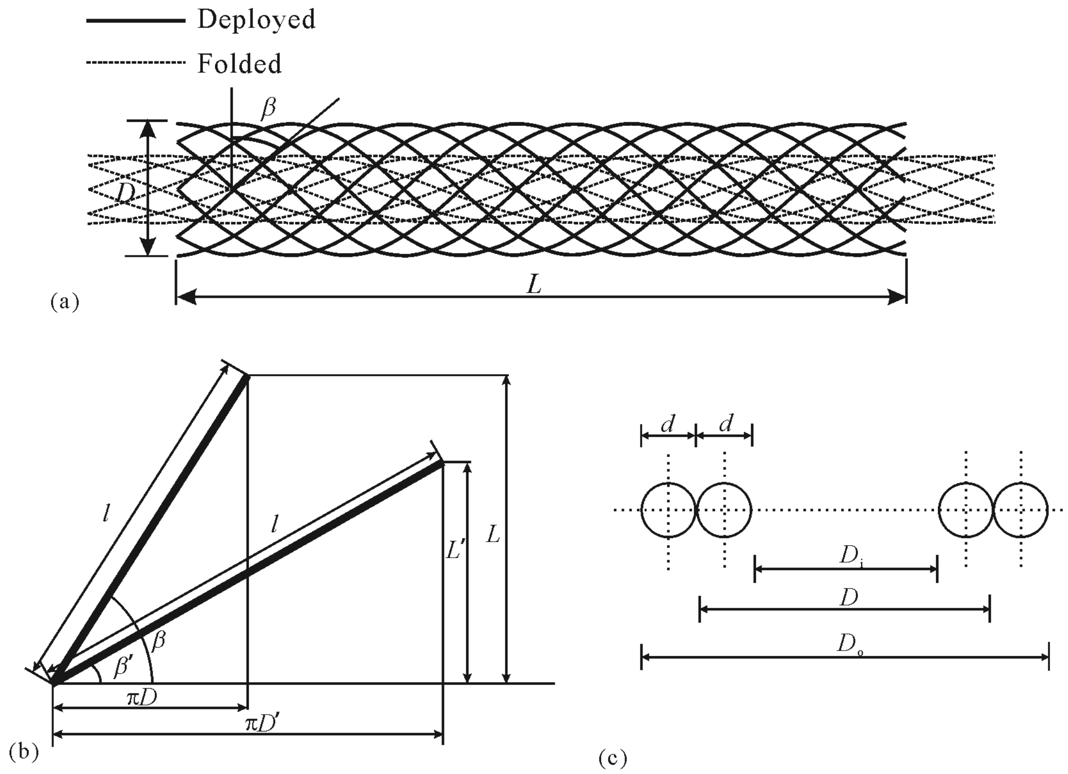

Figure 1-10 (a) Deployability of the braided tube; (b) spreading of one fiber in plane; (c) relationship of the three distinct diameters.

Longitudinal tensile force and radial compression pressure can fold the braided tube as Figure 1-11 shows. In contrast, longitudinal compression force and radial expanding pressure can deploy the tube. The foldability and deployability are both related to the variable diameter, and the forces to fold or deploy a braided tube were also concerned by Jedwab and Clerc [79]. They found that the longitudinal and radial forces are equivalent and both can fold/deploy a tube. The braided tube can be simplified as a combination of helical springs under the condition that the springs possess large indices *D/d*. Based on the spring theory proposed by Wahl [80], the longitudinal and radial forces on the tube can be calculated as

$$\begin{aligned} F &= 2n\left[\frac{2GI}{K_3}\left(\frac{2\sin\beta'}{K_3}-K_1\right)-\frac{E_f I_f \tan\beta'}{K_3}\left(\frac{2\cos\beta'}{K_3}-K_2\right)\right] \\ P &= \frac{2Fc}{D'L'\tan\beta} \end{aligned} \tag{1-4}$$

where $K_1 = \dfrac{\sin 2\beta}{D}$, $K_2 = \dfrac{2\cos^2\beta}{D}$, $K_3 = \dfrac{D}{\cos\beta}$, F is longitudinal force, P is radial uniform pressure, G, E_f, and I are the rigidity modulus, Young's modulus and the moment of inertia of the fiber, respectively.

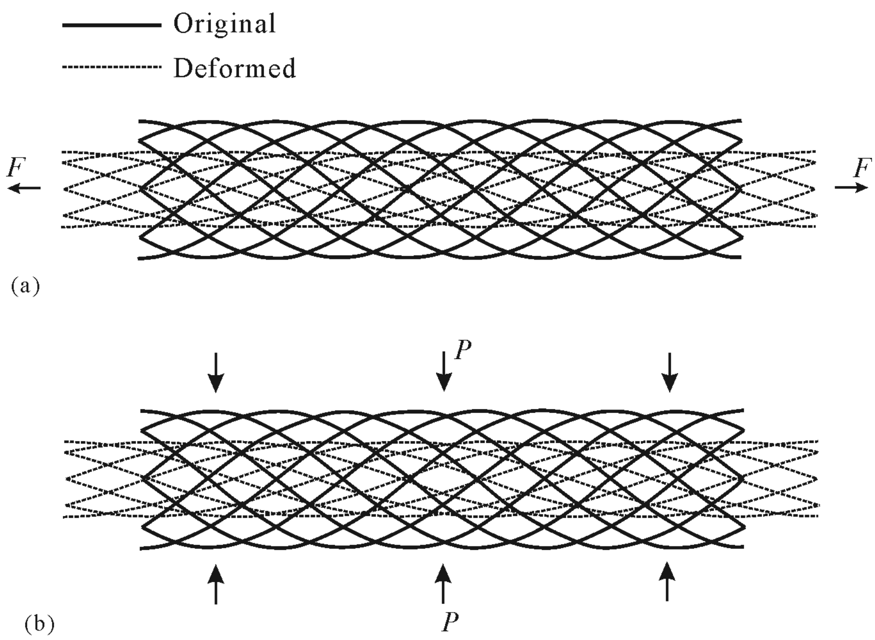

Figure 1-11 Deformations of the braided tube at (a) longitudinal load and (b) radial load.

1.4.2 Deployment Actuation

The deployability enables the tube to successfully pass through a narrow orifice in a compact configuration whereas deploy to function later. With this property, it has been widely used as a medical stent to cure aortic stenosis. In the stenting process, a compact stent is first transferred to the lesion with a delivery system and then deployed to restore the blood flow. Based on the deployment mechanism, a stent can be classified as either self- or balloon- expandable one [68].

The self-expandable stent is fabricated with NiTi alloy, which has great superelasticity to sustain large deformation. In the stenting process, the stent is first compressed into a guide tube and inserted into the body. When it arrives the lesion, the stent is released from the guide tube and deploys automatically [81-83]. In contrast, a balloon-expandable stent deploys passively. Before the delivery procedure, a foldable balloon is set in the stent in advance. When it reaches the delivery site, the balloon is inflated to plastically deform the stent [84, 85].

In stenting, the stent is supposed to be left in the blood vessels permanently, and no withdrawal is needed. Therefore, both methods are for deploying a stent, which completes a transformation from a small-diameter state to a large-diameter state.

However, in NOTES, the manipulator also needs to fold to a compact configuration for withdrawal. As a result, both methods are not applicable to the braided manipulator here. A new bidirectional tunable-diameter actuation method is needed.

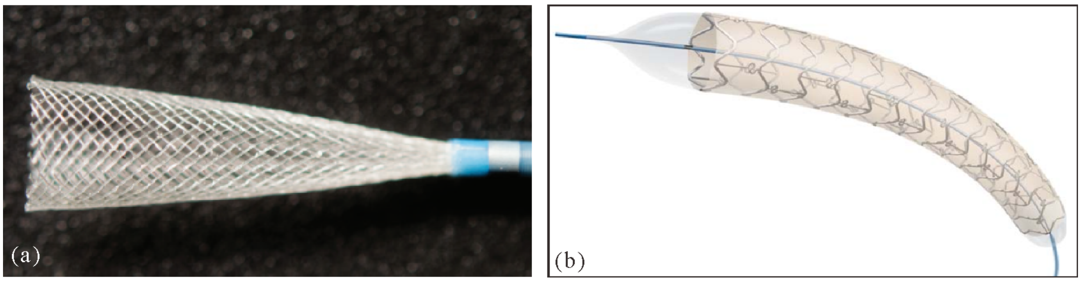

Figure 1-12 Tunable-diameter mechanisms in stenting: (a) self-expandable stent [83] and (b) balloon-expandable stent [85].

1.4.3 Mechanical Analysis Review

a) Basic mechanical behaviors

Deployability is the most distinct property of the braided tube, and it has been detailedly analyzed by Jedwab and Clerc [79]. In their analysis, each fiber is regarded as a helix. By spreading a helical fiber in a plane, the radial and longitudinal behaviors are found to be coupled, and the theoretical relationship between the diameter and the length is given. The diameter range can also be estimated with the theory. In addition, based on the spring theory proposed by Wahl [80], theoretical models for the radial and longitudinal stiffness were also derived. However, it has been found that the theoretical formula does not work when the diameter of the fiber is too large [86]. The stiffness has also been experimentally analyzed by other researchers. Wang et al. has developed a testing method to characterize the mechanical response of the tube subjected to internal or external pressure [87], which eliminates friction greatly and provides accurate results.

Bending flexibility has also been widely concerned by researchers. With the finite element method, the deployment of the braided tube at a bent configuration was successfully modelled [88-90]. It is proved to be able to achieve a large curvature bending. Kim et al. numerically analyzed the bending collapse behavior of the tube [91]. It has been found that the tube may collapse at some configurations, and this is most strongly influenced by the braiding angle and the fiber number. Bending stiffness was also numerically studied by establishing a calendar beam model [92]. The results show that the fiber diameter, the fiber number and the braiding angle affect the bending stiffness greatly. Also, bending fatigue was experimentally investigated by Xue et al. [93], and "four yarn crossover-based" deformation modes were proposed to reveal its energy absorption mechanism and fatigue life.

b) Application-based analysis

Some analyses about the braided tube are strongly related to the application environment. First is about the longitudinal migration of the tube caused by radial load. In stenting, a mathematical model considering the interaction between the stent and the esophageal was established to estimate the migration [94], and end shape of the tube was designed to release it [78, 95]. In contrast, in braided crawling robots, the migration was utilized by designing the gait to exceed its movement [96, 97]. Another case was also found in stenting, which replaces the open ends with looped ones to reduce the risk of tissue trauma [98]. The deformation of the new design was numerically investigated and compared with that of the ordinary one, and the accuracy of the stiffness equations proposed by Jedwab and Clerc [79] was analyzed. The braided tube can also be used as the cover of the pneumatic muscle actuator. It can act as a contractor or an extensor explained by the maximum volume theory [99].

c) New configurations

Some new configurations of the braided tube were proposed to make them function better in stenting. The first case is fully covered stent [100], which is an ordinary braided tube coupled with a tubular membrane on its surface. Its mechanical properties were analyzed, and theoretical models were proposed to predict its stiffness [101]. It was found that the membrane helps block off the mesh and improve the overall stiffness, but the tunable diameter ratio is reduced. If the stent fibers are coated with an elastomer of poly, a coated stent can be acquired, whose mechanical stiffness is between those of the ordinary stent and the fully covered stent [102]. Dual-layer braided tube was also used in application, which is formed with two similar braided tubes [103]. It was numerically observed that an increase in the wire number has larger effect on the overall flexibility. A braided tube can also be designed with different braiding angles at different longitudinal positions. This design was proposed by Ni et al. [104], which can meet the stiffness requirement and shorten the longitudinal elongation simultaneously.

1.4.4 Potential Failure Modes

Based on the working condition of NOTES and mechanical properties of the braided tube, the potential failure modes of the braided tube when acting as the manipulator skeleton are summarized as follows.

The first one is related to the tunable diameter range. The manipulator should present a slim profile during insertion and withdrawal to avoid tissue damage and reduce patient discomfort. However, in the working stage, if the manipulator does not have a wide diameter range, i.e., the manipulator cannot deploy sufficiently, its outline will not be large enough to contain the following surgical instruments, as shown in Figure 1-13(a). As a result, the instruments cannot be successfully inserted into body cavity via the manipulator.

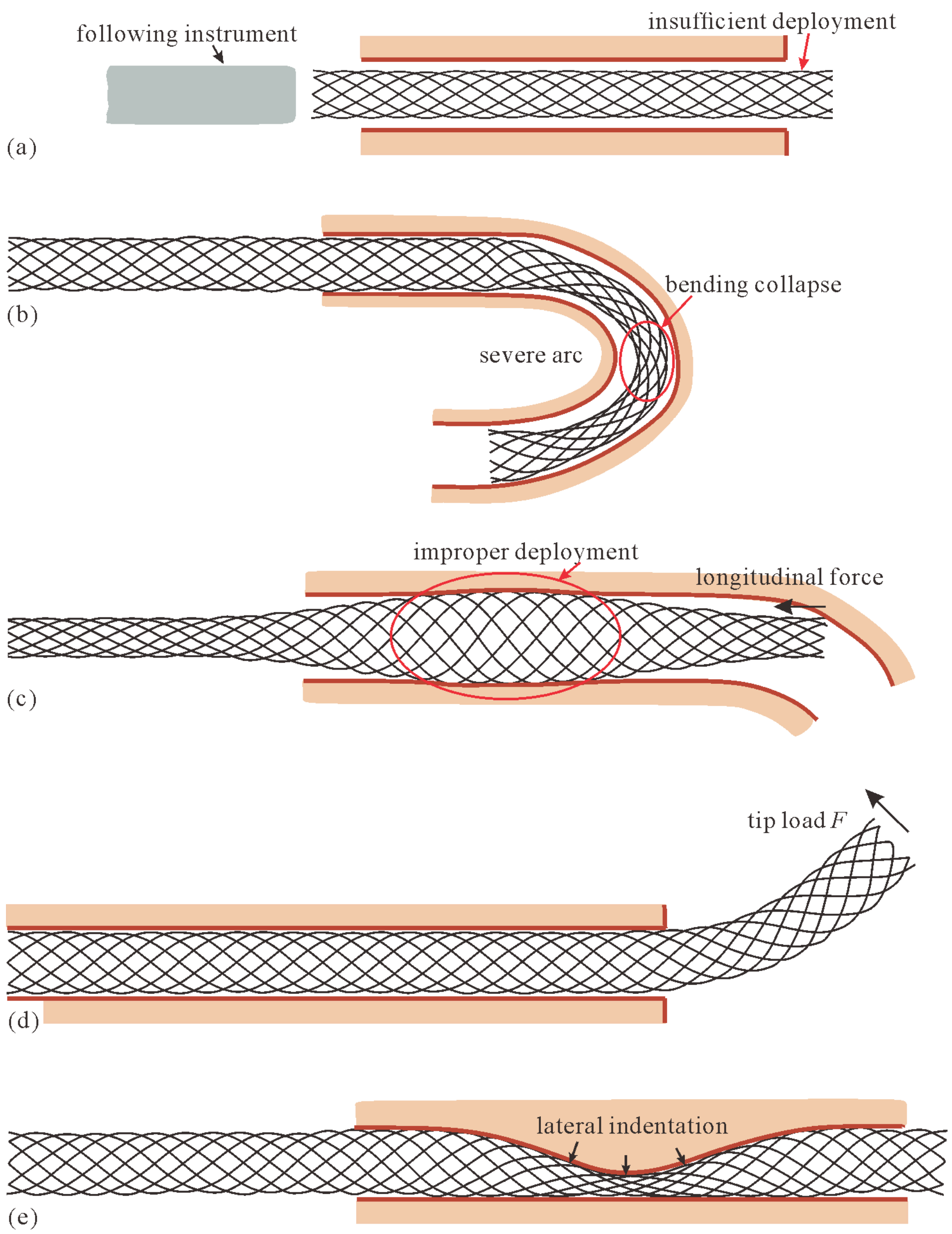

Figure 1-13 Potential failure modes: (a) insufficient deployment, (b) bending collapse, (c) improper deployment, (d) large deflection, and (e) radial indentation.

The second one is about bending flexibility. The natural route is usually tortuous, and the manipulator has to bend severely to follow the path. Thus, the braided tube should have an ideal configuration to avoid bending collapse, as shown in Figure 1-13(b), and provide an intact profile.

Thirdly, the braided tube should exert a good longitudinal stiffness to avoid improper deployment. The manipulator skeleton will meet longitudinal load while knocking on the wall of the body orifice during insertion, especially at a corner, as shown in Figure 1-13(c). If the longitudinal stiffness is too low, the tube will deploy and exhibit a larger diameter. The improper deployment will add additional insertion difficulty and patient discomfort.

The last two failure modes are caused by a lack of stiffness in rigid state. The manipulator is to provide support and maintain the spatial orientation of the surgical instrument [105]. If the bending stiffness is insufficient, there will be a large deflection at the tip of the instrument as shown in Figure 1-14(d), causing problems in accuracy and force output. In addition, the body orifice is not at an ideal tubular configuration, which may have narrow parts. Taking esophageal as an example, it has several normal constrictions along its route [106], which can cause local indentation to the manipulator, as shown in Figure 1-14(e). As a result, the manipulator also needs to present a sufficient radial stiffness to guarantee an intact passageway.

These potential failure modes may make the manipulator function improperly, or even lose efficacy completely. Mechanical analyses of the skeleton and the manipulator are required to avoid the failures.

1.5 Aim and Scope

This work is to design a surgical manipulator based on the braided tube, which has tunable stiffness to support the following flexible instruments and tunable diameter to ease the insertion and withdrawal processes. On the basis of the actuation design proposed and the mechanical analysis conducted, its design rule and control method will be summarized.

In this process, the mechanical analysis of the braided tube is conducted to optimize its performance as the manipulator skeleton at the first beginning. Furthermore, a tunable stiffness mechanism based on negative pressure is proposed, whose bending stiffness and radial stiffness in both rigid and flexible states are studied to widen the tunable stiffness range. Besides, a diameter actuation method using shape memory alloy is proposed to tune the radial size of the manipulator in double directions. Eventually, based on the acquired results, design rule of the manipulator is proposed, and a prototype is developed and put into demonstration test to validate the feasibility.

1.6 Outline of Dissertation

This dissertation consists of six chapters, which are outlined as follows.

Chapter 2 is devoted to the mechanical analysis of the braided manipulator skeleton. At first, deployability under the constraints of geometry and actuation force is studied, and the reachable diameter range is acquired. Next, bending collapse mechanism is explored. The vital parameter on the collapse behavior is found and its critical value to guarantee a basically intact profile is determined. At last, to deal with the improper deployment, a new hybrid braiding configuration is put forward, and its increased longitudinal stiffness is explained by geometrical analysis.

As for Chapter 3, design and analysis of a tunable stiffness mechanism are mentioned. The tunable stiffness mechanism realized through controllable fiber-membrane friction is introduced. The analysis work firstly concerns the bending stiffness. Numerical and experimental analyses are proceeded to explore the deformation mechanisms of the braided skeleton and the membranes. In light of the mechanisms, a membrane-fiber interaction model is established, and an explicit formula is formed to theoretically calculate the bending stiffness. Next, the radial stiffness range is studied with numerical and experimental methods. Distributions of stress, energy density and friction are focused to reveal the radial stiffness enhancing mechanism. A parametric analysis based on the numerical models also shows the effects of the parameters.

Chapter 4 focuses on the bi-directional tunable diameter actuation method using electrical heating. After the tunable diameter range is experimentally determined, a theoretical model based on the helical spring theory is also proposed to estimate the diameter range. With the model, a parametric analysis is made towards the setup of the rubber bands. In this process, heat response of the skeleton needs to be noticed. Distributions of the steady and transient temperatures on the braiding fiber profile are analyzed theoretically and numerically. With comparison between the temperature on the NiTi fiber and the phase-transition temperature, the applicable electric current range and the response time are determined.

The fabrication and characterization of the manipulator prototype are discussed in Chapter 5. It is noted that the relationships between design parameters and property requirement are decoupled, in this regard, a design rule of the braided manipulator has been proposed. According to this rule, a manipulator prototype together with its control system is then fabricated. Workflow of the manipulator is also proposed to couple the tunable stiffness and the tunable diameter actuations. Next, the prototype is put into an in vitro demonstration experiment, which imitates the whole surgical procedure. Together with the quantitative analysis of the tunable properties, the test result verifies the feasibility of the manipulator design.

The main achievements of the research, together with suggestions for future work, are summarized in Chapter 6, which conclude this dissertation.

Chapter 2 Mechanical Behaviors of the Braided Tube

2.1 Introduction

The braided tube is supposed to act as the manipulator skeleton, and its mechanical behaviors are strongly related to the potential failure modes such as insufficient deployment, bending collapse and improper deployment. This chapter focuses on the mechanical analysis of the braided tube. It illustrates the reachable diameter range, conducts a collapse behavior analysis, and proposes a hybrid braiding pattern to cure the three failure modes listed above.

The layout of this chapter is unfolded as follows. Section 2.2 intends to make an analysis of the tube deployment, during which the reachable diameter range is analyzed. Section 2.3 numerically analyzes the effects of design parameters on the bending behavior and gives a critical value of the vital parameter to avoid collapse. In Section 2.4, a hybrid braiding pattern is proposed, which utilizes different braiding angles to enhance the longitudinal stiffness. The conclusion is finally made in Section 2.5.

2.2 Deployability

To swallow the following instrument, the tube should have great deployability and exert a wide diameter range. Considering the fact that the deployability and the foldability are equivalent, in this sub-section, tensile test is conducted to capture the deployability of the braided tube. Experimental setup and numerical modelling are detailedly introduced at first. Based on the analytical results, the reachable diameter range is then determined.

2.2.1 Fabrication and Experiment

A braided tube specimen was fabricated using a braiding machine. Figure 2-1 shows a running braiding process on the machine. With the mandrel moving in longitudinal direction, two groups of bobbins, eight in each group, rotate around the mandrel in clockwise and anticlockwise directions, respectively, to weave the fibers into a braid on the surface of the mandrel. The inner diameter of the tube is determined by the mandrel diameter. The braiding angle β is determined by the take-up speed of the mandrel v and angular speed of the bobbins ω through

$$\beta=\arctan(2v / \omega D) \tag{2-1}$$

In practice, the braiding angle can be controlled with the take-up speed only.

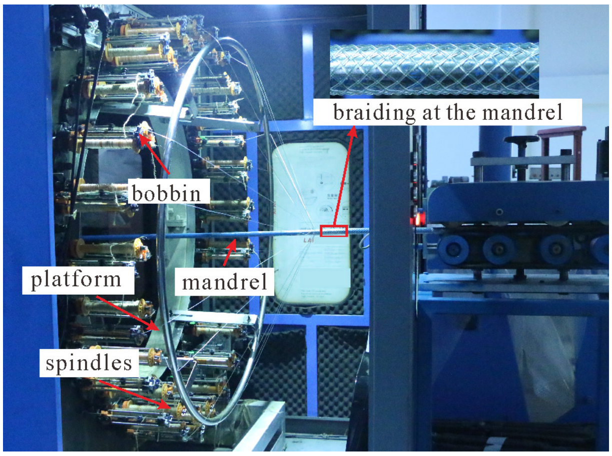

Figure 2-1 Automatic braiding process of the braided tube.

Nylon fiber was selected as the braiding fiber, which has a suitable stiffness and is easily available. Tensile behavior of the fiber was tested on an Insron 5982 testing machine. The tested fiber had a diameter of 0.50mm and a length of 50mm. It was tested three times and the results are presented in Figure 2-2. It can be seen that the results of the three tests show great consistency, and the linear stage is observed within a strain of 1.6%. Using the linear stage results, linear fittings were conducted to calculate the Young's modulus, and the average result is 3498.6Mpa.

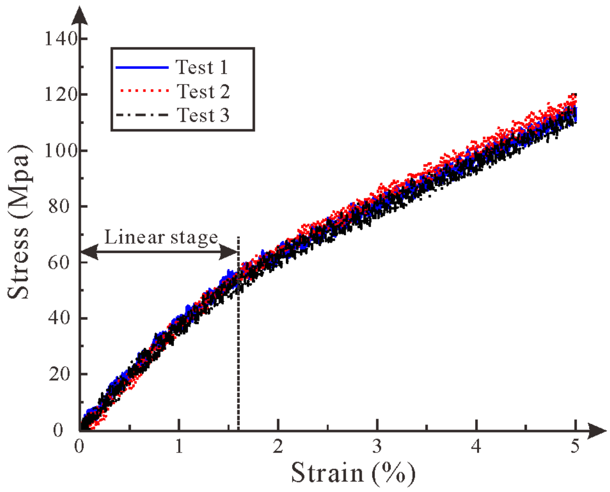

Figure 2-2 Experimental stain-stress curves of the nylon fibers.

In the braiding process, tension force from the bobbins was loaded on the fibers and caused stress. Thus, when the tube was removed from the braiding machine, it was fixed on the mandrel, and a heat treatment at 100^{o}C was conducted to help fix the shape and release the stress, thus creating a stable structure. The parameters of the tube specimen used in the deployment analysis are listed in Table 2-1.

Table 2-1 Geometrical parameters of the physical specimen for deployment analysis

Parameter	Value
Tube length, L	150.00mm
Tube outer diameter, D_o	21.45mm
Fiber number, n	16
Fiber diameter, d	1.07mm
Braiding angle, β	55.47°

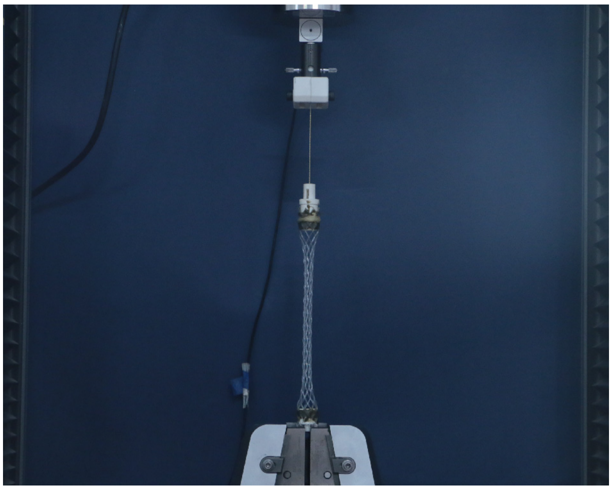

Figure 2-3 Experimental setup for longitudinal tensile test.

The longitudinal tensile test was conducted on the Instron 5982 testing machine, and the experimental setup is as Figure 2-3 shows. Each end of the tube was glued to a block for a good installation. At the large tube length, the effects of the glued ends on the deformation at the longitudinal middle part are ignorable, and thus the test can capture the deformation of a tube with free ends. The lower block was fixed with a clamp and the upper block was tied to a movable force sensor through a transmission wire. The sensor moved upwards at a constant speed of 10 mm/min, and the displacement was 20 mm. The tensile force during the loading process was exported automatically and the loading process was recorded with a high-resolution camera.

2.2.2 Numerical Model

Abaqus/Explicit [107] was used as the solver to simulate the tensile loading process of the braided tube. The first step of the modelling process was to determine the track of the braiding fibers. The fiber is not a perfect helix and it has to cross others at the intersections. This is the biggest challenge in the generation of the geometrical model. With the method introduced by Alpyildiz [108] (shown in Figure 2-4), a sinusoidal disturbance was added to the helices in the radial direction so as to stagger the fibers at the intersections. In this way, the equation for the fibers can be established as

$$\begin{cases} r(\psi) = \dfrac{d}{2}(\sin\dfrac{2\pi}{\alpha}\psi + \dfrac{3}{2}\pi) \\ x = (R + r(\psi))\cos(-\psi - (i-1)\alpha),\ i = 1, 2 \ldots n \\ y = (R + r(\psi))\sin(-\psi - (i-1)\alpha) \\ z = R\psi \tan\beta \end{cases} \tag{2-2}$$

where R is the radius of the tube; α is the shift angle between the braiding fibers moving in the same direction; ψ is wrapping angle; $r(\psi)$ is the crimp of braiding fiber as a sine wave.

(a)

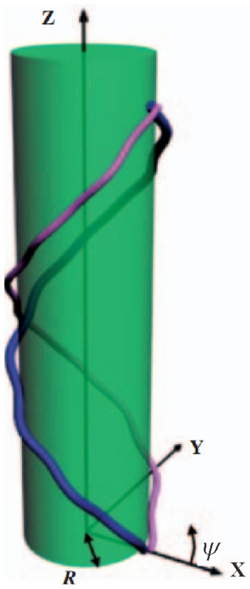

(b)

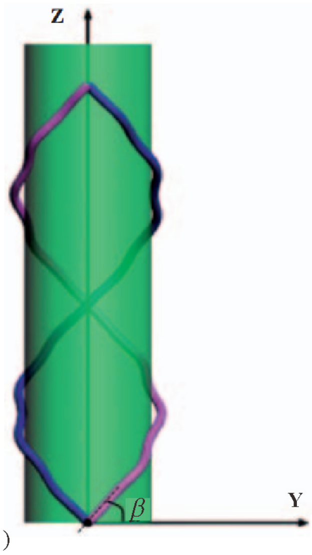

(c)

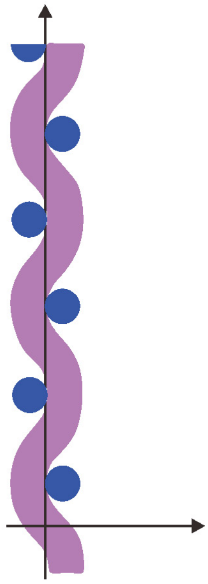

Figure 2-4 (a) The path of the braiding fibers on the cylindrical mandrel and its (b) side view; (c) crimp path of one braiding fiber [108].

The second step was to establish the numerical model in software *Abaqus*, and the modelling strategy was cited from Zheng [109]. Based on Eq. (2-2) and a mesh size, number and coordinate of the nodes and elements of the braided tube could be acquired in software *MATLAB* and then exported into a *txt* document. With the information of the nodes and elements, an orphan mesh part [110] was established and imported into *Abaqus*. In this way, the geometrical model of the braided tube was successfully generated in *Abaqus*. Considering the small diameter and long path of the braiding fiber, beam element *B31* was used to mesh the tube to improve the calculation efficiency.

Thirdly, boundary condition and other necessary settings were made to simulate the tensile loading process. The nodes at the two ends of the braided tube were respectively tied to two reference points, *Rp1* and *Rp2*, as rigid bodies. In this way, loads and boundary conditions could be easily applied to the tube via the reference points. In this case, all DOFs except the longitudinal displacement one of the two points were fixed. The two points moved away from each other at the same rate. Smooth amplitude definition built in *Abaqus* was adopted to control the tensile procedure. Hard contact was used to model the normal behavior and penalty was selected as the friction formulation to capture the tangential behavior. Poisson's ratio was cited from reference [111] and set as 0.28. Other parameters were the same as those in Table 2-1.

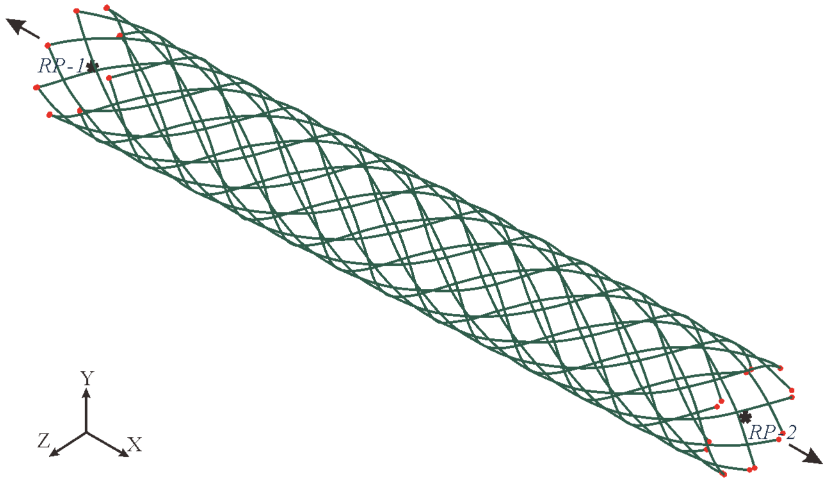

Figure 2-5 Numerical model of longitudinal tensile test.

Mesh size of 0.2mm and step time of 0.1s were determined through convergence tests. The diameter and the pitch of the tube as well as the force on the reference points were exported to characterize the mechanical responses.

2.2.3 Results

Numerical deformed configuration of the tube is presented in Figure 2-6. It can be seen that the middle part suffers from more deformation than the two tube ends. In both experiment and simulation, the tube ends are rigid and not deformable, which leads to the inconsistent configurations along the longitudinal direction. This boundary effect does not exist in manipulator application and is also not considered in the theoretical model. To make the tensile results meaningful and comparable, uniform configurations in the middle part of the experimental and numerical model are taken into account. The diameters and pitches in the following analysis were measured using experimental video and exported from numerical results, as shown in Figure 2-6.

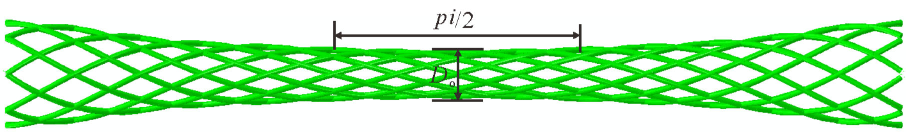

Figure 2-6 Numerical configuration of the tensioned braided tube.

Geometry is firstly emphasized, and the relationships between the outer diameter and the change of pitch are presented in Figure 2-7. The curves match well and show almost linear relationships. According to the experimental curve, the tube presents a maximum outer diameter of 21.45mm and a minimum of 12.42mm during the loading process. The diameter ratio between the two is 1.73. As a matter of fact, the original braiding angle of the tested tube is relatively large, which is about 55.47°. Therefore, the original outer diameter is far from its upper limit. If a longitudinal compression is applied to the tube, it can easily get an outer diameter of 34.93 mm. The theoretical maximum diameter is 37.84 mm. The error between the two is only 7.7%, and the maximum diameter can be basically estimated with the theoretical equation.

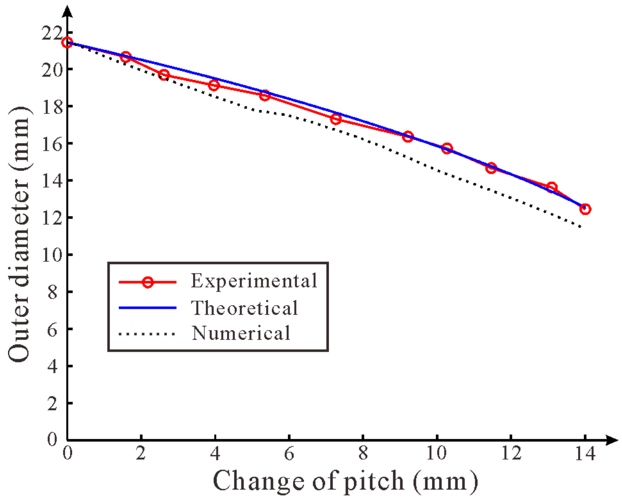

Figure 2-7 Outer diameter versus change of pitch curves.

The tensile force used to fold the tube is then analyzed, and the results are presented in Figure 2-8. The three curves match well, manifesting the same tendency. They are almost linear at the early stage and increase sharply at a larger displacement along with the increasing pitch. At a larger pitch, the fibers are more oriented to the loading direction and the tube has a higher load carrying capability. Though the theoretical equation gives the minimum diameter as $4d$=4.28mm, the higher actuation force reduces the feasibility. In this case, when the pitch increases by 14mm, the braiding angle reaches 68.3°. Thus, $D\cos 68.3^{\circ}/\cos\beta = 0.37D/\cos\beta$ can be used to estimate the minimum diameter.

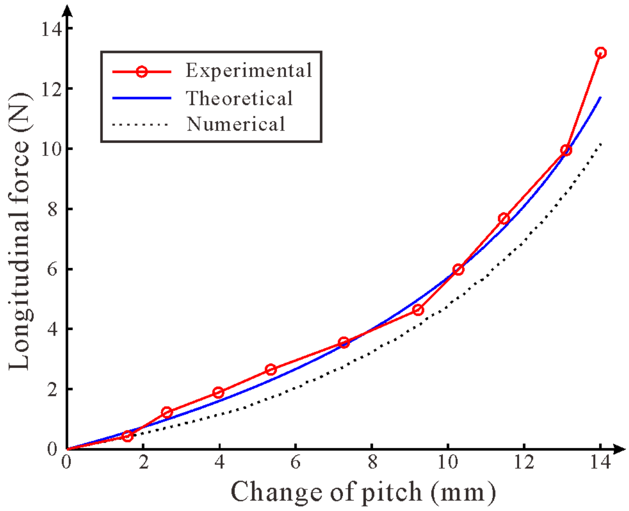

Figure 2-8 Longitudinal force versus change of pitch curves.

2.3 Bending Collapse

In flexible state, the braided skeleton dominates the overall mechanical behavior of the manipulator. During the insertion process, the flexible manipulator will meet severe curves of the natural route and its skeleton may collapse under bending, reducing the radial size. In this section, the bending collapse deformation of the tube and the effects of the design parameters are analyzed.

2.3.1 Experimental Setup and Numerical Model

Pure bending was applied to a physical specimen to evaluate the bending collapse behavior. A braided tube specimen was fabricated with the method introduced in Section 2.2.2, and the parameters are listed in Table 2-2. The bending tester was designed as Simons and Shockey [112] introduced, and its schema is presented in Figure 2-9(a). The transmission wire denoted by the dotted line in the figure is oriented by four fixed pulleys. When the wire was pulled horizontally, a pure moment would be applied to the holder and transmitted to the tested specimen. The moment can be calculated as

$$M = F_{\mathrm{wire}}[\frac{H}{\sin\theta}\sin(\theta+\gamma/2)+2(r_{\mathrm{p}}+r_{\mathrm{w}})] \tag{2-3}$$

where F_{wire} is the force on the transmission wire; H is the vertical distance between the two pulleys; θ is the angle shown in the figure; r_{p} and r_{w} are the radius of the pulley and the transmission wire, respectively.

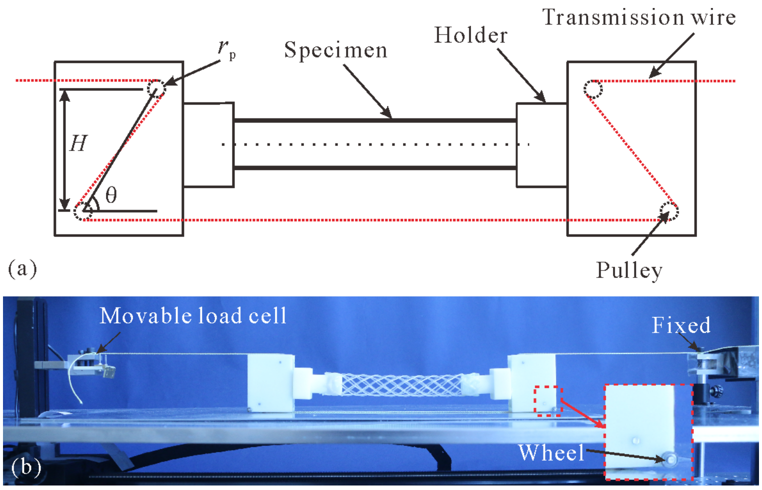

Figure 2-9 (a) Schema of the bending tester and (b) the experimental setup.

Table 2-2 Parameters of the physical specimen for bending collapse test

Parameter	Value
Tube length, L	100mm
Tube diameter, D	19.46mm
Fiber number, n	16
Fiber diameter, d	0.8mm
Braiding angle, β	52.43°
Young's modulus of the fibers, E_f	3498.6Mpa

The experimental setup is illustrated in Figure 2-9(b). The bending tester was put on a flat platform. Both ends of the specimen were fixed on the bending tester. One end of the transmission wire which passed through the bending tester was fixed, and the other was connected to a moveable load cell. Wheels were installed at the corners of the tester for free moving on the platform. Displacement control was applied in the experiments and the loading rate was 0.3mm/s.

A numerical model was then established. In *Abaqus* analysis, thickness of beam elements is obligated to be reduced, resulting in geometrical inaccuracy especially at a large deformation, such as severe bending. To solve the problem, solid element was used, and the profile of the braiding fibers was drawn in the pre-procedure *SolidWorks*. The modelling strategy was as follows. Based on Eq. (2-2), coordinate of the nodes of the braided tube was acquired in *MATLAB* and then imported into *SolidWorks* as curves. Secondly, a circular profile was drawn and swept along each curve to obtain the solid of the tube. And the tube was imported and meshed in *Abaqus* as Figure 2-10(a) shows. Mesh size along the fiber length was 0.2mm, and twelve nodes along the fiber circumference were set to trace the circular outline. Both ends of the fibers were tied to two reference points as rigid bodies, respectively. To bend a braided tube, longitudinal displacement DOF of each point was set free, whereas one rotational DOF along the radial direction of the tube was controlled as shown in Figure 2-10(b). All other DOFs of the two reference points were fixed. Rotation angle of each reference point was 75°. The profile height at the longitudinal middle point and the rotation angle of reference point *Rp1* were exported separately.

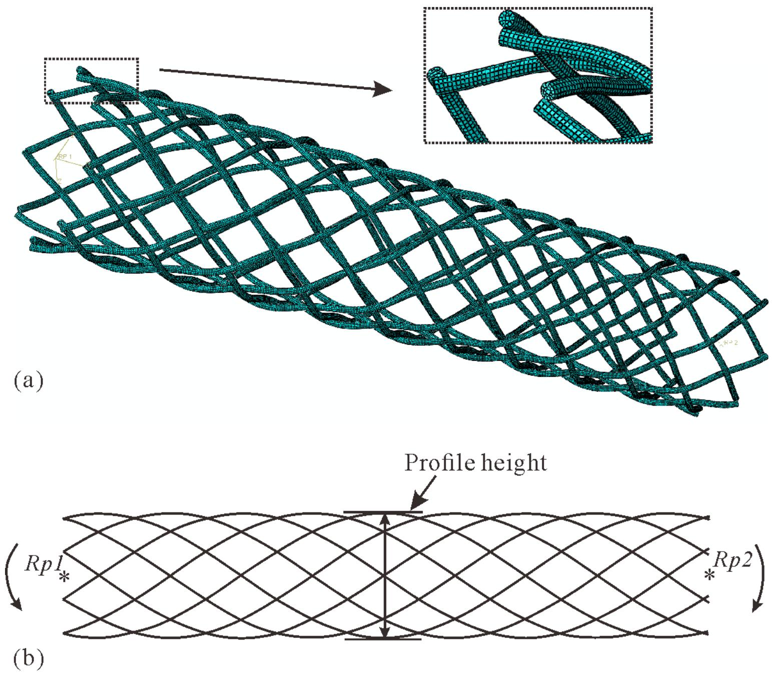

Figure 2-10 (a) Numerical model of bending test based on solid elements and (b) its boundary condition.

2.3.2 Results

First of all, the relationship between the bending angle and the profile height is described, and both experimental and numerical curves are presented in Figure 2-11. It can be seen that the two curves show the same tendency and match well. The profile height is nearly changeless at a smaller bending angle, which starts to drop at a bending angle of around 50° and the trend gets sharply when the bending angle exceeds 100°. The deformations of the tube are then presented in Figure 2-12. The simulations and experiments show the same bent configurations, indicating that the tube keeps a basically intact profile at a bending angle of 57° but collapses when the angle increases to 150°. On the grounds of the numerical results, the collapsed profile and its adjacent fibers suffer from higher stress, especially those below the neutral surface.

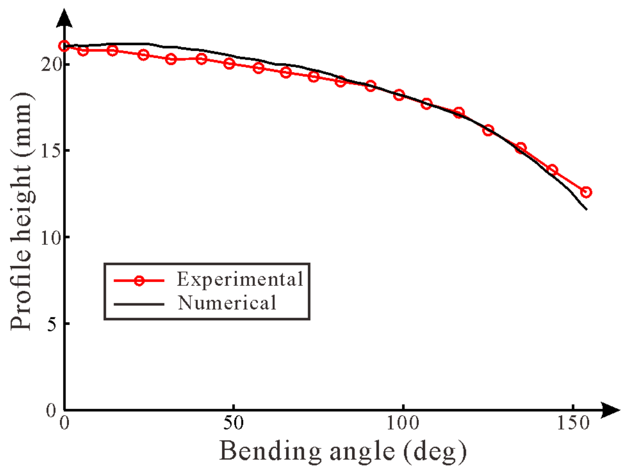

Figure 2-11 Bending angle versus profile height curves.

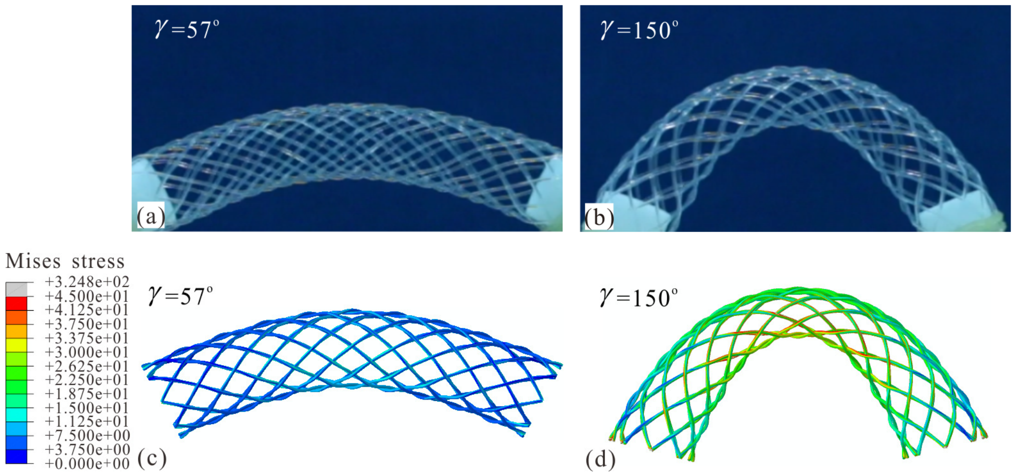

Figure 2-12 Experimental bent configuration at bending angles of (a) 57° and (b) 150°, and (c-d) the numerical ones.

Next, details of the collapsed profile are looked into, and the braiding angles at the highest and the lowest points are shown in Figure 2-13. It can be seen that the braiding angle at the highest point is positively correlated to the bending angle whereas that at the lowest point is negatively correlated. The fibers above the neutral surface are tensioned and those below the surface are compressed, bringing about the different change tendencies of the braiding angles. An increased braiding angle shortens the perimeter of the profile, and a decreased one elongates it. In Figure 2-13, the braiding angle at the lowest point decreases at first, but nearly remains unchanged when the bending angle exceeds 100°, which cannot match the continuously increasing braiding angle at the highest point. As a consequence, the perimeter decreases and a collapsed profile is formed.

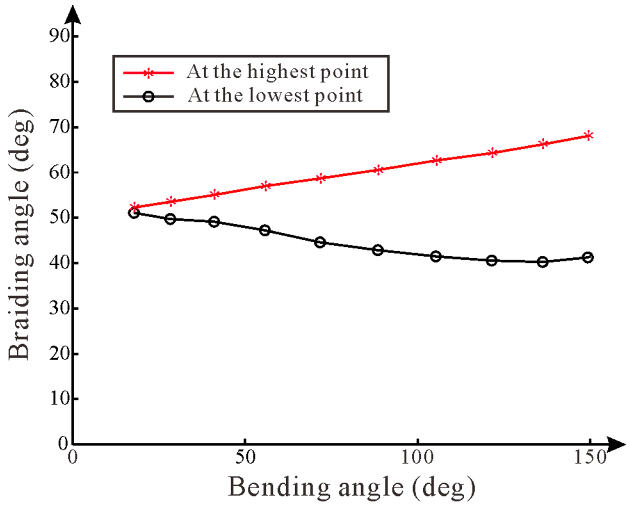

Figure 2-13 Changes of the braiding angles in the collapsed profile.

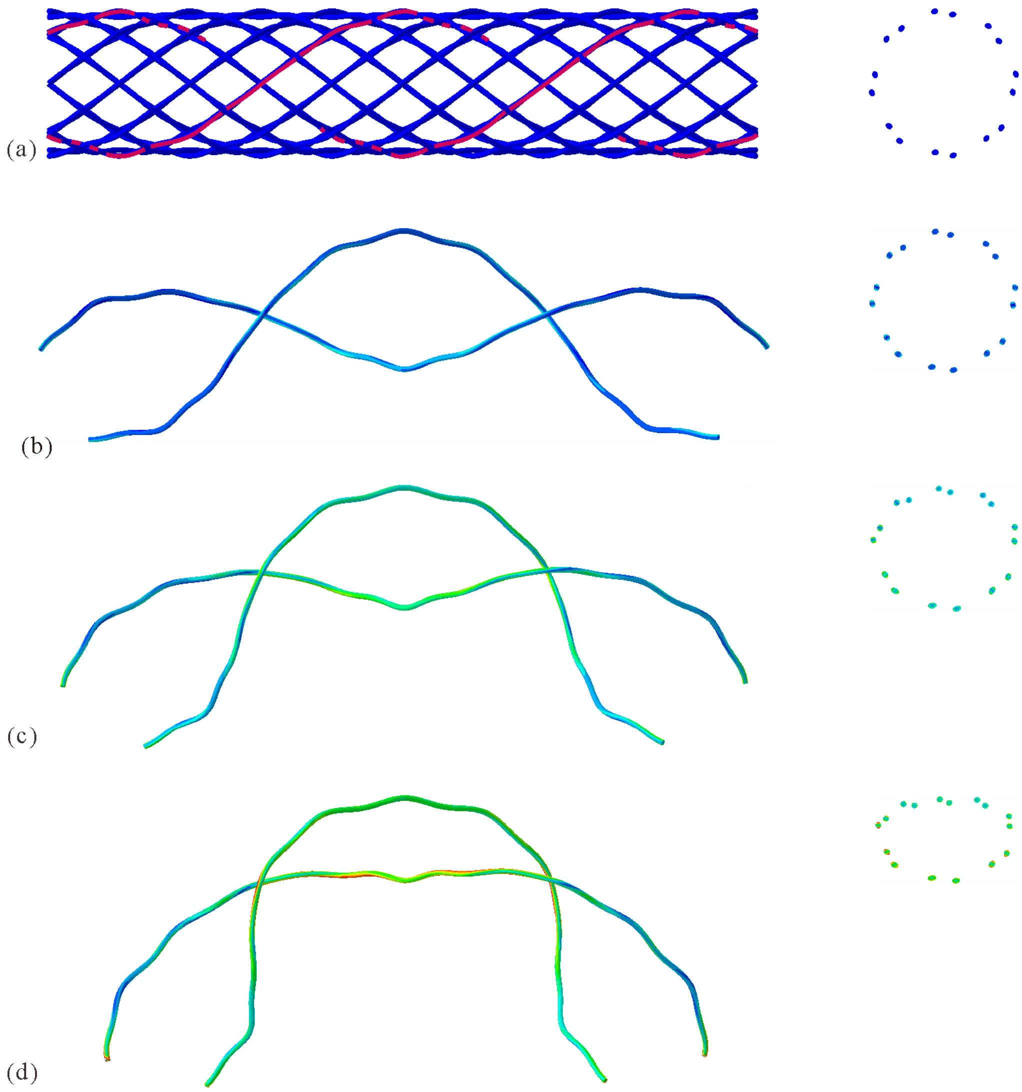

Figure 2-14 Collapse process of the tube: (a) original state, (b) intact-profile state, (c) slightly collapsed and (d) completely collapsed states.

The nonlinear change tendency of the braiding angle at the lowest point is explained by analyzing the fiber deformation. Figure 2-14(a) shows the front view and collapsed profile of the unloaded model. To clearly illustrate the deformation process, all fibers are hidden except two special fibers highlighted in red in the front view, which reach the highest and the lowest points of the collapsed profile of the tube.

The deformation process can be divided into three steps. In the first step, the tube experiences a deformation of nearly pure bending, as shown in Figure 2-14(a) to Figure 2-14(b), and the cross-sectional shape does not change and keeps an intact profile. Then, the tube starts to collapse and reaches a configuration shown in Figure 2-14(c). The profile height decreases gradually whereas the width is changeless. In this case, the profile turns to be an ellipse. Finally, it comes to the last step, during which the tube collapses completely to the configuration shown in Figure 2-14(d). It is found that the lowest fiber deforms a lot and plays a vital role in the collapse behavior. It changes from a concave curve to a convex one, which reduces the deformation in the collapsed profile. This can account for why the braiding angle at the lowest point gets changeless.

2.3.3 Effects of Structural Parameters

The parameters about bending of the braided tube can be divided into two groups. One concerns the parameters about mesh configuration of the tube, including fiber diameter d, fiber number n, braiding angle β, Young's modulus E_f and friction coefficient μ. The other involves overall parameters of the tube, including tube length L and tube diameter D. The independence of the overall parameters is analyzed in Figure 2-15. A braided tube at bent configuration is firstly shown in Figure 2-15(a) as a benchmark. Figure 2-15(b) demonstrates the bent configuration of a longer tube, revealing a similar curvature as that in Figure 2-15(a). Despite a larger bending angle of the longer tube, its larger length helps release the bending extent. This is because the length and the bending angle jointly affect the curvature k, which is calculated as

$$k = \gamma / L \tag{2-4}$$

Thus, at a larger bending angle, a longer tube can present a similar bending configuration as that of a shorter one. In this way, the tube length would not be considered, since it is not an independent parameter. Similarly, the bent configuration of a tube with a larger D is shown in Figure 2-15(c). It resembles that shown in Figure 2-15(a) for its length is proportionally elongated according to their diameter ratio. A tube with a different diameter can be equivalent to one with a standard diameter, and then equivalent to one with a standard length at a different bending angle. As a consequence, the parameter D is also dependent and does not need to be considered.

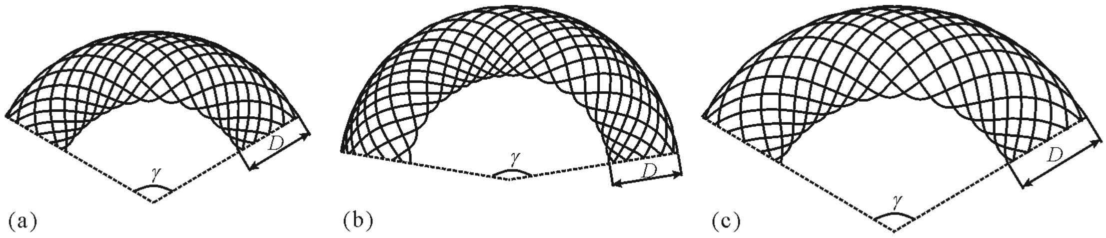

Figure 2-15 Bending configurations of (a) a normal braided tube, (b) a longer tube and (c) a fatter tube.

To figure out the effects of design parameters on the collapse behavior, a series of numerical models are established, and orthogonal test is performed. Five parameters are taken into consideration, including β, n, d, material property and μ. $L_{12}(2\text{\^{}}6)$ orthogonal table can contain the whole five parameters and an empty column. Each parameter has two levels and there are twelve tests in total. Set as 100mm and 20mm respectively for each numerical model, tube length L and tube diameter D are constants. The maximum geometrical angle of the mouth-esophagus natural orifice occurs at throat, which is about 90°, and the maximum bending angle in this analysis is 120°. The setup of the orthogonal test is listed in Table 2-3.

Table 2-3 Orthogonal table for bending collapse analysis

Number	β	n	d (mm)	Material	μ	Empty	Result (mm)
1	30°	12	0.5	Steel	0.3	1	0.08
2	30°	12	0.5	Steel	0.3	2	0.08
3	30°	12	1.0	PA66	0.6	1	0.04
4	30°	16	0.5	PA66	0.6	1	0.06
5	30°	16	1.0	Steel	0.6	2	0.08
6	30°	16	1.0	PA66	0.3	2	0.08
7	60°	12	1.0	PA66	0.3	1	9.12
8	60°	12	1.0	Steel	0.6	2	10.61
9	60°	12	0.5	PA66	0.6	2	8.45
10	60°	16	1.0	Steel	0.3	1	14.35
11	60°	16	0.5	PA66	0.3	2	13.03
12	60°	16	0.5	Steel	0.6	1	15.27

As listed in Table 2-3, the reduction of the profile height of each collapsed profile is recorded as the result to show the collapse extent. The average results of each parameter at levels 1 and 2 are calculated as k_{1j} and k_{2j}, and their difference is calculated as Ra. The results are manifested in Table 2-4. It reveals that Ra of β is the largest, which is up to 11.74, implying that β has the largest effects on the collapse behavior. The second most important factor is n, followed by material, d, and μ. It needs to be emphasized that Ra results of d and μ are smaller than that of the empty column.

Thus, it can be concluded that d and μ barely have any effect on the collapse, and the results of them are caused by error. Hereby, the d and μ columns, as empty columns, can be used to calculate the error.

Table 2-4 Calculation of the orthogonal test results

Parameter	β	n	d	Material	μ	Empty
k_{1j}	0.07	4.73	6.16	6.75	6.12	6.49
k_{2j}	11.81	7.15	5.71	5.13	5.75	5.39
Ra	11.74	2.41	0.45	1.62	0.37	1.10
Rank	1	2	4	3	5	-

F-examination is conducted to judge if the effects of these parameters are significant. The statistical result of j column is calculated as

$$F_{\mathrm{j}} = {S_{\mathrm{j}}}/{S_{\mathrm{E}}} \tag{2-5}$$

where S_j and S_E are variances of j column and error columns, respectively.

The F-examination results are listed in Table 2-5. It is presented that the F-statistics of β and n exceed the critical value prominently, while that of the material is smaller than the critical value. Thus, it is fair to say that the collapse depends on β and n, and the material does not need to be considered in collapse design.

Table 2-5 F-examination results

Parameter	Mean square	F	Fa (0.05)	Remarkable
β	413.13	267.40	7.71	Yes
n	17.497	11.32	7.71	Yes
Material	7.825	5.06	7.71	No
Error	1.545	-	-	-

Though the collapse behavior is sensitive to both β and n, the result of β (267.4) is much larger than that of n (11.32). In addition, fiber number cannot be tuned casually because of limits in cover factor, structural stability and braiding machine capability. Thus, the collapse extents of braided tube with different braiding angles are more focused. Twelve fibers are enough to form a stable structure at an acceptable cover factor. A series of numerical models with a constant fiber number of twelve but different braiding angles are established and analyzed, results of which are presented in Figure 2-16. At a smaller braiding angle, in a range of 30° to 40°, the profile height is nearly unchanged. In contrast, when the braiding angle is over 40°, the collapse behavior appears which is getting more serious at a larger braiding angle. When it reaches around 48.5°, the height is reduced to 85% of its original height. Thus, a braided tube with twelve fibers should exert a braiding angle smaller than 48.5° to avoid collapse. If the fiber number is larger, the maximum braiding angle will be even smaller. Under the circumstance that the bending angle is 120° and the tube length is 100mm, the radius of curvature is 47.7mm. Thus, a braiding angle smaller than 48.5° can make the manipulator successfully pass through an orifice with a radius of curvature of 47.7mm.

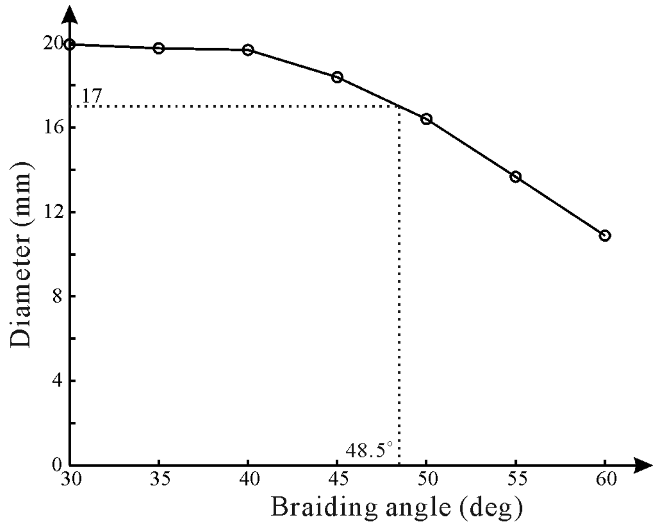

Figure 2-16 Effects of the braiding angle on collapse: profile height versus braiding angle curve.

2.4 Hybrid Braiding

The tube should take with great stability under longitudinal load, thus avoiding improper deployment during insertion. An increased fiber diameter or fiber number can improve the longitudinal stiffness, but tuning the parameters can affect other tube properties, such as covering factor and tube thickness. In this section, a hybrid braiding pattern is designed, which can obtain an improved longitudinal stiffness compared with a uniform tube at the same fiber length. The stiffness-enhancing mechanism is first analyzed through a view of geometry and then validated through experiments and simulations. A parametric analysis is presented next to figure out the effects of the parameters on the longitudinal stiffness. Finally, its bending behavior is compared with that of the ordinary braided tube.

2.4.1 Concept and Mechanism of the Hybrid Braiding

A uniform braided tube with identical braiding angles in clockwise and anticlockwise directions is shown in Figure 2-17(a). If the braiding angles in both directions are different, a hybrid braided tube as shown in Figure 2-17(b) can be obtained.

In a hybrid braided tube, each fiber is still a helix, and its length can be calculated by

$$\begin{cases} l_1 = L / \sin \beta_1 \\ l_2 = L / \sin \beta_2 \end{cases} \tag{2-6}$$

To quantify the degree of hybrid, the hybrid ratio, *hr*, is defined as

$$hr = \frac{l_2 - l_1}{l_1 + l_2} = \frac{\sin \beta_1 - \sin \beta_2}{\sin \beta_1 + \sin \beta_2} \tag{2-7}$$

A higher *hr* means a larger length difference between the fibers, also a higher degree of hybrid. Besides, a weighted average of braiding angle β_0 is also defined as

$$\beta_0 = \arcsin \frac{2L}{l_1 + l_2} = \arcsin \frac{2 \sin \beta_1 \sin \beta_2}{\sin \beta_1 + \sin \beta_2} \tag{2-8}$$

For braided tubes with identical β_0, the average fiber lengths, $(l_1 + l_2)/2$, are also the same. A bigger β_0 indicates a smaller fiber length. In the case of uniform braid, β_0 reduces to β.

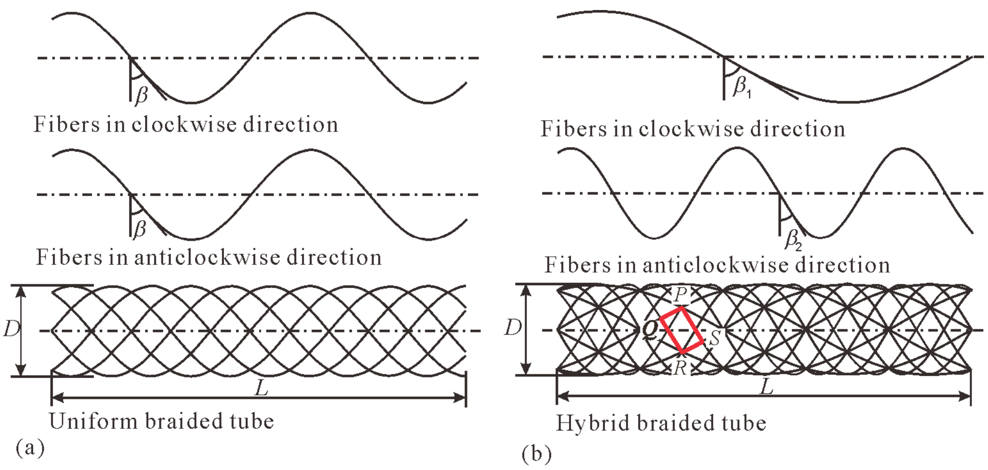

Figure 2-17 Geometrical configurations of (a) uniform braided tube and (b) hybrid braided tube.

When a braided tube is longitudinally tensioned, the deformed configurations can be determined by considering the units highlighted by red in Figure 2-17. The geometry of the units of uniform braided tubes with β_1 and β_2 are respectively presented in Figure 2-18(a) and Figure 2-18(b), and that of the hybrid braided tube is presented in Figure 2-18(c), in which *w* and *he* are respectively the width and height of the units. All the units have identical unit height but different braiding angles. When they are pulled longitudinally, points *P* and *R* can only move in the circumferential direction due to symmetry, whereas points *Q* and *S* move in the longitudinal direction. Besides, since the fiber is assumed to be inextensible during deformation, the side lengths of the units remain unchanged. Then, the diameter of a deformed uniform braided tube can be calculated by

$$D'/D = he'/he = (w'/w)\tan\beta/\tan\beta' \tag{2-9}$$

where parameters of the deformed braided tube and fiber are denoted with primes. With the same assumptions, the diameter of a deformed hybrid braided tube can also be acquired as

$$D'/D = he'/he = (w'/w)\frac{\sin\beta_1\sin\beta_2\sin(\beta_1+\beta_2)}{\sin\beta_1'\sin\beta_2'\sin(\beta_1'+\beta_2')} \tag{2-10}$$

With Eq. (2-9) and Eq. (2-10), the deformed configurations of the units at the same tensile ratio $w'/w = 20\%$ are acquired and presented in Figure 2-18(d-f). It can be seen from Eq. (2-9) that of the uniform braided tube depends on the braiding angle β. Since all the fibers have identical β, its deformed configuration is always geometrically compatible. When two different braiding angles exist in a single braided tube as in the case of the hybrid one, the two braiding angles will determine two different tube diameters at an identical tensile ratio w'/w, which are geometrically incompatible. These two diameters will interact to form the final diameter, which can be calculated with Eq. (2-10). Such interaction would require additional energy to realize, leading to increase in the longitudinal stiffness of the hybrid braided tube.

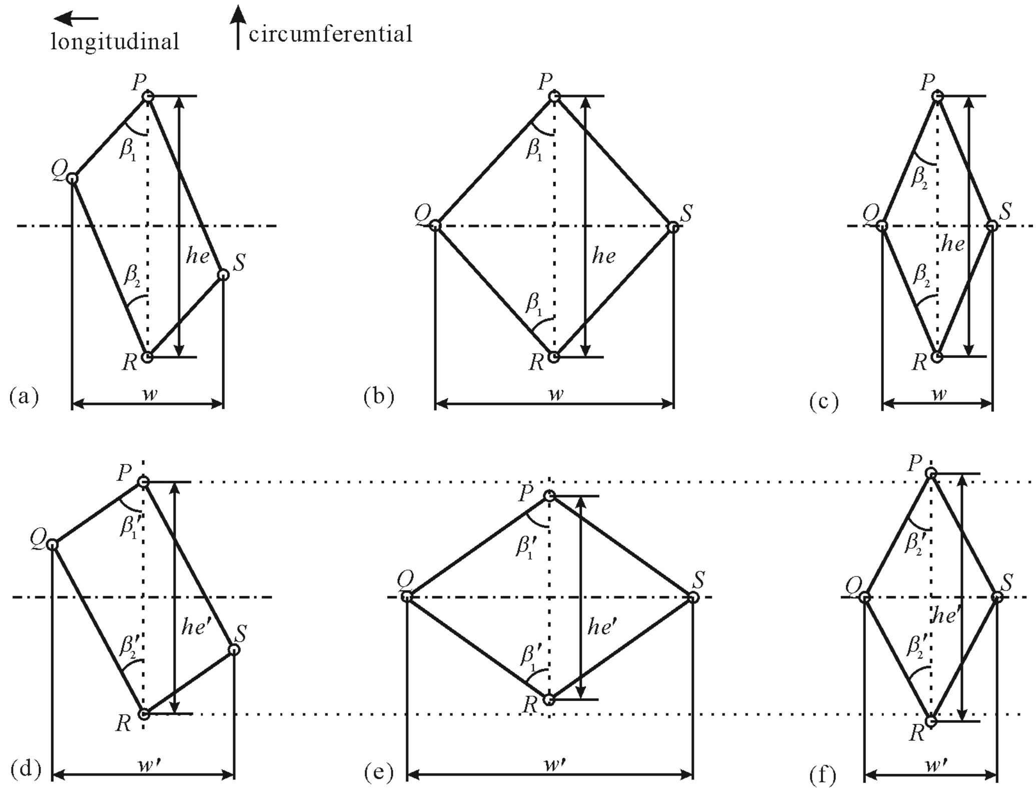

Figure 2-18 Units of (a) (b) uniform braided tubes with β_1, β_2, (c) hybrid braided tube, and (d)-(f) their deformed configurations at a longitudinal tensile ratio of 20%.

2.4.2 Experimental Setup and Numerical Model

Nylon PA66 fiber was selected for one uniform braided tube and two hybrid braided tubes, which were fabricated using the manual method. With Eq. (2-8), the β_0 of the three tubes were calculated to be 48.82°, 48.78° and 48.64°, respectively. The maximum difference of β_0 was only 0.37%, which ensured nearly identical mass of the three specimens. With Eq. (2-8), *hr* of the three specimens were calculated to be 0, 0.065 and 0.100, respectively. The Young's modulus of the nylon was obtained with tensile tests, and the parameters of the physical specimens are listed in Table 2-6.

Table 2-6 Parameters of the physical specimen in hybrid braid analysis

Parameter	Value
Tube length, L	122.00mm
Tube inner diameter, D_i	20.00mm
Fiber number, n	12
Fiber diameter, d	1.07mm
Braiding angle, β	48.82° (Uniform 1)
	48.78° (Hybrid 1)
	48.64° (Hybrid 2)
Young's modulus of the fibers, E_f	3498.6Mpa

To evaluate the longitudinal stiffness of the tubes, the physical specimens were tensioned on the Instron 5982 testing machine. The experimental setup is illustrated in Figure 2-19. Both ends of the tube were clamped to two blocks, respectively. One block was fixed, and the other was moved upwards by a tension wire connected to the load cell. Displacement control was applied in the experiments and the loading rate was set as 2mm/min to avoid dynamic effects. The final tensile displacement was set as 5% of the original length. During the experiments, the displacement and force were recorded automatically.

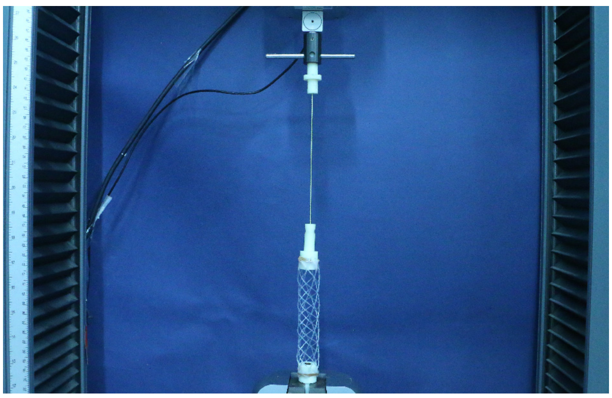

Figure 2-19 Experimental setup for longitudinal stiffness.

The method introduced in Section 2.3.2 was used to establish the numerical model of the braided tube. The nodes at the ends of the tube were tied to two reference points, *Rp1* and *Rp2*, respectively, as rigid bodies. To model the tensile experiments, *Rp*2 was completely fixed in space, whereas all the degrees of freedom (DOFs) of *Rp*1 were constrained except for the translational DOF in the longitudinal direction and rotational DOF about the axis of the braided tube. A prescribed longitudinal displacement was assigned to the translational DOF of *Rp1* to control the tensile process, and smooth amplitude definition built in *Abaqus* was assigned to control the tensile rate. Friction coefficient was also considered and set as 0.2.

The bending flexibility was also modelled using the same modelling method as that employed in Section 2.3.1. Prescribed rotations about the radius of the braided tube were assigned to the rotational DOF of the *Rp*1 and *Rp*2, respectively, to control the bending process. Directions of the rotation of *Rp*1 and *Rp*2 were opposite to achieve a 180^{o} bending of the tube.

Convergence tests with respect to mesh density and analysis time, respectively, were conducted prior to the analysis. It was found out that mesh size of 0.2mm, and step time of 0.1s, yielded satisfactory results.

2.4.3 Results and Discussions

1. Longitudinal stiffness of the uniform and hybrid braided tubes

Tensile experiments of the three physical specimens are first studied to demonstrate the increase in longitudinal stiffness due to hybrid braiding. The experimental force versus displacement curves are presented in Figure 2-20. It can be seen that the reaction force level is significantly raised when hybrid braiding is adopted, and the improvement is positively correlated to the hybrid ratio. Compared with the uniform braided tube, the forces of the hybrid tube 1 and hybrid tube 2 at a tensile ratio of 5% are increased by 15.44% and 57.12%, respectively. Numerical results are also drawn in the same figure. Numerical results of both the uniform braided tube and the hybrid ones show great consistence with the experimental results. Errors between the results of all three models at a tensile ratio of 5% are only 7.36%, 1.58% and 8.59%, respectively, thereby validating the accuracy of the numerical models.

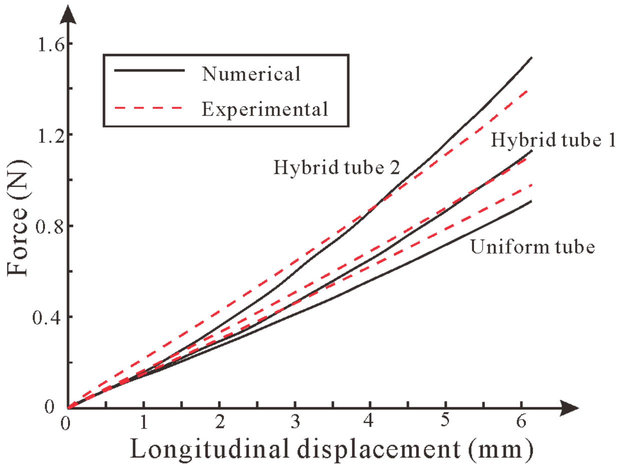

Figure 2-20 Force versus longitudinal displacement curves of the uniform and hybrid braided tubes.

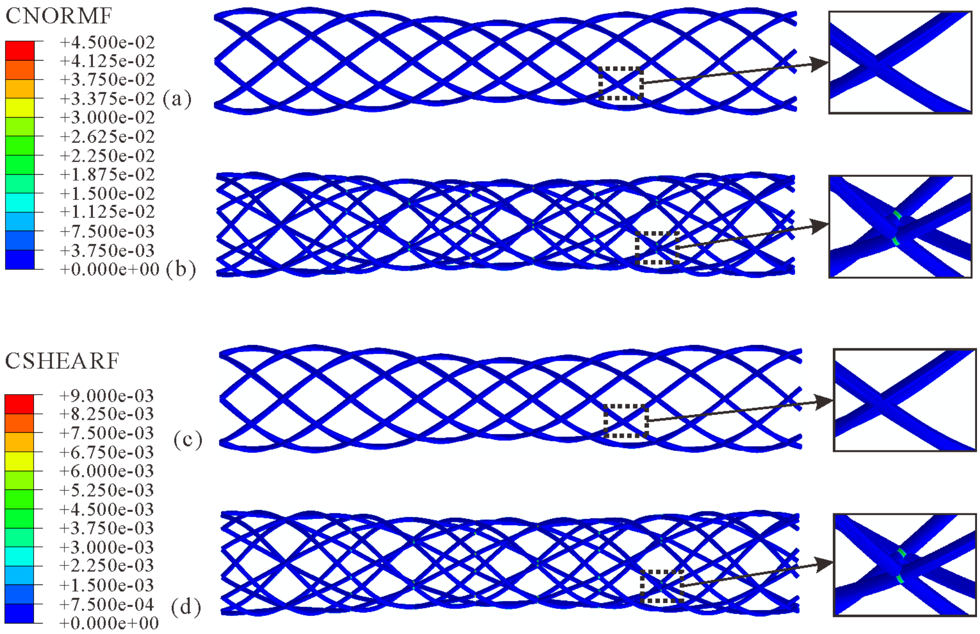

Figure 2-21 Normal contact force (CNORMF) distributions of (a) uniform braided tube and (b) hybrid braided tube 2, and shear contact force (CSHEARF) distributions of (c) uniform braided tube and (d) hybrid braided tube 2 at a tensile ratio of 5%.

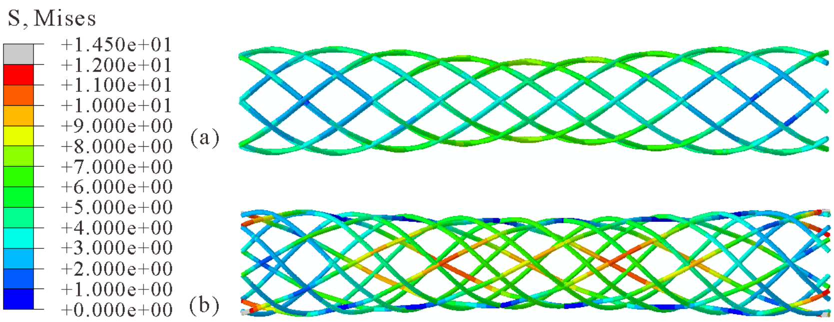

Figure 2-22 Mises stress distributions of (a) the uniform braided tube and (b) the hybrid braided tube 2 at a tensile ratio of 5%.

A detailed analysis of the numerical models indicates that the improved stiffness is caused by the increased contact force existing at the intersections of the hybrid tube, as shown in Figure 2-21. For the uniform tube, the contact force at the intersections is very small. As Figure 2-21(a) and (b) show, the maximum normal force and shear force are only 7.234×10^{-4}N and 1.395×10^{-4}N, respectively. For the hybrid tube 2, on the other hand, the forces increase to 437.2×10^{-4} N and 87.26×10^{-4}N, respectively, about 60 times larger than those of the uniform tube. The hybrid braiding angle is responsible for the high contact force. With the same tensile ratio, Eq. (2-9) yields different braid diameters for the two sets of fibers in a single tube. These two sets of fibers have to interact with each other and compromise to reach a final configuration. Large contact forces are required to overcome such geometric incompatibility, leading to an increase in stiffness. The Mises stress of the two braided tubes are shown in Figure 2-22, which further prove the higher stress in the hybrid model because of geometric incompatibility.

2. Effects of design parameters on the longitudinal stiffness

To investigate the effects of geometric parameters on the performance of the hybrid braided tubes, a set of numerical models were built and analyzed. All the models had the same length and diameter as those listed in Table 2-6. All the other parameters are listed in Table 2-7. The force at a tensile ratio of 5% was recorded and shown in Figure 2-23.

Table 2-7 Parameters of the numerical models in hybrid braid analysis

Group	*hr*	β_0	*n*	*d* (mm)
A	0,3%,6%,9%,12%15%	45°	12	1.0
B	0,15%	35°,40°,45°,50°	12	1.0
C	0,15%	45°	12,16,20,24	1.0
D	0,15%	45°	12	0.6,0.7,0.8,0.9,1.0

First consider the effects of hybrid ratio *hr*. Six models in Group A with varying *hr* from 0 to 0.15 were analyzed and the results are presented in Figure 2-23(a). It can be seen that when *hr* is less than 0.06, the reaction force keeps nearly unchanged, since the difference in length between the two sets of fibers is very small. A noticeable increase in force is observed when *hr* is larger than 0.06. When *hr*=0.15, the reaction force is increased by 110.8%, demonstrating the effectiveness of the hybrid ratio.

Next, the effects of weighted average of braiding angle β_0 are studied. Both uniform and hybrid models in Group B with varying β_0 from 35° to 50° were analyzed and the results are presented in Figure 2-23(b). It can be seen that the forces of both uniform and hybrid braided tubes increase with β_0. In addition, a strong nonlinear relationship between force and β_0 is observed for the hybrid tubes, as opposed to the approximately linear relationship for the uniform ones. Compared with the uniform one, the hybrid tube can obtain a 18.6% force increase when β_0=35°, and 418.3% force increase when β_0=50°. Therefore, relatively large β_0 should be selected in the design if a high longitudinal stiffness is required.

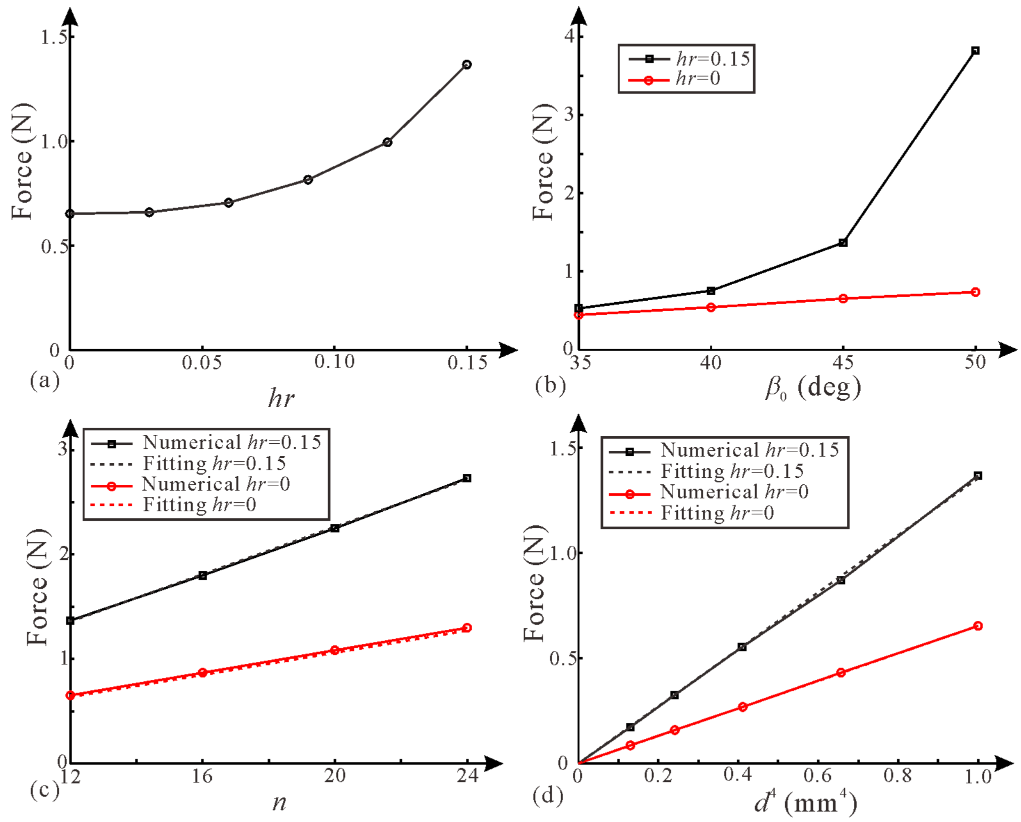

Figure 2-23 Effects of (a) hybrid ratio, (b) weighted average of braiding angle, (c) fiber number, (d) fiber diameter on the longitudinal stiffness of the hybrid braided tube.

Subsequently, the effects of fiber number n are investigated with both uniform and hybrid models in Group C which had varying n from 12 to 24. As can be seen from Figure 2-23(c), the forces of both the uniform and hybrid tubes increase with n, and nearly a linear relationship is obtained as demonstrated by the linear fitted curves marked by dotted lines. As a result, the ratio of the force of the hybrid tube to that of the uniform tube is constant regardless of n.

Finally, the effects of fiber diameter d are looked into with both uniform and hybrid models in Group D which had varying d from 0.6mm to 1.0mm, and the results are presented in Figure 2-23(d). In both cases, an approximately linear relationship between force and d^4 is obtained. The reason is that during tension, the fibers mainly undergo bending. The bending stiffness of a fiber can be expressed as $E_f \pi d^4 / 64$, which is linear with d^4. Therefore, the force also increases linearly with d^4. This result indicates that the deformation mechanisms of both tubes are independent of d, and increasing d can increase the longitudinal stiffness of both tubes to the same extent.

3. Bending flexibility

Apart from longitudinal stiffness, bending flexibility of the braided tube has also been focused to see if the hybrid configuration has effects on bending behavior. The deformed configurations of the models with hr=0 and hr=0.15 in Group A are presented in Figure 2-24. It can be seen that the hybrid tube can retain its open cross-sectional shape as the uniform tube does. The inner diameters at the middle point in longitudinal direction of the uniform tube and the hybrid tube are 19.78mm and 19.55mm, respectively, with a difference of only 1.16%.

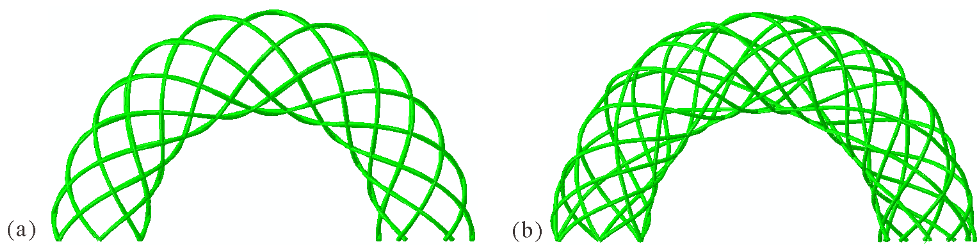

Figure 2-24 Bending deformations of (a) uniform braided tube and (b) hybrid braided tube.

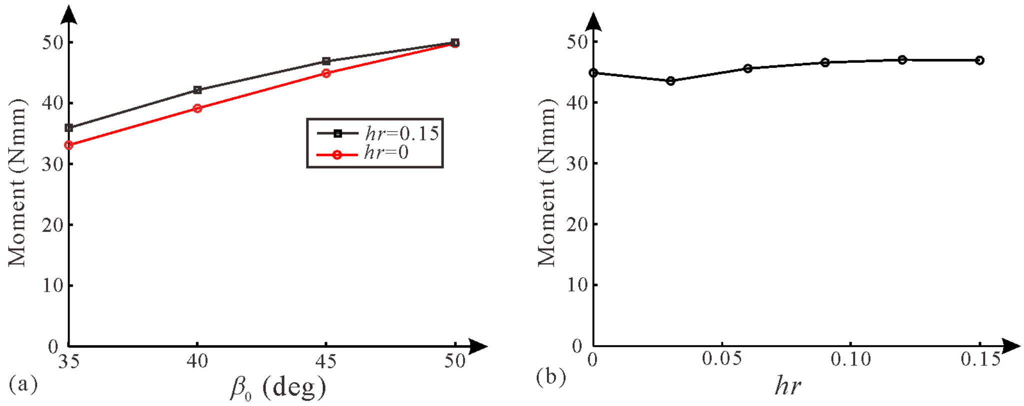

Figure 2-25 Effects of (a) weighted average of braiding angle and (b) hybrid ratio on the bending moment of the hybrid braided tube.

Regarding bending flexibility, the bending moment at a bending angle of 180° for the numerical models in Group A and Group B are extracted from numerical analysis and the effects of weighted average of braiding angle β_0 are presented in Figure 2-25(a). It can be seen that the bending moment required to bend either type of braided tube to 180° slightly increases with β_0. Moreover, within the range of β_0 studied here, the difference between *hr*=0 and *hr*=0.15 is marginal, with the maximum difference of 8.53%.

Then the effects of hybrid ratio are looked into. Figure 2-25(b) presents the bending moment for the numerical models with identical β_0=45° and varying *hr* from 0 to 0.15. A nearly constant bending moment is obtained, indicating that the bending flexibility is independent of *hr*. Therefore, it can be concluded that when β_0 is identical, the hybrid tube has comparable bending flexibility with the uniform one, provided that the effect of the hybrid ratio is not very large. This property would greatly facilitate the application as a manipulator skeleton of the hybrid braided tube.

2.5 Conclusion

In this chapter, the mechanical behaviors of the braided tube have been analyzed, through which a theory system for the application of the tube in manipulator has been established. Above all, the deployability is studied, and researchable diameter range of $(0.37-1)D/\cos\beta$ is determined considering the constraints of geometry and force. Afterwards, the bending collapse behavior of the tube has been numerically investigated. Through an orthogonal test, it suggests the braiding angle plays a dominating role in the collapse behavior, and the fiber number occupies the second place. The collapse extent increases with the two parameters. At a fiber number of twelve, a braiding angle smaller than 48.5° can guarantee an intact profile whose height reduction is less than 15%. Then, a new braiding configuration named hybrid braiding is proposed primarily. With the geometric incompatibility caused by the hybrid braiding angle, its longitudinal stiffness has increased by 57.12%, which can be increased further by adopting a larger hybrid ratio. Work in this chapter can provide guidance in dealing with potential failure of the braided manipulator skeleton, such as insufficient deployment, bending collapse and improper deployment.

Chapter 3 Tunable Stiffness Mechanism

3.1 Introduction

As introduced before, a great bending stiffness in rigid state guarantees the instrument stability, and a sufficient radial stiffness helps keep an intact profile against the compression from the narrow orifice. This chapter proposes a tunable stiffness design and analyzes the stiffening mechanisms. In Section 3.2, the tunable stiffness design is firstly introduced. In Section 3.3, bending stiffness is firstly concerned using experimental and numericl methods. Based on the acquired results, a theoretical model is proposed and an explicit equation for the bending stiffness is obtained. A parameteric analysis is also included to know the effects of the design parameters. Section 3.4 focuses on the radial stiffness. Both experiments and simulations are conducted for the details of the mechanisms and parametric analysis. Final conclusion is drawn in Section 3.5.

3.2 Tunable Stiffness Design

To achieve the tunable stiffness, a braided tube and sealing membranes are assembled together as shown in Figure 3-1. In the manipulator, the braided tube serves as a skeleton, whereas membranes are used to cover both the inner and outer surfaces of the braided tube. The membranes form a tubular sealing cavity, which is connected to a pump via an air duct to create negative pressure. In normal flexible state, the effect of the membranes is ignorable. The braiding fibers loosely touch each other at the intersecting points, where the relative movement is only constrained by friction. As a result, the braided skeleton dominates, and the manipulator is flexible and deployable. It tunes its diameter under the action of longitudinal or radial load, causing folding/deploying. And it shows great bending flexibility and can bend at a large curvature. In contrast, when the air in the cavity is exhausted, the manipulator enters the rigid state. In this state, the air pressure compresses the membranes onto the braided tube tightly. The relative motion between membranes and the braiding fibers is restricted, thereby improving stiffness of the manipulator.

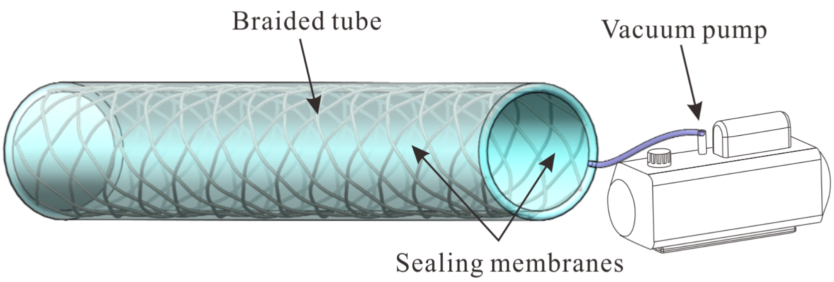

Figure 3-1 The tunable stiffness design of the manipulator.

3.3 Bending Stiffness

3.3.1 Experimental Setup and Numerical Model

Specimens were first prepared to do the experiments. Nylon fiber was selected to fabricate the braided tube and polyethylene membrane was used to form the cavity. A simple fabrication procedure was developed as follows. First, a braided tube was manually constructed with the mehtod introduced in Section 2.3.3 and was put under heat treatment at 100ºC for one hour. A tubular polyethylene membrane was also fabricated by heat sealing. Second, the tubular membrane was dressed on the braided tube, covering both inner and outer surfaces of the tube. Third, a duct was inserted into the cavity, which as sealed with glue. A specimen fabricated with the above method together with the pump system is shown in Figure 3-2. Young's modulus of both the nylon fiber and the polyethylene membrane were tested on an Instron 5982 testing machine, and the parameters are listed in Table 3-1.

Table 3-1 Parameters of the physical specimen for bending stiffness experiment

Parameter	Value
Tube length, L	127.26mm
Tube diameter, D	19.32mm
Fiber number, n	12
Fiber diameter, d	1.07mm
Braiding angle, β	54.43°
Young's modulus of the fibers, E_f	3498.6Mpa
Young's modulus of the membrane, E_m	291Mpa
Membrane thickness, b	0.04mm
Friction coefficient, μ	0.3
Negative pressure, p	67Kpa

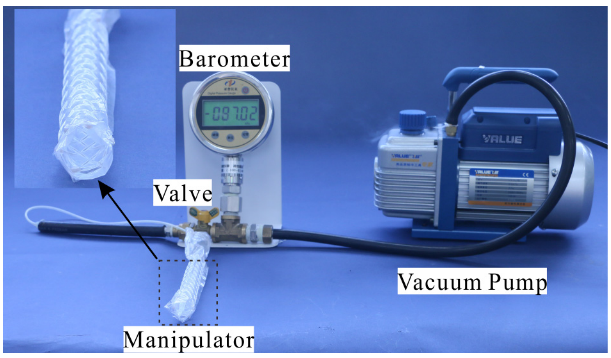

Figure 3-2 Physical model of the tunable stiffness manipulator.

Pure bending experiments were conducted on the physical specimen to evaluate the bending stiffness. The experimental setup was the same as that introduced in Section

2.3. Displacement control was applied in the experiments and the loading rate was 0.3mm/s. The loading process was recorded with a camera and the bending angle was measured from the video. The bending moment is calculated with Eq. (2-3).

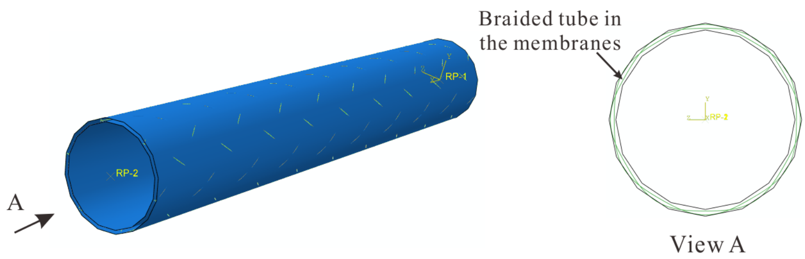

Figure 3-3 Numerical model of the manipulator bending.

Numerical model was established in *Abaqus* and shown in Figure 3-3. The geometrical model of the braided tube was established accoding to the method in Section 2.3.2, whereas those of the membranes were established directly in *Abaqus*. The diameter of the inner membrane was slightly smaller than that of the braided tube, whereas that of the outer membrane was slightly larger to avoid physical interference. Membrane element, M3D4R, was used to mesh the membranes. To model the bending process, two analysis steps were defined. First, uniform pressure was applied to the membranes to model the negative pressure. Subsequently, the pressure was kept at a constant, while opposite rotations about the radius of the manipulator were assigned to the rotational degree of freedoms of the $Rp1$ and $Rp2$, respectively, to achieve a 60^{o} bending of the manipulator. Smooth amplitude definition built in *Abaqus* was utilized to control the bending rate. Friction coefficient was considered and set as 0.3. Mesh sizes of 0.2 mm for the braided tube, 0.5 mm for the membranes, and step times of 0.005 s and 0.03 s for the two steps, respectively, were determined through convergence tests. The rotation angle and moment of reference point $Rp1$ were recorded and output.

3.3.2 Results

Bending of both a manipulator and a stand-alone braided tube were first studied to demonstrate the tunable stiffness. The experiments were respectively conducted three times to the tube and the manipulator. Good repeatability was obtained, and the averages of the results were calculated. The experimental and numerical bent configurations of the manipulator in the rigid state and the stand-alone tube are shown in Figure 3-4 as representatives. No collapse is observed, indicating the design parameters are appropriate. The experimental moment versus bending angle curves are presented in Figure 3-5. First the experimental curves of the braided tube and the manipulator in the flexible state are compared. A linear response is obtained in both cases, and the two curves almost overlap, with the error between them at a bending angle of 60^{o} being only 4.23%. This result validates the assumption in the numerical simulation that the effects of the membranes on bending stiffness in the flexible state is very limited and can be safely ignored. Then the flexible and rigid states of the manipulator are compared. It can be seen that the manipulator shows a highly nonlinear response in the rigid state, and the moment is tremendously raised when negative pressure is applied. At a bending angle of 60^{o}, the bending moment is increased by 585%. To this point, it can be concluded that a device with two remarkably different states of stiffness has been successfully developed.

Numerical simulation results are also presented in Figure 3-4 and Figure 3-5 and compared with the experimental results. At a bending angle of 60^{o}, the numerical data of the manipulator and the braided tube are 14.03% and 8.95%, respectively, lower than the experimental ones, see Table 3-2. This error is mainly caused by the frictional consumption existing in the loading tester in Figure 2-9, which was not considered in the numerical simulations. However, the numerically obtained deformed configurations and moment curves are found to show the same tendency with the respective experimental ones. Therefore, the numerical models are deemed reliable to explain the stiffness-enhancing mechanism. In addition, the maximum strain of the membranes and the braided skeleton are 4.9% and 0.06%, respectively, both of which are in their linear elastic stages.

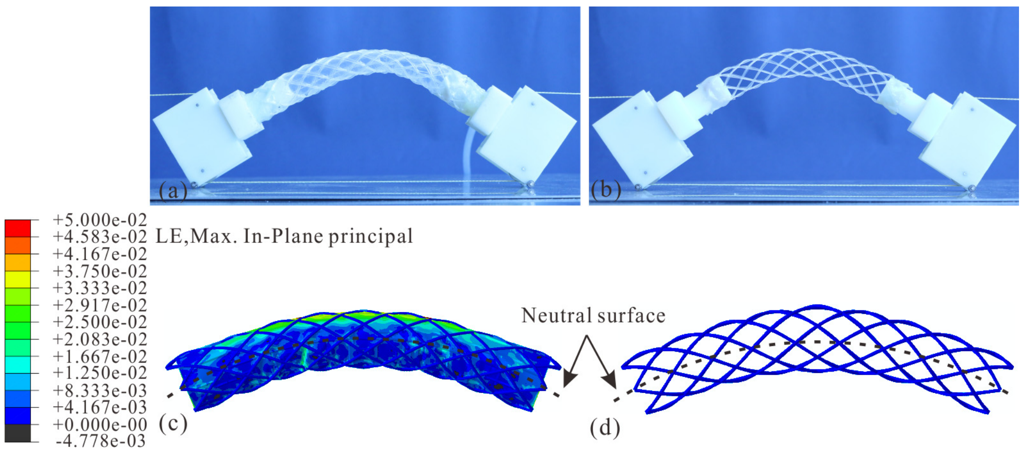

Figure 3-4 Experimental bent configurations of (a) the manipulator and (b) the stand-alone braided tube, and the numerical ones of (c) the manipulator and (d) the stand-alone braided tube.

Table 3-2 Moments at a bending angle of 60^{o} of both the manipulator and the braided tube

Specimen	Result	Value (Nmm)	Error
Manipulator, rigid state	Experimental	136.20	-
	Numerically	117.09	14.03%
	Theoretically	142.80	4.85%
Braided tube	Experimental	19.88	-
	Numerically	18.10	8.95%
	Theoretically	17.14	13.78%

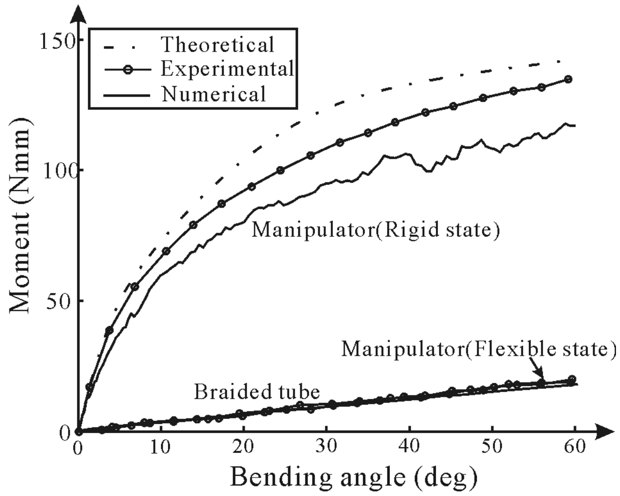

Figure 3-5 Moment versus bending angle curves of both the manipulator and the braided tube.

With the validated numerical models, the stiffness-enhancing mechanism of the manipulator in the rigid state is examined in detail. Figure 3-4(c) shows the bent configuration of the braided skeleton of the manipulator in the rigid state. It can be seen that a nearly pure bending with a measured radius of curvature ρ =136.17mm, similar to the stand-alone tube in which ρ =144.36mm in Figure 3-4(d), is obtained. This suggests that in the rigid state where the membranes are tightly compressed onto the skeleton, the deformation mode of the manipulator is not significantly affected and can still be treated as pure bending. Then the deformation of the membrane is investigated by drawing the longitudinal (LE11) and circumferential (LE22) strain contours of the outer membrane in Figure 3-6(a-b). It can be seen that the membrane above the neutral surface is longitudinally tensioned, whilst that below is circumferentially tensioned. This is because the braiding angle above the neutral surface increases after bending, whereas that below decreases as shown in Figure 3-6(a-b), thereby stretching the membrane in different directions. The deformed membrane can sustain load and therefore improve the stiffness of the manipulator. Note that the change in braiding angle also causes circumferential compression above the neutral surface and longitudinal compression below. However, since membrane cannot sustain compressive load, the compressive deformation does not contribute to stiffness improvement. In addition, it is observed that the membrane above the neutral surface has a larger strain in the middle than that at the two ends.

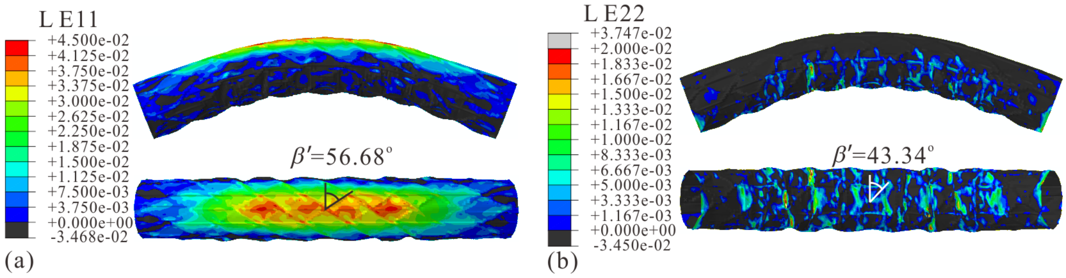

Figure 3-6 (a) Longitudinal and (b) circumferential strain contours of the outer membrane in bending simulation.

3.3.3 Theoretical Model

In the flexible state, the effect of the membranes is ignorable, and the manipulator can be regarded as a stand-alone braided tube. The braided tube can be regarded as a combination of helical springs, and the bending stiffness of the tube can be calculated as the sum of the spring stiffness. Zhang [113] established an energy-based theoretical model to determine the relationship between bending angle and moment of a mechanical spring. The force and the deformation on sections was studied, with which the strain energy of the spring was obtained. In this way, if the change of braiding angle is ignorable, bending moment on one fiber can be acquired as

$$M_{\mathrm{f}}=\frac{2\gamma E_{\mathrm{f}} I_{\mathrm{f}} \sin\beta}{(1+\sin^2\beta+\dfrac{E_{\mathrm{f}}}{2G}\cos^2\beta)} \tag{3-1}$$

where γ is the bending angle. Similarly, if the braided tube is regarded as a combination of independent springs, the moment on a braided tube can be calculated as

$$M_{\mathrm{b}}=\frac{2n\gamma E_{\mathrm{f}} I_{\mathrm{f}} \sin\beta}{(1+\sin^2\beta+\dfrac{E_{\mathrm{f}}}{2G}\cos^2\beta)\ L} \tag{3-2}$$

According to the material mechanics, the bending stiffness of a beam, here the manipulator, can be calculated as

$$EI_{\mathrm{braid}}=M_{\mathrm{b}}L/\gamma=\frac{2nE_{\mathrm{f}} I_{\mathrm{f}} \sin\beta}{1+\sin^2\beta+\dfrac{E_{\mathrm{f}}}{2G}\cos^2\beta} \tag{3-3}$$

In the rigid state, the membranes are compressed by the air pressure onto the braided skeleton tightly, and both components deform simultaneously when bent. The following assumptions are made based on the numerical results: (1) the braided skeleton is also subjected to pure bending (Figure 3-7(a)); (2) compression in the membranes is not considered; (3) when the tensile force is small, there is no sliding between the membranes and the fibers, and the friction between them provides the tensile force; (4) when the tensile force reaches the maximum static friction, sliding will appear between the membranes and the fibers.

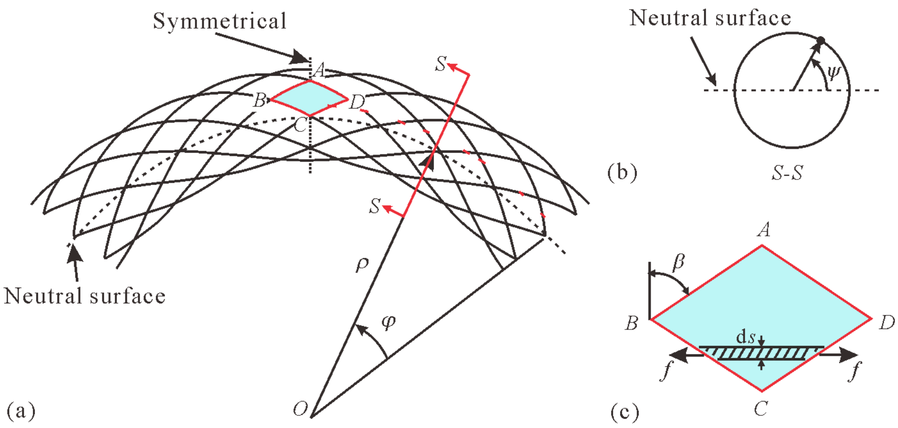

Figure 3-7 Geometry of the bent manipulator: (a) global bending of the manipulator; (b) cross section; (c) a single unit.

According to the assumption of pure bending of the braided skeleton, the longitudinal strain ε_{l}, and the circumferential strain ε_{c}, of the points at the same circular coordinate ψ defined in Figure 3-7(b) are identical, which can be respectively calculated as

$$\begin{cases} \varepsilon_{\mathrm{l}} = \dfrac{D\gamma \sin\psi}{2L} \\ \varepsilon_{\mathrm{c}} = -\dfrac{D\gamma \sin\psi}{2L} \tan\beta \end{cases} \tag{3-4}$$

In addition, the elastic strain energy of the braided skeleton can be calculated based on Eq. (3-3) as $0.5EI_{\mathrm{braid}}\gamma^2$.

Regarding the deformation of the membranes, first consider the membranes above the neutral surface $(0^{\circ} < \psi < 180^{\circ})$ by selecting a unit ABCD in Figure 3-7(c). Based on assumption (3), when the tensile force is below the maximum static friction, there is no sliding between the membranes and the fibers, and therefore the longitudinal strain of the membranes is identical to that of the braided skeleton. Accordingly, the tensile force of a strip with an infinitesimal circumferential length ds at a circular coordinate ψ can be calculated as

$$f = E_{\mathrm{m}}\varepsilon_{\mathrm{l}} b \mathrm{d}s \tag{3-5}$$

where E_{m} and b are the Young's modulus and thickness of the membranes.

Meanwhile, the maximum static friction at the same circumferential length is

$$f_{\max} = Np\mu \frac{\pi d}{\cos\beta} \mathrm{d}s \tag{3-6}$$

where p is the negative pressure; μ is the friction coefficient; N is the number of fiber segments highlighted in red, which contributes to the friction and can be determined by

$$N=\frac{\varphi nL}{\gamma \pi D\tan\beta} \tag{3-7}$$

where φ is a circle angle shown in Figure 3-7(a). When the tensile force rises to the maximum static strain, the membrane strain also reaches its maxima, or the critical strain, which is determined from Eqs. (3-5)-(3-6) as

$$\varepsilon_1{}'=\frac{\pi\varphi np\mu d}{\gamma E_{\mathrm{m}} b\sin 2\beta} \tag{3-8}$$

When the longitudinal strain of the braided skeleton ε_1 is smaller than $\varepsilon_1{}'$, the membrane strain is equal to ε_1. When it exceeds $\varepsilon_1{}'$, according to assumption (4), the membranes slide along the braided skeleton and its longitudinal strain stays constant at $\varepsilon_1{}'$. In this case, the energy is contributed by two parts: the elastic strain energy of the membranes, and the work done by the sliding friction force which is considered as identical to the maximum static friction force. As a result, the energy density above the neutral surface can be calculated as

$$W(\varepsilon_1)=\begin{cases}\dfrac{1}{2}E_{\mathrm{m}}b\varepsilon_1{}^2 & (\varepsilon_1\le\varepsilon_1{}') \\ E_{\mathrm{m}}b\varepsilon_1{}'(\varepsilon_1-\varepsilon_1{}'/2) & (\varepsilon_1>\varepsilon_1{}')\end{cases} \tag{3-9}$$

For the membranes below the neutral surface $(180^{\circ}<\psi<360^{\circ})$, only the circumferential tensile deformation is considered. The same approach is used and both the critical strain $\varepsilon_{\mathrm{c}}{}'$ and the energy density $W(\varepsilon_{\mathrm{c}})$ can be determined.

With the analysis above, the total energy of the manipulator in the rigid state can be obtained by summing up the energies contributed by the braided skeleton, the membranes and sliding friction if it exists

$$E_{\mathrm{t}}=2\frac{LD}{\gamma}\left[\int_0^{\pi}\int_0^{\gamma/2}W(\varepsilon_1)\mathrm{d}\varphi\mathrm{d}\psi+\int_{\pi}^{2\pi}\int_0^{\gamma/2}W(\varepsilon_{\mathrm{c}})\mathrm{d}\varphi\mathrm{d}\psi\right]+\frac{1}{2}EI_{\mathrm{braid}}\gamma^2 \tag{3-10}$$

Applying balance between the total energy and the external work, the bending moment can be determined as

$$M_{\mathrm{m}}=\mathrm{d}E_{\mathrm{t}}/\mathrm{d}\gamma \tag{3-11}$$

The bending moment of the manipulator with parameters listed in Table 3-1 is calculated with Eq. (3-11) and validated with the experimental result in Figure 3-5. The theoretical and experimental curves show the same trend, and the difference between them at a bending angle of 60° is only 4.85%, indicating the accuracy of the theoretical model.

3.3.4 Parametric Analysis

With the theoretical model, the effects of design parameters on the stiffness of the manipulator are analyzed here. The design parameters are classified into three categories: membrane parameters E_m and b, membrane-skeleton interaction parameters p and μ, and braided skeleton parameters E_f, n, β , and d. The design parameters of the theoretical models are listed in Table 3-3, and the other parameters are the same as those of the physical specimen listed in Table 3-1.

Table 3-3 Parameters of the theoretical models for bending stiffness analysis

Group	E_m (Mpa)	p (Kpa)	E_f (Gpa)	n	β (°)	d (mm)
1	50~300	30	3.5	12	54.43	1.07
2	50~300	50	3.5	12	54.43	1.07
3	50~300	67	3.5	12	54.43	1.07
4	100	0~100	3.5	12	54.43	1.07
5	200	0~100	3.5	12	54.43	1.07
6	400	0~100	3.5	12	54.43	1.07
7	100	67	0.5~9.5	12	54.43	1.07
8	100	67	3.5	12~36	54.43	1.07
9	100	67	3.5	12	30~60	1.07
10	100	67	3.5	12	54.43	0.5~1.2

1) Effects of the membrane parameters

According to Eqs. (3-8) and (3-9), thickness b and Young's modulus E_m of the membranes affect the stiffness of the manipulator in the same manner through the term $E_m b$, which can be considered as membrane stiffness. To investigate the effects of membrane stiffness, b is set to be 0.04mm, and E_m varies from 50Mpa to 300Mpa. The moments at a bending angle of 30°, denoted by M_{30}, are calculated from Eq. (3-11), and the relationships between M_{30} and E_m at different negative pressures p are drawn in Figure 3-8. The results of the manipulator in the flexible state are also presented as a benchmark. Two observations can be made from the curves. First, M_{30} increases with E_m, indicating that a stiffer membrane leads to a higher bending moment. The reason is that the tensile force carried by the membranes increases with the membrane stiffness. Second, the slopes of the curves, on the other hand, reduce with E_m. This suggests that increasing E_m is more effective when it is relatively small. Therefore, in practice, the membranes need not to be too stiff. According to Figure 3-8(a), membranes with $E_{\mathrm{m}} = 5 \times 10^3 p$ are stiff enough for membranes with a thickness b of 0.04mm.

2) Effects of the membrane-skeleton interaction

Similarly, the negative pressure p and the friction coefficient μ theoretically play the same role in the stiffness of the manipulator for the friction is proportionable to $p\mu$ according to Eq. (3-8). Here μ is set as 0.3 and p varies from 0Kpa to 101Kpa to analyze the effect of friction. M_{30} at different p and E_m are theoretically calculated from Eq. (3-11), and the results are presented in Figure 3-8(b). Generally, M_{30} increases sharply with p, especially when E_m is large. This result clearly demonstrates that applying negative pressure is effective at tuning the bending stiffness of the manipulator.

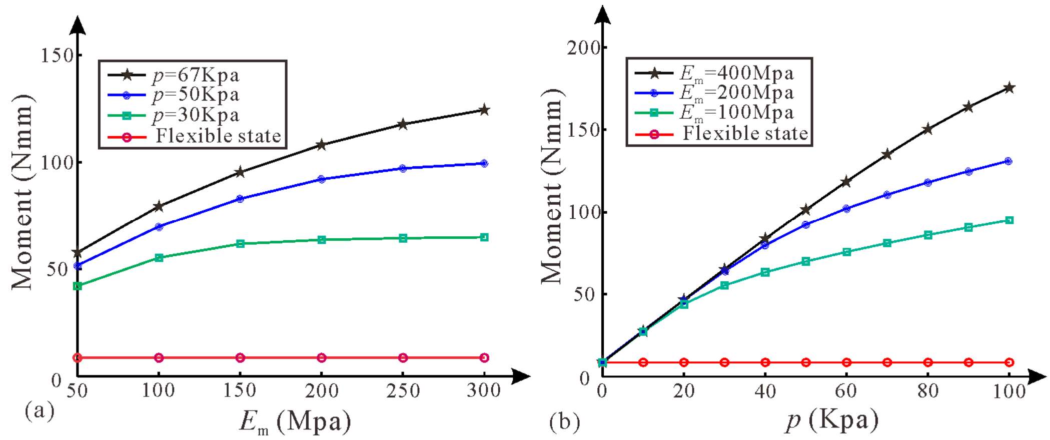

Figure 3-8 Effects of membrane stiffness and friction: (a) M_{30} versus E_m curves at different p; (b) M_{30} versus p curves at different E_m.

3) Effects of the braided-skeleton parameters

The effect of the Young's modulus of the fibers E_f is firstly investigated by varying it from 0.5Gpa to 9.5Gpa. As shown in Figure 3-9(a), a linear response is obtained in both the rigid and flexible states. This is understandable as E_f only linearly increases the bending moment taken by the braided skeleton, which is clearly seen in Eqs. (3-6) and (3-11).

The other three parameters, while mainly affecting the bending stiffness of the braided skeleton as in the case of EI_{braid}, also slightly change the friction due to variation in the number and size of the quadrilateral units in the braided skeleton. The effects of the three parameters on the bending moments are respectively drawn in Figure 3-9(b-d). It can be seen that all the parameters lead to increase in bending stiffness in both states. And roughly linear relationships are invariably obtained.

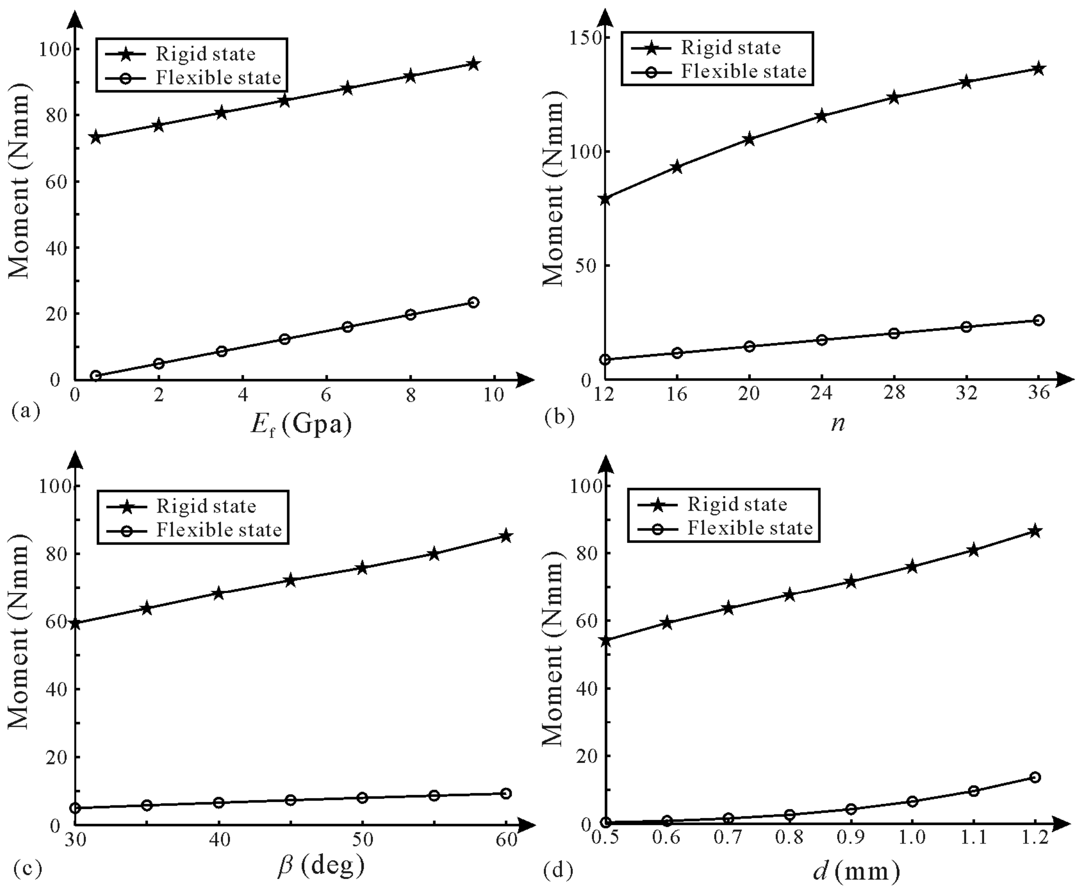

Figure 3-9 Effects of the properties of the braided skeleton: relationships between M_{30} and (a) E_f, (b) n, (c) β , (d) d.

3.4 Radial Stiffness

3.4.1 Experimental Setup and Numerical Model

The braided skeletons here were fabricated using the braiding machine. For the manipulator, other fabrication details were the same as those of the one in bending experiment. In addition, a stand-alone braided tube in which the fibers could freely slide at intersection points and a welded one in which all the fiber intersection points were glued together were also built for comparison purpose. All the three specimens have the same skeleton parameters listed in Table 3-4.

Table 3-4 Skeleton parameters of the specimens for radial compression experiment

Parameter	Value
Length L	100.20mm
Diameter D	19.34mm
Number of fibers n	16
Braiding angle β	44.4°
Fiber diameter d	1.07mm

The lateral indentation experiments of the physical specimens were carried out on the Instron 5982 testing machine. The manipulator was connected to a pump via an air duct to tune the negative pressure. A negative pressure p = 80kPa was applied to the specimen. The experimental setup shown in Figure 3-10(a) was set as Kim et al. [91] suggested, where a circular rod was used to compress the longitudinal midpoint of the specimen to test the radial stiffness. During the experiment, the specimen was placed on a flat plate freely, and a 3D printed circular rod with a diameter of 18mm moved downwards to compress the midpoint of the specimen by 4.5mm, about a quarter of the original tube diameter. To avoid dynamic effects, the indentation was conducted at a loading rate of 5mm/min. Both force and displacement during each experiment were recorded automatically by the Instron.

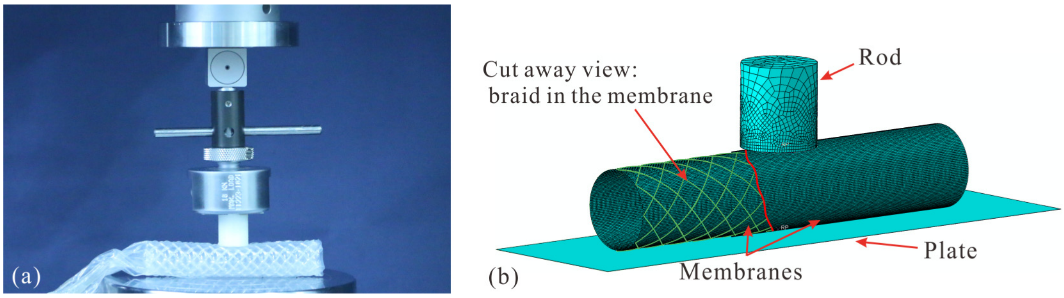

Figure 3-10 (a) Experimental setup and (b) numerical model for radial stiffness test.

Numerical simulations were also conducted using *Abaqus/Explicit*. The modelling method of the manipulator is the same as that in bending simulation. It included a manipulator, a rigid plate and a rod in the model. Two analysis steps were defined to model the loading process of the manipulator. In the first step, both the rod and the plate were fixed, and uniform pressure was applied to both membranes to model the negative pressure. In the second one, at the constant pressure, a prescribed displacement was assigned to the free degree of freedom of the rod to compress the structure. Smooth amplitude definition built in *Abaqus* was adopted to control the indentation procedure. As for the stand-alone braided tube and the welded braided tube, only the second step was applied.

The mesh density and the analysis time were determined prior to the analysis. According to the convergence experiments, mesh sizes of 0.2mm and 0.5mm respectively for the braid and the membranes, and step time of 0.003s and 0.05s respectively for the two steps, were found to yield satisfactory results. The rigid plate was meshed with one element, and a fine mesh with 100 nodes were applied to the lower end of the rod to capture its curved profile. Displacement and force of the rod were recorded during the analysis.

3.4.2 Results

Lateral indentation experiments of the three structures are first presented. The deformed configurations are shown in Figure 3-11(a-c), and the reaction force versus indentation displacement curves are drawn in Figure 3-11(d). It can be seen that the stand-alone braided tube extends longitudinally upon compression, while the other two show negligible change in length. The reaction forces of the three structures increase monotonically with compression displacement. In addition, the stand-alone braided tube and the welded braided tube exhibit the lowest and highest stiffness, respectively, whilst the stiffness of the manipulator is medium. The numerically obtained curves are also drawn in Figure 3-11(d) for comparison. At a displacement of 4.5mm, the force of the manipulator is increased to 3.9 times as much as that of the stand-alone braided tube. Also, a good match between numerical and experimental results is achieved in all the three structures. The errors of at a displacement of 4.5mm of the welded braided tube, the manipulator and the stand-alone braided tube are only respectively 9.1%, 8.0%, and 2.2%, thereby validating the accuracy of the numerical models. The slight differences between numerical and experimental results are mainly due to the limitation of the fabrication process, including weaker gluing at the intersections of the welded braided tube and the additional effects caused by the membranes at the two ends in the manipulator.

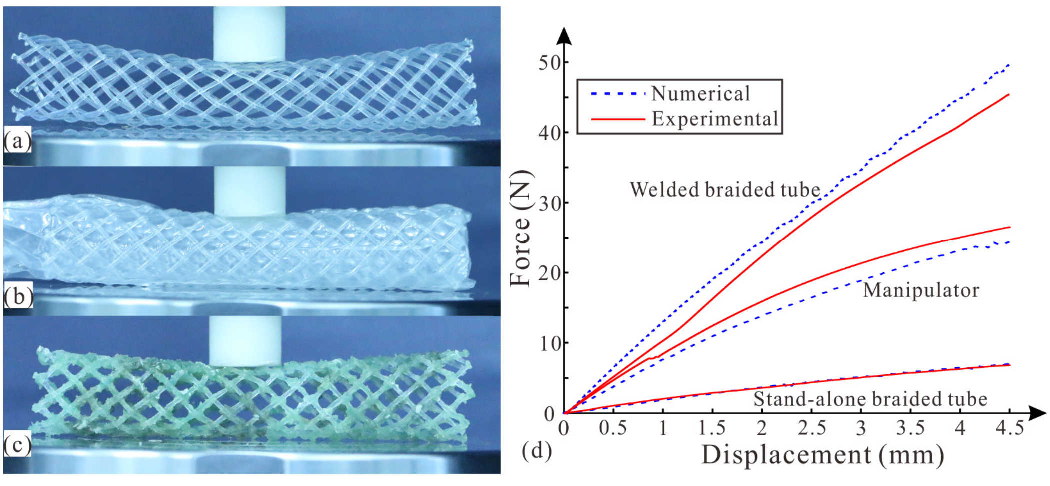

Figure 3-11 Experimental results: deformed configurations of (a) the stand-alone braided tube, (b) the manipulator, and (c) the welded braided tube; (d) reaction force versus indentation displacement curves.

The numerical models that have been validated by experiments are used to reveal more details during deformation of the structures. It starts from the braids, the Mises stress contours of which are shown on the deformed configurations in Figure 3-12(a-c). First the stand-alone braided tube is investigated. Upon compression, the stand-alone braided tube accommodates the deformation easily because the fiber can rotate at the intersection points, leading to increased braiding angles. To demonstrate this feature, the change in braiding angle $\Delta\beta$ of five points along the middle cross section A-A, a~e, and six points along the longitudinal direction, c, f, g, h, j, k, are measured from the numerical model and respectively drawn in Figure 3-12(d-e). It can be seen that a symmetric distribution about point a is obtained along the circumferential direction, leading to an elliptical middle cross section as shown in Figure 3-12(a). Along the longitudinal direction, on the other hand, the braiding angle variation diminishes from the middle section to the end, indicating the localized feature of the indentation. Increase in the braiding angle results in elongation of the stand-alone braided tube, which explains the change in the length by 7mm in the numerical model. Moreover, the stress contour in Figure 3-12(a) indicates that the compression load is main carried through bending of the fibers on the top side of the stand-alone braided tube, which are directly in contact with the rod. This is because the rod tends to straighten the originally curved fibers.

Subsequently the braided skeleton in the manipulator is studied. In comparison with the stand-alone braided tube, the braided skeleton shows three different features. First, as seen in Figure 3-12(d-e), the magnitude of braiding angle variation is much lower due to the restriction provided by the membranes, leading to a slight elongation of only 1.2mm. Second, at the middle cross section B-B, the braiding angle on top (point a) and bottom (point e) decrease, whereas those on the sides (points b, c, d) increase. As a result, a kind of oval shape with localized flattening on the top is obtained. This mode indicates that the membranes effectively bond the fibers and makes them deform more simultaneously like a thin-walled cylinder with continuous surface. Finally, in the vicinity of the rod, apart from the top surface, the fibers at the two sides contribute greatly to the overall stiffness. With the restriction brought by the membranes, they tend to stay their original direction, which is roughly parallel to that of the load. As a result, they become the main load carriers instead of the contacting surface in the stand-alone braided tube, thereby presenting the maximum stress. The numerical results in Table 3-5 show that the strain energy of the braided skeleton is 173.5% higher than that of the stand-alone braided tube.

Table 3-5 Energy distribution in the structures in radial compression experiment

Structure	Parameter	Value (mJ)
Stand-alone braided tube	Elastic energy	15.98
	Friction dissipation	4.40
Manipulator	Elastic energy of skeleton	43.70
	Elastic energy of membrane	4.23
	Friction dissipation	22.55
Welded braided tube	Elastic energy	142.17
	Friction dissipation	3.76

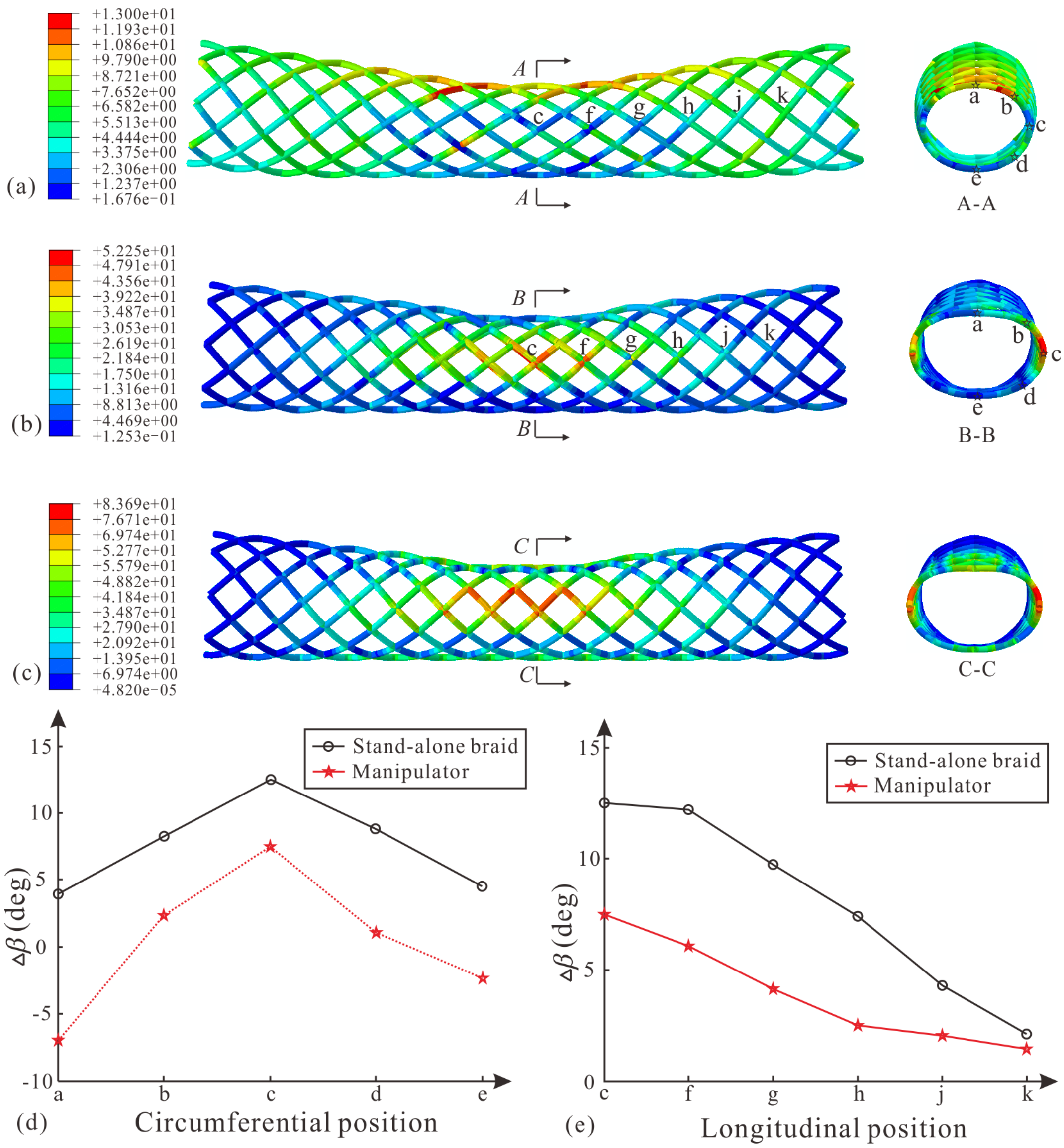

Figure 3-12 Mises stress contours of the (a) stand-alone braided tube, (b) the braided skeleton in the manipulator, and (c) the welded braided tube; changes in braiding angle at intersection points in the (d) circumferential direction and (e) longitudinal direction for the stand-alone braided tube and the manipulator.

To further explain the deformation mechanism of the braided skeleton in the manipulator, a welded braided tube in which the fibers are rigidly joined at intersections is also built and analyzed. As can be seen in Figure 3-12(c), the deformation mode and stress distribution are similar to those of the braided skeleton. The only major difference is that the stress is higher due to the stronger constraint at the intersection points. In comparison with the stand-alone braided tube, the elastic energy is dramatically increased by 789.7%.

Having understood the contribution by the braided skeleton, next we will study the role played by the membranes. The Mises stress contour of the deformed outer membrane resembles that of the inner one and is presented in Figure 3-13(a). The stress is found to be mostly below 10MPa and the elastic energy of the membranes as shown in Table 3-5 accounts for only 4.3% of the total energy in the manipulator. However, the membranes contribute to the radial stiffness of the manipulator in two ways. The first is to restrain rotation at the intersections of the braided skeleton, the effect of which has been demonstrated above. The second is through friction dissipation arising from sliding between the fibers and the membranes. Figure 3-13(b) shows the contact shear force, i.e., the friction, on the membrane. It can be seen that friction between the two constituents of the manipulator exists in the whole structure. And the area with friction is denser in the neighborhood of the loaded middle portion, indicating larger sliding between the fibers and the membranes. As seen in Table 3-5, the friction dissipation takes up 32% of the total energy, clearly demonstrating the effect of friction. Moreover, different from ordinary composites with a nearly perfect bonding between fibers and matrix, the friction serves two functions. First, it enables tunable stiffness of the structure, i.e., the larger the friction, the higher the radial stiffness. Second, it allows sliding between constituents during deformation, but the bonding interface is maintained by the negative pressure. As a result, the manipulator is expected to withstand larger deformation.

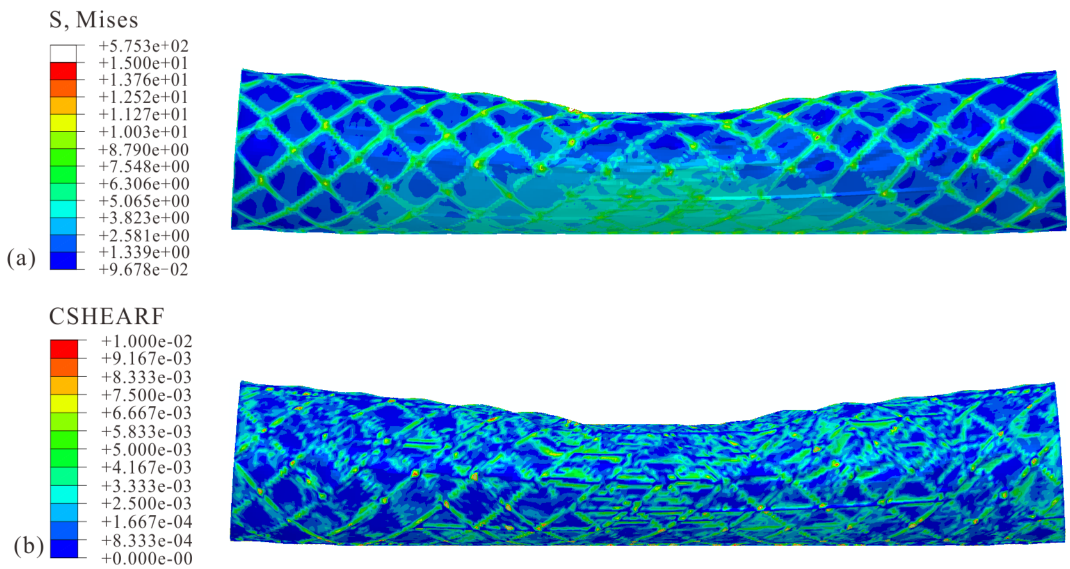

Figure 3-13 (a) Mises stress and (b) contact shear force contours of the inner membrane.

3.4.3 Parametric Analysis

It has been shown from Section 3.3.2 that the stiffness of the manipulator is affected not only by the stiffness of the braided skeleton and the membranes but also by their interaction through friction. In this sub-section, the effects of those design parameters are analyzed through a series of models of the stand-alone braided tube and the manipulator. They have a length of 100mm and a middle diameter of 20mm, and the other varied parameters are listed in Table 3-6. The reaction forces at a compression of 5mm were recorded and analyzed.

Table 3-6 Parameters of the numerical models for radial stiffness

Group	E_f(Gpa)	d(mm)	n	β (º)	E_m(Mpa)	b(mm)	P(Kpa)	μ
A	10-90	0.6	16	45	300	0.03	70	0.3
B	50	0.2-1.0	16	45	300	0.03	70	0.3
C	50	0.6	16-48	45	300	0.03	70	0.3
D	50	0.6	16	30-60	300	0.03	70	0.3
E	50	0.8	16	45	100-900	0.03	70	0.3
F	50	0.8	16	45	300	0.01-0.09	70	0.3
G	50	0.8	16	45	300	0.03	10-90	0.3
H	50	0.8	16	45	300	0.03	70	0.1-0.9

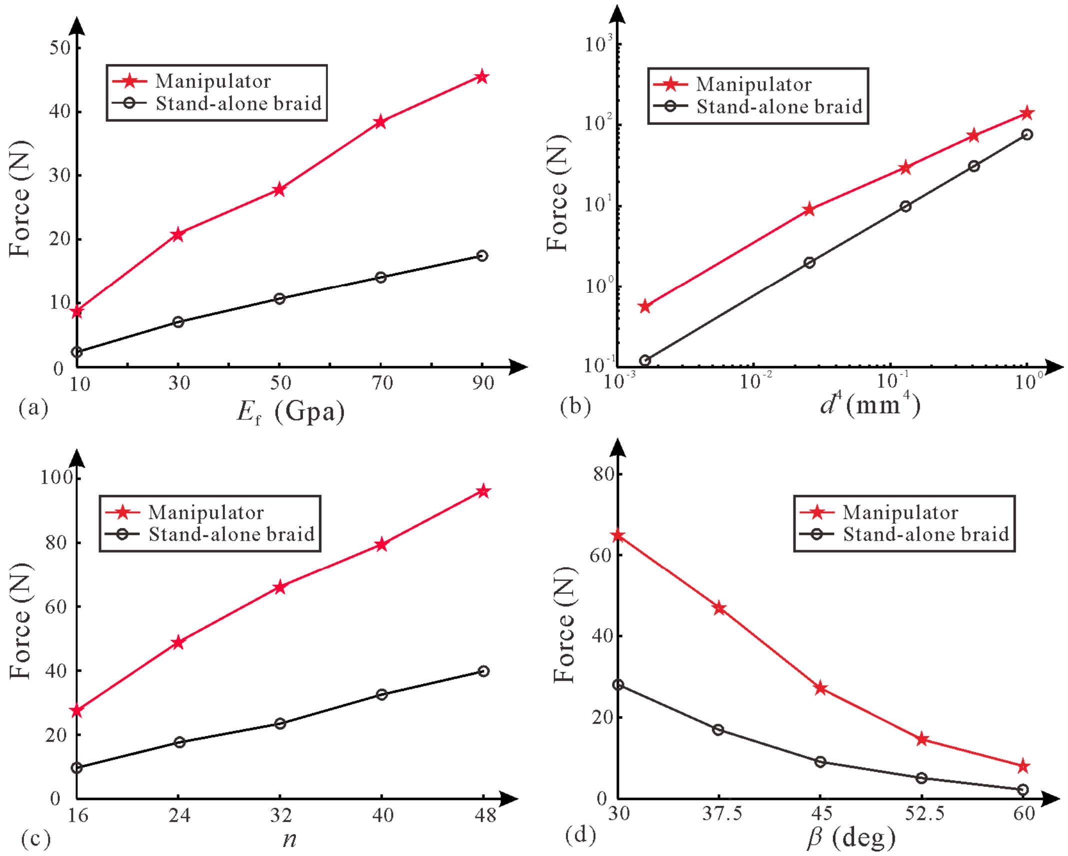

Figure 3-14 Effects of the braid parameters on the radial stiffness: (a) E_f, (b) d, (c) n and (d) β .

First, the effects of braided skeleton are looked at through model groups A-D. The radial forces of the manipulator against varying Young's modulus of the fiber E_f, diameter of the fiber d, the number of fibers n, and the braiding angle β, are respectively drawn in Figure 3-14(a-d). The radial forces of the stand-alone braided tube with identical parameters are also presented in the figures for comparison. It can be seen that the curves of the two structures present the same trend, further proving that a stiffer braided skeleton leads to a stiffer manipulator. In addition, the force of the manipulator increases with E_f, d^4, and n in a roughly linear manner. The reason is that during indentation, the fibers can be regarded as beams and mainly undergo bending. The bending stiffness of the fibers can be calculated as $\pi E_f d^4 / 64$, which is linear with E_f and d^4. And the larger n, the more fibers are bent, leading to higher structural radial stiffness. Furthermore, Figure 3-14(d) shows that a higher reaction force is obtained at a smaller β, and the relationship between the force and β is nonlinear. This is because the number of fiber coils contained in a length L can be calculated as

$$c = L / (\pi D \tan \beta) \tag{3-12}$$

At a smaller β, more fibers coils sustain the load, leading to a higher overall radial stiffness.

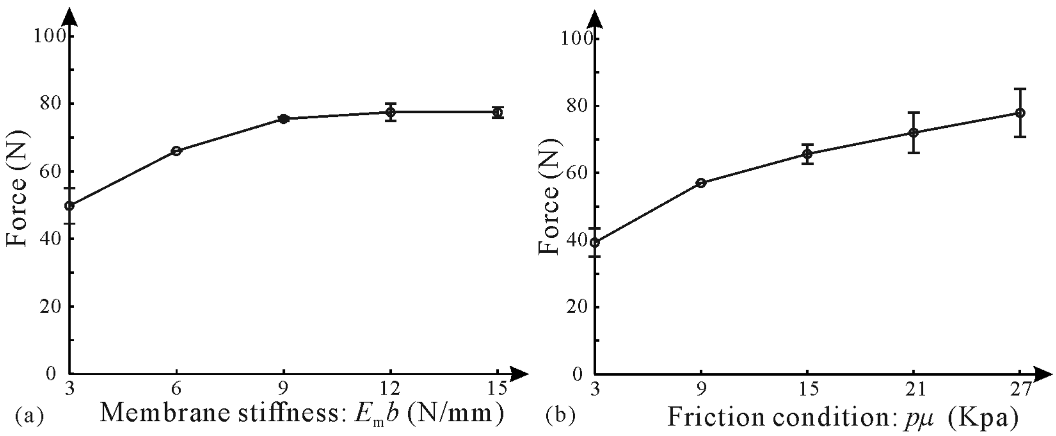

Figure 3-15 Effects of (a) membrane stiffness and (b) friction on the radial stiffness.

Second, the effects of membranes are investigated with model groups E and F. Since the membranes can only sustain tension, the membrane tensile stiffness $E_m b$ is considered in the investigation. The reaction forces of the manipulator with varying $E_m b$ are shown in Figure 3-15(a). The force is found to increase mildly at a smaller membrane stiffness but tends to reach a plateau when the membrane stiffness is relatively large.

Finally, the friction between the constituents are studied with model groups G and H. The friction has a linear relationship with negative pressure p and friction coefficient μ, and therefore the two parameters are considered collectively as $p\mu$. According to the result in Figure 3-15(b), the force of the manipulator increases substantially with $p\mu$, indicating that the stiffness of the manipulator can be widely tuned with negative pressure.

Understanding the effects of design parameters can provide guidance in the design of manipulators to satisfy engineering requirements. Based on the parametric analysis, the skeleton which contributes to most of the stiffness in flexible state, should not be too stiff. Reducing fiber diameter, Young's modulus and fiber number, as well as increasing braiding angle can achieve this. On the other hand, the stiffness in the rigid state should be improved. This can be achieved by a large membrane stiffness, friction, and negative pressure, without noticeably affecting the stiffness in flexible state.

3.5 Conclusion

In this chapter, a tunable stiffness mechanism of the manipulator has been proposed and analyzed, which takes a braided tube as the skeleton and uses sealing membranes to form a sealing cavity. The stiffness is tuned through negative pressure, under which the membranes constraints the fibers' movement greatly. At first it focuses on the bending stiffness. Experimental and numerical results indicate that in the flexible state, the braided tube and the membranes are loosely contacted, and the bending stiffness is predominantly provided by the braided skeleton. In the rigid state the membranes are compressed on the braided tube by creating a negative pressure inside, and the membranes are tensioned by the braided tube, leading to a stiffness ratio of 6.85 between the rigid state and the flexible state. Based on the experimental and numerical results, a theoretical model has been developed to calculate the bending stiffness in the rigid state, which agrees reasonably well with experiments. Furthermore, a parametric study has been conducted to investigate the effects of design parameters. It has been found out that the Young's modulus and thickness of the membranes which indicate membrane stiffness, and the negative pressure and friction coefficient between the tube and the membranes which indicate the friction force, are effective at improving the stiffness in the rigid state. The stiffness in the flexible state, on the other hand, is mainly determined by the parameters of the braided tube.

Next, the radial stiffness of the manipulator when subjected to lateral indentation have been studied experimentally and numerically. According to the experiments, the stiffness ratio between the rigid and flexible states of the manipulator is 3.9. It has been found out that the radial stiffness of the manipulator mainly arises from two deformation mechanisms. One is the restriction exerted on the braided skeleton by the membranes. It constrains the rotation of fibers at intersections and thus increases the stiffness of the skeleton. The other is the sliding between the fibers and the membranes, which leads to substantial friction dissipation in the structure. A parametric analysis has also been conducted to investigate the effects of design parameters on the radial stiffness. The results show that a stiff braided skeleton with large Young's modulus, diameter, number of fibers, but small braiding angle, stiff membranes with large Young's modulus and thickness, as well as large friction between them through high negative pressure and coefficient of friction, can lead to a manipulator with high resistance to lateral indentation.

Chapter 4 Tunable Diameter Actuation

4.1 Introduction

A bi-directional tunable diameter of the manipulator helps reduce the manipulation difficulty and patient discomfort during insertion and withdrawal. In this chapter, a tunable diameter actuation method has been proposed and validated through experiments on a braided skeleton, and the diameter tuning capability and heat response behavior have been analyzed. The layout of this chapter is listed as follows. In Section 4.2, the tunable diameter actuation design of the manipulator skeleton is introduced, and its material selection and fabrication process are also included. Section 4.3 analyzes the tunable diameter range through theoretical model and experiment. Based on the analysis of heat transfer, Section 4.4 studies the applicable electric current range and response time to actuate the diameter, and the effect of preheating on the response time is also looked into. The conclusion is finally given in Section 4.5.

4.2 Tunable Diameter Design

The tunable diameter mechanism of the manipulator can be interpreted with Figure 4-1, which shows the braided skeleton of the manipulator. It is composed of NiTi shape memory fibers, tubular coats and rubber bands. The NiTi fibers are one-way shape memorized, which can reshape themselves to be helixes with a large diameter when heated over their transmission temperature. Electrical heating method is adopted, and tubular coats are applied to the fibers for electrical insulation. Following the helical configuration, it is easy to braid the fibers manually on a mould. In this way, the obtained braided tube shares the same parameters with the helical fibers. Elastic rubber bands are then dressed on the outer surface of the braided tube, which are small circles and are tensioned on the tube.

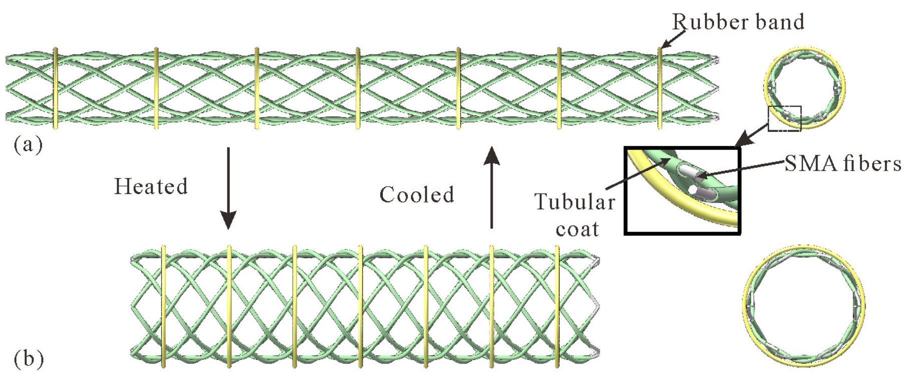

Figure 4-1 Tunable diameter mechanism of the manipulator: (a) folding state and (b) deploying state.

The NiTi fibers are flexible at room temperature, and the rubber bands are stiff enough to fold the tube, as shown in Figure 4-1(a). Whereas when electrical heating is applied, the fibers get much stiffer, and the tube expands in radial direction, tending to the pre-configured profile. As a result, the whole tube exhibits a larger diameter. When the heat is cancelled, the fibers are easy deformed again as the temperature drops. Finally, the whole structure recovers to the slim state under the rubber bands.

A prototype is first prepared, and there are three major fabrication processes for the manipulator skeleton. The first step is to design the shape memory effect. NiTi fiber is selected as the shape memory material for its substantial moduli difference between austenitic and martensitic phases [55]. The fibers are fixed in the helical grooves of a steel rod. After a heat treatment at 480^{o}C for one hour and cooling at room temperature, the fibers are helical-shaped, obtaining one-way shape memory at a phase transition temperature of 55^{o}C. The second step is to obtain the braiding fibers. To provide enough stiffness, double-braid configuration is adopted, and two fibers constitute one group. The two fibers are then inserted into a Teflon tube, which serves as a coat for electricity insulation. Thirdly, a braided tube is acquired using the fabrication method in Section 2.3.3. The braiding mould, the helical fibers, and the final braided skeleton share the same helical parameters. Thus, the braiding process is coordinated and the fibers in the skeleton keep their original configuration. The length, the outer diameter and the braiding angle of the final braided tube in the sufficiently heated state are 144.8mm, 26.0mm and 47.8^{o}, respectively.

The Young's modulus of the fibers at different electric currents is determined through tensile test, which is conducted on the Instron 5982 testing machine, following ASTM F2516-14. Numerical result based on the *Abaqus* simulation shows that the maximum strain of the braiding fibers during the diameter changing process is 0.6%. Thus, the stress in the strain range of 0-0.6% is considered and the stress versus strain curves are presented in Figure 4-2(a). It can be seen that the curve at no current is perfectly linear and that at a current of 2A bends slightly but never reaches a plateau. Here, the material is regarded to be linearly elastic, and the Young's modulus is calculated using linear fitting based on the experimental results and listed in Table 4-1.

Electrical heating method is adopted to simplify the control system, and a new configuration of the braided tube is designed. As shown in Figure 4-2(b), the fiber ends are connected one by one with electric wires: a dextral fiber is connected to a sinistral one. As a result, all fibers form a single circuit, controlled by a power supply. Connections between the fibers and the wires are fastened with compression, and thus have a good strength. Rubber tube is coated at the joint for insulation. In addition, the rubber bands are uniformly distributed on the outer surface of the tube, obtaining the final physical model. All parameters are listed in Table 4-1.

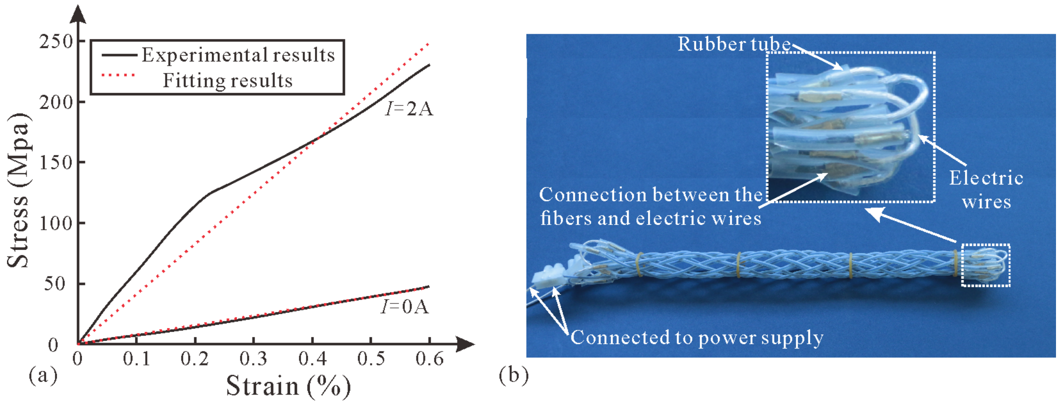

Figure 4-2 Experimental specimen: (a) experimental strain-stress curves of the NiTi fibers at different electric currents; (b) physical model of the braided tube with tunable diameter.

Table 4-1 Parameters of the physical model for tunable diameter

Parameter	Value
Tube length, L	144.8mm
Tube outer diameter, D_o	26.0mm
Fiber number, n	12×2
Fiber diameter, d	0.5mm
Braiding angle, β	47.8°
Fiber Young's modulus E_f	41.56Gpa (at I=2A) 7.76Gpa (at I=0A)
Tubular coat outer diameter, d_c	1.6mm
Tubular coat inner diameter, d_i	1.2mm
Rubber band length, cr	32mm
Rubber band elasticity E_w	0.77
Number of the rubber bands, m	4
Density of the rubber band distribution, L/m	36.2mm

4.3 Diameter Range

4.3.1 Theoretical Model

NiTi alloy outstands for its phase change between austenite and martensite, which makes it exhibit the greatly different Young's modulus. The phase change process is complicated despite that many theoretical models have been proposed. What's more, here the theoretical model does not focus on the dynamic results but only concerns the final diameter range. Therefore, to simplify the problem, the heat transmission process is ignored, and the braided tube is assumed to be cooled down instantly. In addition, the effect of the Teflon cover is not included.

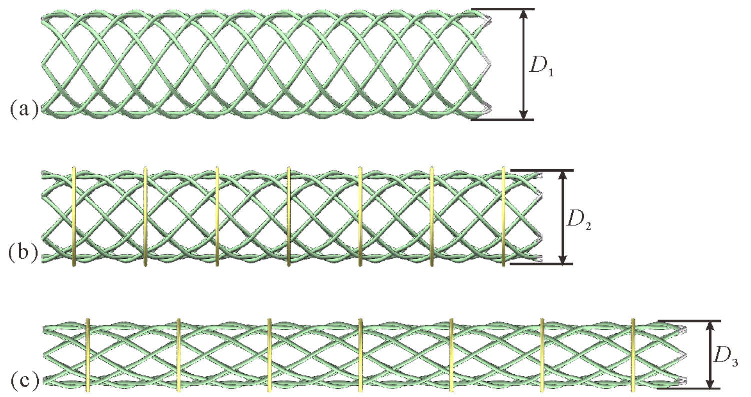

Figure 4-3 Diameters of (a) fully deployed braided tube, (b) deployed skeleton and (c) folded skeleton.

With the above assumptions, the tunable diameter mechanism can be explained with Figure 4-3. Figure 4-3(a) presents the fully deployed braided tube with a diameter of D_1. It is heated and the fibers have a Young's modulus of E_1. As in the case of the manipulator skeleton shown in Figure 4-3(b), the rubber bands are covered on the outer surface, which compress the tube from its original diameter D_1 to the largest diameter D_2 of the manipulator. When heating is stopped, the tube cools down and the Young's modulus decreases to E_2. At this circumstance, the cooled tube obtains its stress-free diameter D_2, and it is forced to be slimmer by the rubber bands. Finally, the diameter reaches the bottom of the range, the smallest diameter D_3. Therefore, D_1 is determined by the heat treatment process during the fabrication, whereas D_2 and D_3 are determined by the relationship between the stiffness of the braided tube and the load caused by the rubber bands.

Next, equations for the relationships between the radial load and the diameter of both the braided tube and the bands are focused. The equation for the braided tube is given by Jedwab and Clerc [79] as follows:

$$\begin{cases} P_{\mathrm{b}} = \dfrac{4n\cos^2\beta}{\pi D^2 \sin^2\beta'}\left[\dfrac{2GI\cos\beta'}{K_3}\left(\dfrac{2\sin\beta'}{K_3}-K_1\right)-\dfrac{EI\tan\beta'}{K_3}\left(\dfrac{2\cos\beta'}{K_3}-K_2\right)\right] \\ D_{\mathrm{b}} = D\cos\beta' / \cos\beta \end{cases} \tag{4-1}$$

where $K_1 = \sin 2\beta / D$, $K_2 = 2\cos^2\beta / D$, $K_3 = D/\cos\beta$, P_{b} and D_{b} are respectively the radial pressure and diameter of the tube, and deformed parameters are denoted with a prime. Thus, the relationship between P_{b} and D_{b} can be determined at a given original configuration of D, β and E_{f}, and expressed as $P_{\mathrm{b}} \sim D_{\mathrm{b}}(D, \beta, E_{\mathrm{f}})$. As for the radial compression pressure of the rubber bands, based on the material mechanics, it can be calculated as

$$P_{\mathrm{r}} = \frac{2mE_{\mathrm{w}}(D_{\mathrm{r}}/D-1)}{D_r L'} \tag{4-2}$$

and expressed as $P_r \sim D_r(D, E_w)$. In the equation, P_r and D_r are respectively the radial pressure and diameter of the bands. The bands cover the outer surface of the braided tube, and following equations can be acquired

$$P_b = P_r \tag{4-3}$$

$$D_b = D_r - 2d_c \tag{4-4}$$

Solving the four unknown variables including P_b, P_r, D_b and D_r with Eqs. (4-1)-(4-4), the final diameter can be determined at a given original configuration including diameter, braiding angle and Young's modulus of the fibers and the bands. Therefore, the largest and the smallest diameters can be calculated as $D_2(D_1, \beta_1, E_1, E_w)$ and $D_3(D_2, \beta_2, E_2, E_w)$, respectively.

4.3.2 Experimental Setup

The NiTi braided tube was heated with a power supply which can provide a constant current, as shown in Figure 4-4. All the fibers can be charged at the same time. When the temperature of the structure got to be stable, the phase change process was completed, and the shape of the braided tube was fixed. The outer diameter was recorded as the maximum diameter and the heating was then stopped. The tube was left to be gradually cooled at the room temperature. When it returned to the slim configuration, the outer diameter was recorded as the minimum diameter.

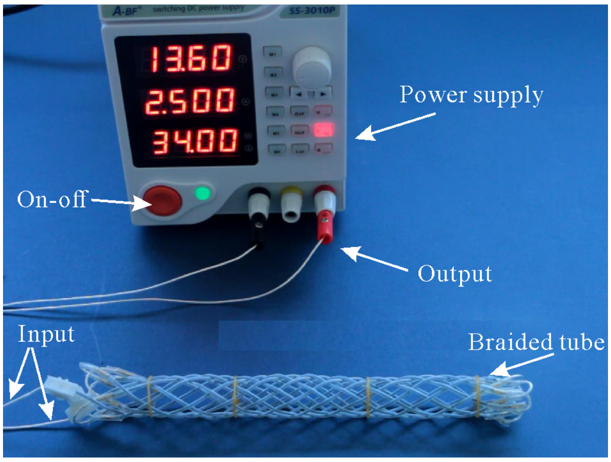

Figure 4-4 Experimental setup for the tunable diameter.

4.3.3 Results

The experimental diameter range is shown in Figure 4-5. Figure 4-5(a) presents the skeleton heated by an electric current of 2.0A, which has an average diameter of 21.4mm. When cooled down, it recovers to the slim state shown in Figure 4-5(b), whose diameter is 14.7mm.

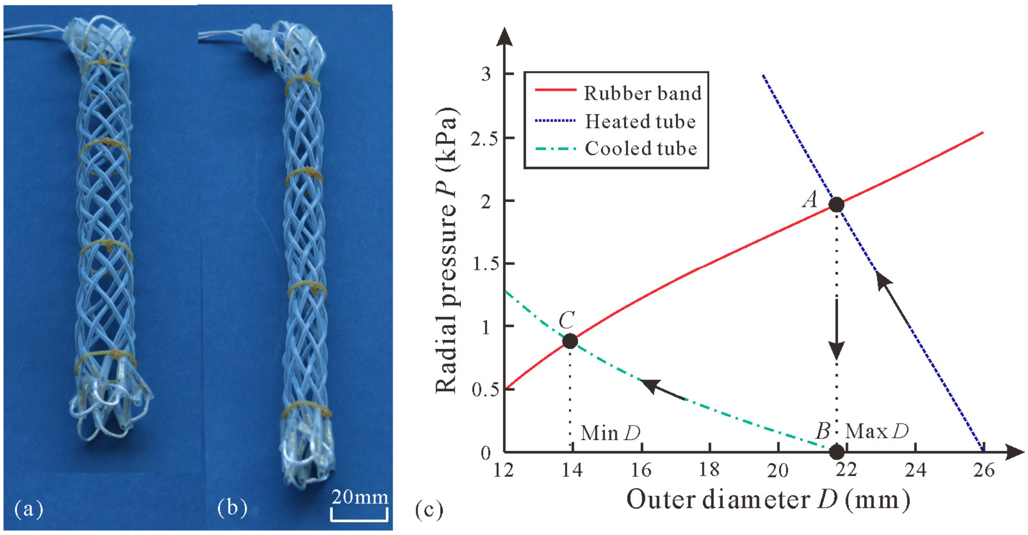

Figure 4-5 Diameter range: experimental (a) maximum diameter and (b) minimum diameter; (c) theoretical relationships between the outer diameter and the radial load of the ring and tubes.

The theoretical results are presented in Figure 4-5(b). In the figure, the pressure versus diameter curves of the rubber band and the heated tube meet at point A, forming a stable diameter of 21.7mm, i.e., the maximum diameter. With the assumption that the phase change process is completed instantly, the state changes from point A to point B, which share the same geometrical parameters. Then, following the curve of the cooled tube, the diameter decreases to the point C, where curves of the cooled tube and the rubber band meet. The minimum diameter is 13.9mm. Table 4-2 lists the errors between the theoretical and the experimental results for the maximum and minimum diameters, which are respectively 1.40% and 5.44%, validating the theoretical model.

Table 4-2 Results of the diameter range

Diameter	Experimental value	Theoretical value	Error
Maximum	21.4mm	21.7mm	1.40%
Minimum	14.7mm	13.9mm	5.44%

With the theoretical model, parametric analysis is conducted to analyze the effects of rubber bands on the tunable diameter of the skeleton. The concerned parameters include the elasticity, the distribution, and the circumference of the rubber bands, and the results are presented in Figure 4-6. It can be seen in Figure 4-6(a) that both the maximum and the minimum diameters decrease with the elasticity of the rubber bands. However, the width of diameter range is not monotone and with a maximum at the elasticity of around $0.6\mathrm{N}/\varepsilon$. With soft bands, the compression is too limited to force the cooled tube to be compacted. In contrast, if the bands are too stiff, the heated tube will have difficulty in resisting the large compression. Therefore, the elasticity of the band should be moderate. Figure 4-6(b) analyzes the effects of distribution, which is the average length of the tube for per band. A higher distribution means fewer rubber bands. Because both distribution and elasticity directly affect the compression with the same mechanism, the effects of the distribution are similar as the elasticity. The distribution should not be too large nor too small. Figure 4-6(c) shows variation of the diameters with the circumference. It can be seen that the width of diameter range is higher at a smaller band circumference. At a smaller circumference, the bands can still provide compression to a slim tube because of the larger strain. Therefore, the minimal diameter decreases more obviously, leading to a larger width of diameter range.

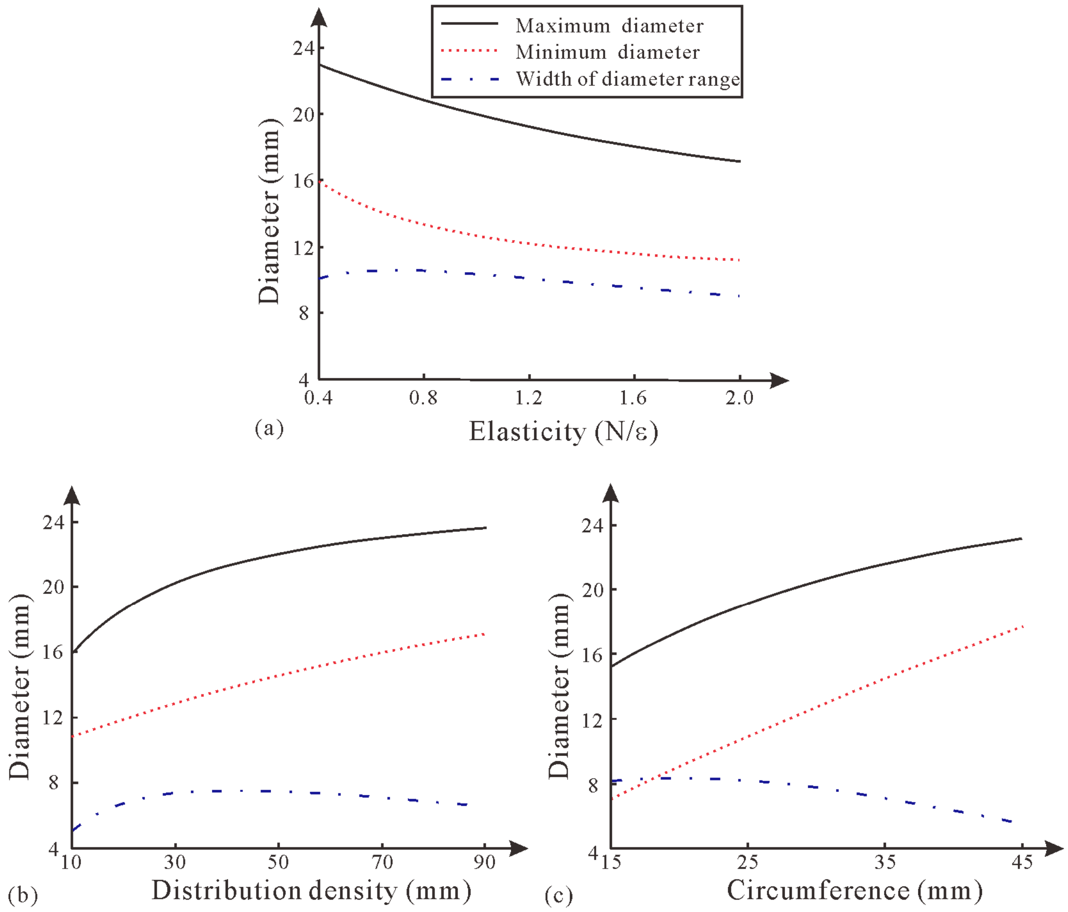

Figure 4-6 Effects of (a) the elasticity, (b) the distribution and (c) the circumference of the rubber band on the diameter range.

4.4 Heat Response

The skeleton varies its outline when the temperature exceeds the phase transition temperature of the NiTi shape memory fiber. In accordance with heat transfer analysis, distributions of steady and transient temperatures in the braiding fiber are studied, presenting the applicable current range and the response time, respectively.

4.4.1 Theoretical Model: steady state

In the design, double-braiding configuration is adopted and two NiTi fibers are inserted into one tubular coat, forming the braiding fiber. The NiTi fiber diameter is 0.5mm, and the inner diameter of the coat is 1.2mm. The two fibers fill the coat, and the relative position of the two NiTi fibers (shown in Figure 4-7(a)) does not matter and remains random. From this perspective, the two NiTi fibers are simplified as one tubular fiber with the same profile area as that of the two fibers. The outer diameter of the tubular fiber is the same as the inner diameter of the coat, and the outer surface contacts the inner wall of the coat uniformly (shown in Figure 4-7(b)). The inner diameter of the tubular fiber d' is determined by calculating the profile area, as

$$d' = \sqrt{d_{\mathrm{i}}^2 - 2d^2} \tag{4-5}$$

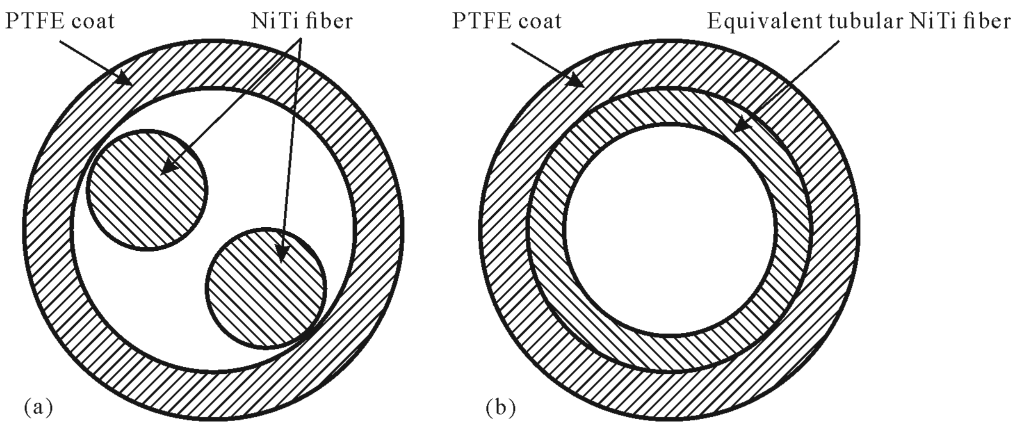

Figure 4-7 (a) Actual and (b) simplified profiles of the braiding fiber.

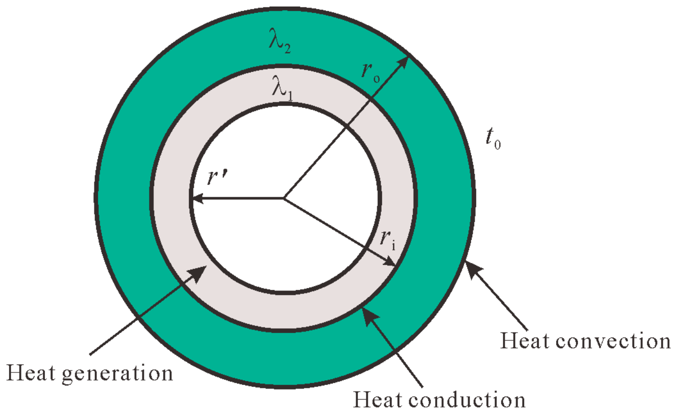

Figure 4-8 Diagram of the heat transfer on the braiding fiber profile.

The fiber is slender and the temperature along the fiber length keeps unchanged. The analysis of steady-state heat transfer is conducted to know the temperature in the profile, as its schematic diagram shown in Figure 4-8. The heat is generated by the thermo-electric effect of the NiTi fiber, then conducted to the tubular coat, and finally released to the environment through heat convection.

In light of Joule's law, the heat generated in a NiTi fiber with a finite length dl can be described as

$$\phi = I^2 \nu \mathrm{d}l / \pi(r_\mathrm{i}^2 - r'^2) \tag{4-6}$$

where I is the electric current; ν is the electrical resistivity of the NiTi fiber. Therefore, the heat generated in unit volume can be expressed as

$$\phi_\mathrm{v} = \phi / \pi(r_\mathrm{i}^2 - r'^2)\mathrm{d}l = I^2 \nu / \pi^2 (r_\mathrm{i}^2 - r'^2)^2 \tag{4-7}$$

At $r=r_\mathrm{i}$, heat flux q_r can be calculated as

$$q_\mathrm{r} = \phi / (\mathrm{d}l 2\pi r_\mathrm{i}) = I^2 \nu / 2\pi^2 r_\mathrm{i} (r_\mathrm{i}^2 - r'^2) \tag{4-8}$$

In a one-dimensional steady-state heat transfer problem and at a cylindrical coordinate system, the differential equation of heat conduction can be written as [114]

$$\lambda \frac{\mathrm{d}}{\mathrm{d}r}\left(r \frac{\mathrm{d}t}{\mathrm{d}r}\right) + r\phi_\mathrm{v} = 0 \tag{4-9}$$

For the NiTi fiber, its heat conductivity coefficient is λ_1, and its temperature distribution can be derived from Eq. (4-9) as

$$t_1 = C_1 \ln r - \phi_\mathrm{v} r^2 / 4\lambda_1 + C_2 \tag{4-10}$$

where C_1 and C_2 are two constants to be determined. For the tubular coat, without heat generation, its heat conductivity coefficient is λ_2. Temperature distribution in the coat can be calculated as

$$t_2 = C_3 \ln r + C_4 \tag{4-11}$$

where C_3 and C_4 are another two unknown constants. Thus, the heat flux in the NiTi fiber and the coat can be calculated as

$$\begin{aligned} q_1 &= -\lambda_1 \mathrm{d}t_1 / \mathrm{d}r = C_1 \lambda_1 / r - \phi_\mathrm{v} r / 2 \\ q_2 &= -\lambda_2 \mathrm{d}t_2 / \mathrm{d}r = -\lambda_2 C_3 / r \end{aligned} \tag{4-12}$$

To determine the four unknown constants, boundary conditions are summarized as follows:

1) At $r=r_\mathrm{i}$, the heat flux calculated using Eq. (4-12) is the same as the generated heat flux.
2) At $r=r_\mathrm{i}$, temperatures of the NiTi fiber and the coate are the same.
3) Ar $r=r_\mathrm{c}$, the heat flux is the same as the amount released by heat convection.

Therefore, the boundary conditions can be expressed as

$$\begin{cases} q_1 |_{r=r_i} = q_r \\ q_2 |_{r=r_i} = q_r \\ t_1 |_{r=r_i} = t_2 |_{r=r_i} \\ q_2 |_{r=r_c} = h(t_2 |_{r=r_c} \text{-} t_0) \end{cases} \tag{4-13}$$

where h is the coefficient of heat transfer; t_0 is the environment temperature.

With Eqs. (4-10), (4-11) and (4-13), the temperature distribution in the whole braiding fiber profile can be calculated as

$$t = \begin{cases} t_1 = \text{-}\phi_v r^2 / 4\lambda_1 + \dfrac{I^2 v}{2\lambda_2 \pi^2 (r_i^2 - r'^2)} [\dfrac{\lambda_2}{r_c h} + \ln(r_c / r_i)] + t_0 \\ \qquad + \phi_v r_i^2 / 4\lambda_1 - \dfrac{I^2 v r'^2}{2\lambda_1 \pi^2 (r_i^2 - r'^2)^2} \ln(r_i / r) & (r < r_i) \\ t_2 = \dfrac{I^2 v}{2\lambda_2 \pi^2 (r_i^2 - r'^2)} [\dfrac{\lambda_2}{r_c h} + \ln(r_c / r)] + t_0 & (r_i \le r \le r_c) \end{cases} \tag{4-14}$$

4.4.2 Numerical Model

Coupled thermal-electric analysis step is utilized to capture the heat response of the braiding fiber. The numerical model is composed of a Poly tetra fluoroethylene (PTFE) coat and a NiTi fiber, which is shown in Figure 4-9. Merely the heat transfer in the profile is considered, and only one element is set in the longitudinal direction of the fiber. The NiTi fiber is charged by defining the surface current on its two ends. Additionally, heat convection on the outer surface of the coat is considered and film condition is defined. In a heat transfer by free convection, the coefficient of heat transfer of a tubular rod is temperature-dependent, and can be calculated as [114]

$$h = 1.34\left(\Delta t / d_c\right)^{0.25} \tag{4-15}$$

where Δt is the temperature difference between the coat outer surface and the environment. In addition, thermal conduction is defined to happen between the outer surface of the NiTi fiber and the inner diameter of the coat. Upon convergence analysis, a mesh size of 0.04mm is set along the radial direction, and one hundred elements are set along the circumferences of the fiber and the coat. Step time is 0.2 in each increment.

Heat transfer element DC3D8 and thermal electric element DC3D8E are selected to define the coat and the fiber, respectively. Thermal parameters of the materials including NiTi alloy and PTFE are obtained from references, and they are listed in Table 4-3. The environment temperature is 25°C.

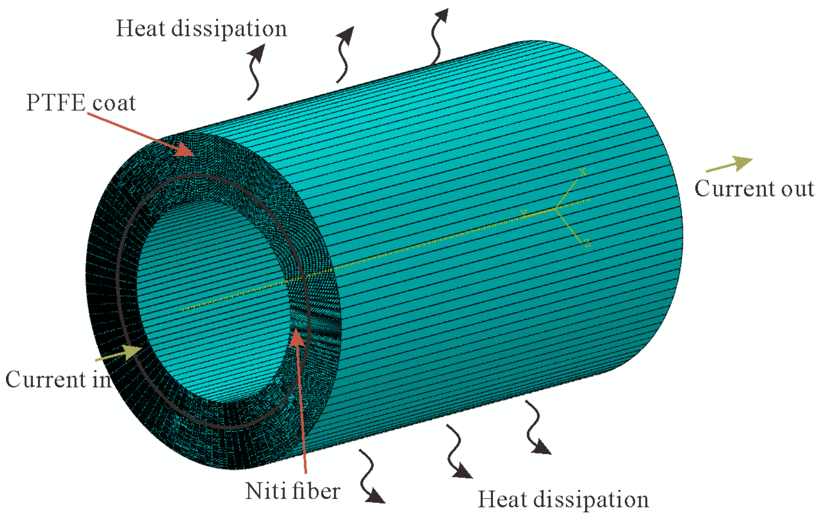

Figure 4-9 Numerical model for the heat transfer.

Table 4-3 Thermal parameters in the heat transfer simulation

Parameter	NiTi fiber [115, 116]	PTFE coat [117]
Coefficient of heat conduction	18W/m°C	0.25W/m °C
Specific heat capacity	837J/kg°C	1050J/kg°C
Density	6.45g/cm^3	2.2g/cm^3
Current	2A	-
Electrical resistivity	$8.2\times10^{-7}\Omega$m	-

4.4.3 Experimental Setup

In experiment, the response time was determined based on the deployment of the skeleton. To detect the shape change of the skeleton, cantilever test condition was established and the force versus displacement curve was focused on. One end of the skeleton was fixed and the other was forced downwards with a force sensor at a constant movement speed of 10mm/min. The braided tube was charged during the loading process and the force was observed.

4.4.4 Results

Steady temperature: applicable electric current

The steady temperature after being heated for enough time is first analyzed, and both theoretical and numerical results are presented in Figure 4-10. At the first beginning, the theoretical result gives a temperature range of 107.0~108.6°C, and the maximum temperature difference is only 1.6°C. The thickness of the coat is 0.2mm, whose material is not heat-insulated. A coat with better performance in heat insulation can decrease the temperature on the outer surface of the braiding fiber. Later, the temperature range obtained from the numerical simulation is 107.3~108.8°C. The theoretical result is consistent with that from the numerical model.

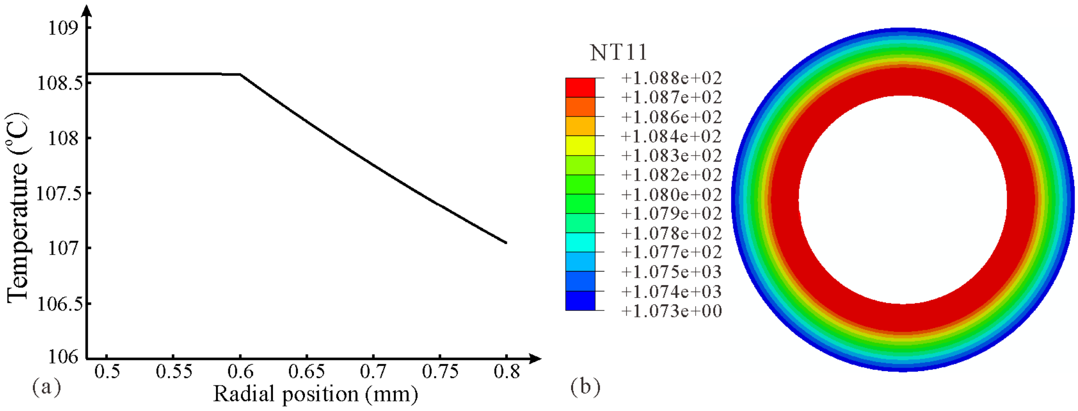

Figure 4-10 Steady temperature in the braiding fiber profile: (a) theoretical temperature versus radial position curve; (b) numerical temperature distribution in the profile.

Next, as the theoretical result shown in Figure 4-11, steady temperatures at different electric currents are analyzed. It can be seen that the steady temperature increases slowly at a low current but shows a faster increase at a higher current. At a lower current, the generated heat is insufficient. The steady temperature reaches the phase-transition temperature 55°C at a current of about 1.1A. Accordingly, an electric current below 1.1A is not applicable to the tunable diameter actuation. In contrast, at a very high current, the steady temperature successfully exceeds the phase-transition temperature, but it is too high for the human body. It requires a current control system to interrupt the heating process to avoid the overheating as soon as the transmission temperature is reached, and a good heat insulation cover to protect the patient.

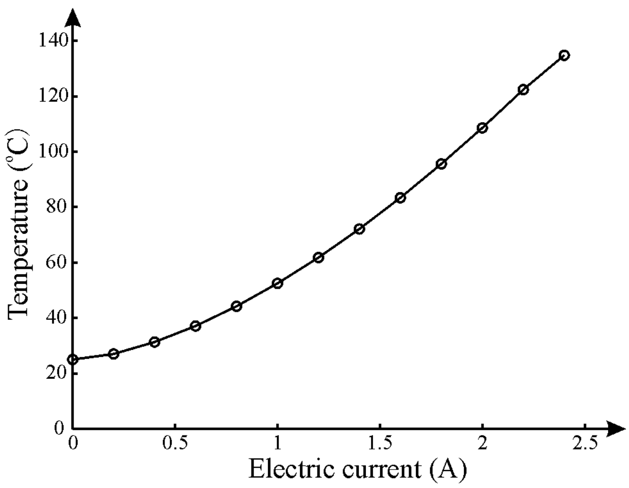

Figure 4-11 Electric current versus steady temperature curve.

Transient temperature: response time

The relationship between experimental reaction force and loading time is presented in Figure 4-12. It is clear that the reaction force increases linearly until the tube is heated. At a constant loading speed, the linear stage shows a constant force increment rate. When the tube is heated, the force drops greatly for the generated disturbance, and then increases sharply. There are two reasons for the sharp increase. One is the increase of the Young's modulus of the fibers, contributing a larger overall stiffness. The other is the deployment of the tube. When the sensor compresses the tube, the tube is also deploying to the sensor, leading to a larger compression. However, when the deformation process is completed, the whole system gets stable, and the curve returns to be a linear configuration. The time it takes the system to return stable is regarded as the response time, which is about 20s in this case.

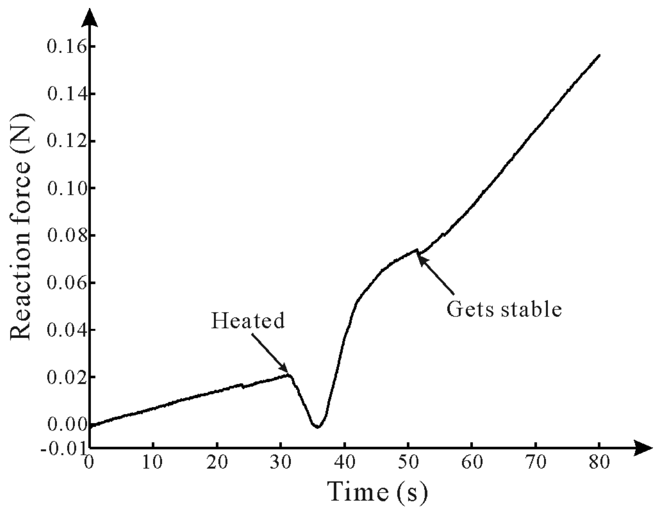

Figure 4-12 Experimental response time determination: force versus time curve under tip load.

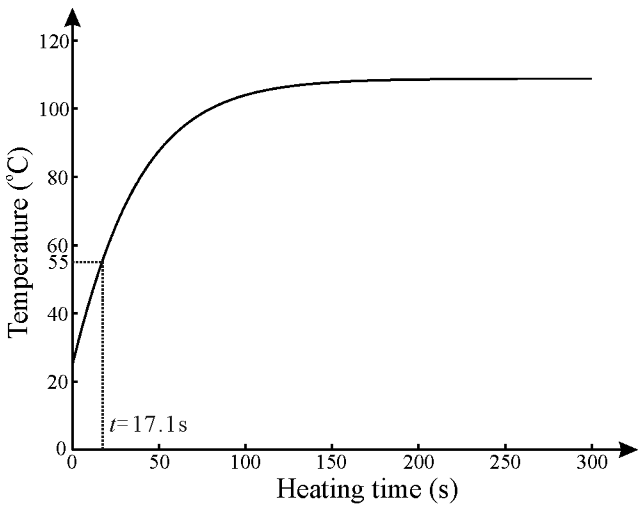

Figure 4-13 Heating time versus temperature curve.

The response time is also analyzed by looking into the temperature of the NiTi fiber. The relationship between the heating time and the temperature on the outer surface of the NiTi fiber is exported from the numerical simulation and presented in

Figure 4-13. It can be seen that the temperature increases sharply at first, and finally keeps constant. It takes 17.1s to reach the transition temperature, at which the phase change of the NiTi alloy starts. This result basically reaches a consensus with the experimental result, validating the numerical model further.

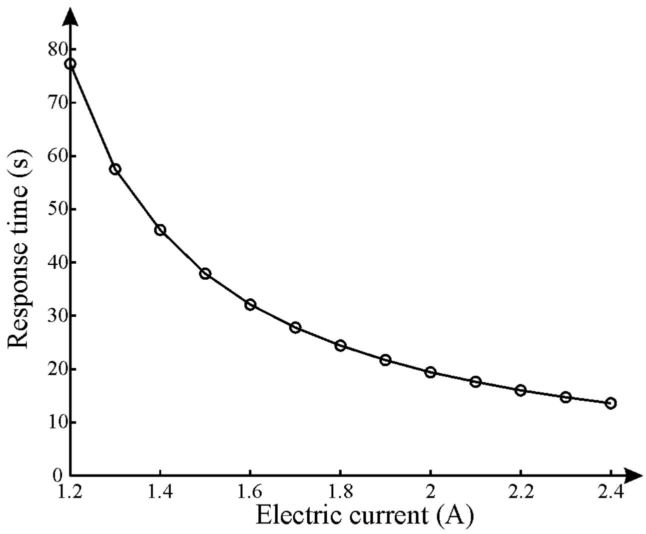

Figure 4-14 Electric current versus response time curve.

Based on the numerical method, response times at different electric currents are studied, and the results are shown in Figure 4-14. At a low current of 1.2A, it takes 77.3s to response. The response time decreases with the increase of the electric current, especially when the current is not high enough. This tendency is in keeping with Eq. (4-7), which illuminates how the current affects the efficiency in heat generation. The electric current cannot remain too low because it takes too much time to response, which is not ideal in medical surgery. However, it should not be too high, because at a higher current, increasing the current cannot cut the response time down too much, and it puts forward higher demands for the system reliability, meanwhile posing a higher risk in overheating.

Effects of preheating

To cut down the response time requires to reduce the time it takes the temperature to increase from initial temperature to the transition temperature. A preheating can facilitate increasing the initial temperature and reducing the temperature increment needed during the heating process, thus reducing the response time. Based on the numerical method, response times at different initial temperatures are analyzed, and the results are presented in Figure 4-15. It can be seen that the response time decreases with the increase of the initial temperature, and the tendency is linear. At an initial temperature of 37 °C which is definitely safe to the patients, the response time is only 9.8s. As a matter of fact, with a better heat insulation cover, the initial temperature can be further increased to decrease the response time.

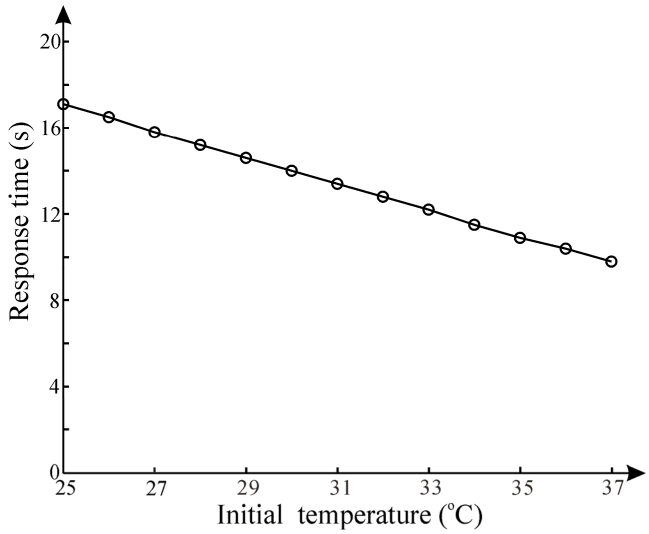

Figure 4-15 Response time versus initial temperature curve at a constant electric current of 2A.

4.5 Conclusion

In this chapter, the method of bi-directional tunable diameter actuation has been proposed. A prototype manipulator skeleton has been developed with NiTi shape memory fibers. With a delicate braiding pattern, the braiding fibers form a single circuit, which can be charged by a power supply simultaneously. According to the experiments, the braided skeleton can achieve a tunable diameter range of 14.7mm to 21.4mm. A theoretical model for the diameter range is also built. In compliance with this, a parametric analysis of the rubber band setup has been conducted, displaying that the skeleton can achieve a diameter ratio of 1.6 at optimized parameters. In addition, the analysis of heat transfer has been conducted to obtain the applicable electric current range and the response time. The steady-state heat transfer analysis reveals that the current has to exceed 1.1A to reach the transition temperature. The deployment experiment indicates that 20s is needed to activate the skeleton. Transient-state heat transfer analysis has been conducted based on the numerical model, which finds that a higher current and a preheating can help reduce the response time. At an initial temperature of 37°C and a current of 2A, the response time can be reduced to be less than 10s. This chapter enables the diameter of the manipulator skeleton to be tuned in double directions.

Chapter 5 Prototype and Performance Test

5.1 Introduction

Former chapters have studied the mechanical behaviors of the braided skeleton, validated the tunable stiffness mechanism, proposed the tunable diameter actuation method, and established a theoretical framework for the tunable properties. Taking them as a basis, at the outset, this chapter gives a design rule for the braided manipulator, following which a prototype is developed. The workflow of the manipulator is given, which comprehensively combines the tunable stiffness and the tunable diameter. Next, the performances of the prototype are characterized through an in vitro test and a theoretical calculation. According to its performance and fabrication challenges, strengths and limitations of the manipulator are summarized. The conclusion is given at last.

5.2 Prototype Fabrication

5.2.1 Parameter Design

Parameters of the manipulator shall be carefully designed to meet the application requirements. In this sub-section, design considerations are summarized, which involve geometry of the braided skeleton, tunable stiffness range and tunable diameter actuation.

Geometry of the skeleton

For starters, an intact profile along the body orifice should be provided, whereas the braided tube may collapse when bent severely. According to the analysis in Section 2.3, the braiding angle has the largest effect on the collapse behavior, and the fiber number plays the second vital role. In addition, the fiber number cannot be tuned casually when the tube is fabricated on a machine. From this point, it is more ideal to determine a braiding angle to guarantee an intact profile. The numerical results in Section 2.3 show that a braiding angle smaller than 48.5^{o} can basically provide an intact profile at a fiber number of twelve. Considering that the collapse extent increases with fiber number, the critical braiding angle should be adjusted to be smaller at a larger fiber number, and vice versa. In application, the braiding angle is supposed to be larger than 30^{o}, or it will make the fibers jam together and affect the deployability. Thus, the braiding angle should be within the range of 30^{o}-48.5^{o}.

Next it concerns the deployability. In the design, manual fabrication process has to be selected to avoid the large stress on the shape memory fiber during the fabrication. To ease the manual fabrication, a smaller fiber number and a mandrel dimeter about 20mm are more appealing. With the diameter range equation proposed in Section 2.2, the diameter range of the manipulator at a mandrel diameter of 20mm and a braiding angle of 45^{o} can be estimated as 10.5mm-28.2mm, which can meet the application requirements.

A sufficient longitudinal stiffness is vital in avoiding improper deployment during insertion, and a hybrid braiding pattern can improve the performance. A hybrid braided tube can exert a higher longitudinal stiffness at a higher hybrid ratio. At this aspect, the human body orifice is deformable and its longitudinal resistance has not been detected. Thus, the requirement in longitudinal stiffness is not quantitatively determined. In this design, a uniform braiding pattern is adopted to fabricate the manipulator prototype. It can adapt to the 3D-printed tortuous orifice in the performance test in Section 5.3 and validate the feasibility of the manipulator design.

Finally, other geometrical requirements such as covering factor and thickness are focused. The covering factor is the ratio of the fiber coverage to the outer surface area of the braided skeleton. It is dominated by the number and diameter of fiber. At a higher covering factor, the relative movement between the fibers will be interfered, thus reducing the deployability. Hence, a smaller fiber number is ideal, and a fiber number of twelve can guarantee the stability of the structure. For another, a small thickness is also fine because it can save room for the following surgical instrument. As Figure 2-1 shows, if the membrane thickness is ignored, the manipulator thickness will be two times of the fiber diameter ($2d$). To provide a suitable bending stiffness in flexible state, two NiTi fibers with a diameter of 0.5mm are used to form one braiding fiber, and the diameter of the outer surface of their coat is 1.4mm.

Tunable stiffness range

The tunable stiffness accounts for the adoption of the manipulator. As analyzed in Chapter 3, the stiffness range is related to the sealing membranes, the negative pressure, the braiding fiber and the braiding configuration. What is meaningful is that the effects of the membranes and the pressure are ignorable in the flexible state, since they only affect the stiffness in the rigid state. Thus, it is valuable to strengthen the roles of these two components. The maximum value of the negative pressure is 101Kpa, which cannot be improved further. Accordingly, it is vital to improve the roughness of the membranes to increase the frictional interaction. The prototype here is to validate its feasibility and to save the fabrication cost, ordinary PTFE membrane with no additional surface treatment is adopted. The coefficient of friction of the membrane is about 0.3. In addition, stiffer membranes help increase the stiffness in the rigid state. Here, PTFE membrane is selected for its good heat durability, and the membrane stiffness is tunes through changing the membrane thickness. According the test results in Section 3.3, a membrane thickness of 0.05mm can provide a sufficient membrane stiffness.

In contrast, the other two components, including braiding fibers and braiding configuration, are not suggested to be tuned for a higher stiffness purpose. On the one hand, the two are also related to the stiffness in the flexible state, so tuning them can also increase the lower limit of the stiffness range. On the other hand, they have a correlation with the diameter range and other behaviors of the manipulator.

Tunable diameter actuation

The tunable diameter is achieved by the interaction between the shape memory tube and the rubber bands. According to Figure 4-5(c), the two stiffness curves of the skeleton directly affect the two intersections in the figure. Namely, a greater difference in Young's modulus between the two phases of the NiTi alloy can efficiently widen the diameter range. However, it requires experience and facilities in NiTi alloy fabrication. That is, optimizing the material property is more applicable at a large-scale production stage. Furthermore, the memorized shape of the fibers is significant because it determines the upper limit of the diameter range, which can be tuned through changing the configuration of the braiding and heating mould. The properties and distribution of the rubber bands also play a role in the diameter range by affecting their stiffness curve, as shown in Figure 4-5(c). Optimizing the rubber bands setup is the most efficient way to achieve a larger diameter range for it is easily available and assembled. It is worth mentioning that the braiding configuration also affect the stiffness curves of the skeleton. However, its effects are not as obvious as those of the fiber materials, and the two curves have to be moved simultaneously, making the method less efficient. In conclusion, the memorized shape should be selected first, and then the rubber bands should be optimized. Material design can be considered at a large-scale production. In the design, the memorized diameter is set slightly larger than that of the esophagus as 26mm. The number and circumference of the rubber bands are determined by calculating the stiffness relationship between the braided skeleton and the rubber bands, like that in Figure 4.5.

In applications, determination of the manipulator design parameters is a multi-objective task. As Figure 5-1 shows, three major aspects should be considered, which involve geometrical requirements, stiffness range and diameter range. In addition, the manipulator is constituted by five components, including sealing membranes, negative pressure, shape memory fibers, rubber bands and braiding configuration, which also affect its performance. According to the analysis above, the relationship between the manipulator properties and design parameters is summarized, as shown in Figure 5-1, where strong links are presented with bold lines whereas weak links with fine ones.

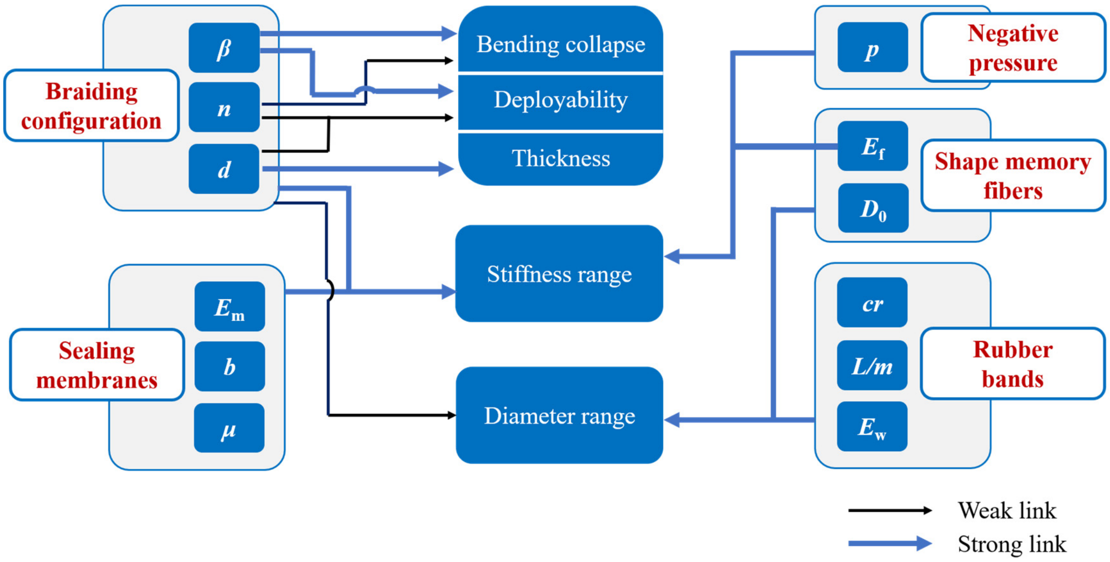

Figure 5-1 Relationship between the application requirements and design parameters of the manipulator.

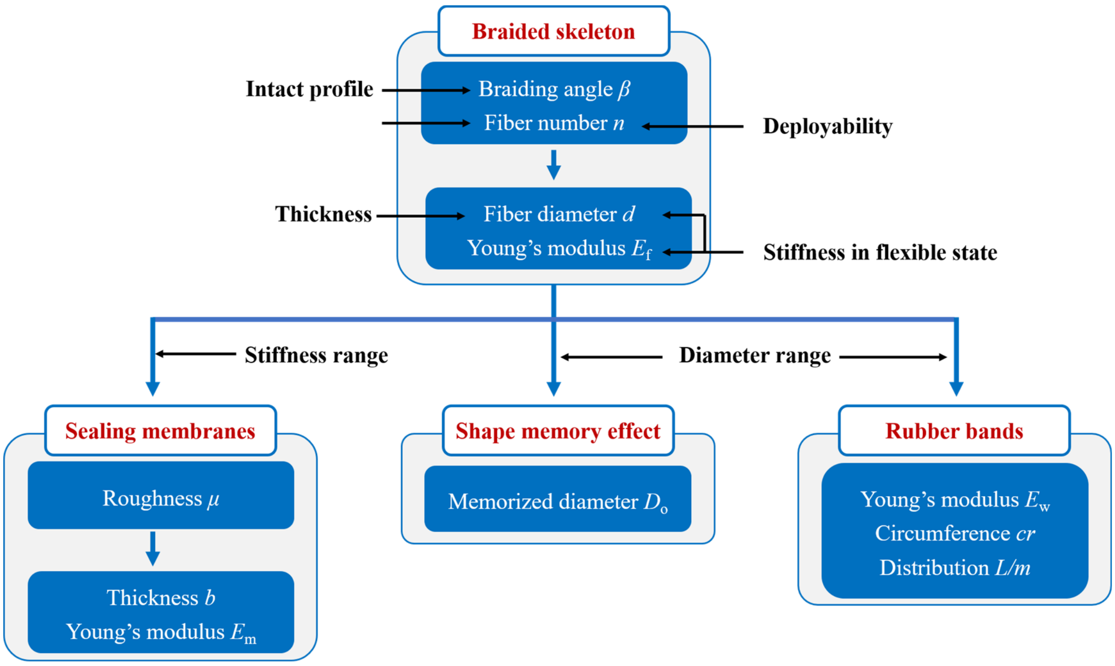

Figure 5-2 Parameter determination process.

With the analysis above, the parameter determination process can be summarized as in Figure 5-2. Firstly, the skeleton parameters are determined according to the geometrical requirements, the fabrication process and the stiffness in the flexible state. With the skeleton parameters, the stiffness range and diameter range can be designed in parallel. With regard to the stiffness range, the roughness of the sealing membranes should be improved, and then membranes with a suitable stiffness can be determined according to the friction. On the other hand, shape memory effect and rubber bands should be considered simultaneously to widen the diameter range. Based on the process in Figure 5-2, parameters of the skeleton are selected and listed in Table 5-1.

Table 5-1 Parameters of the manipulator prototype

Component	Parameter	Value
Overall configuration	Manipulator length when folded	340mm
	Manipulator memorized diameter	26mm
NiTi fiber	Fiber number	12×2
	Fiber diameter	0.5mm
	Young's modulus at I=2A	41.56Gpa
	Young's modulus at I=0A	7.76Gpa
PTFE sealing membranes	Thickness	0.05mm
	Young's modulus	460Mpa
	Friction coefficient	0.3
PTFE tubular coat	Inner diameter	1.2mm
	Outer diameter	1.6mm
	Young's modulus	1.14Gpa
Rubber bands	Rubber band length	32mm
	Rubber band elasticity	0.77
	Number of the rubber bands	4
	Density of the rubber band distribution	36.2mm
Others	Braiding angle	47.8^{o}
	Negative pressure	93Kpa

5.2.2 Prototype Assembly

Figure 5-3 presents the manipulator prototype together with its control system. The whole system is composed of five parts: the manipulator, a tortuous orifice, a cable driving system, a heat actuation system and a negative pressure system. The manipulator uses the same skeleton pattern introduced in Chapter 4. Differently, the manipulator dresses PTFE membranes as the sealing cover due to its better heat durability. A double-braid configuration is adopted, which can provide a sufficient stiffness but keep the resistance at a lower level, making it easier to be heated at a lower voltage. The manipulator has a memorized diameter of 26mm and a length of 340mm when folded. The tortuous orifice is fabricated by 3D printing, which has an inner diameter of 26mm and two distinct curves along its centerline to imitate the curvatures at the throat and the end of esophageal. The cable driving system is composed of three cables, which are set evenly along the circumference of the manipulator and tied to the distal end. With stressing and relaxing of the cables, the end of the manipulator can be adjusted to a suitable posture. The cables are driven by three stepper motors in the driving box. The motors are actuated by three drivers and a controller, set in the control box. The deployment of the manipulator is controlled by the heat actuation system with a constant-current power supply as its main part. The negative pressure system is composed of an air pump and a barometer. The maximum of the pressure is around 93kPa.

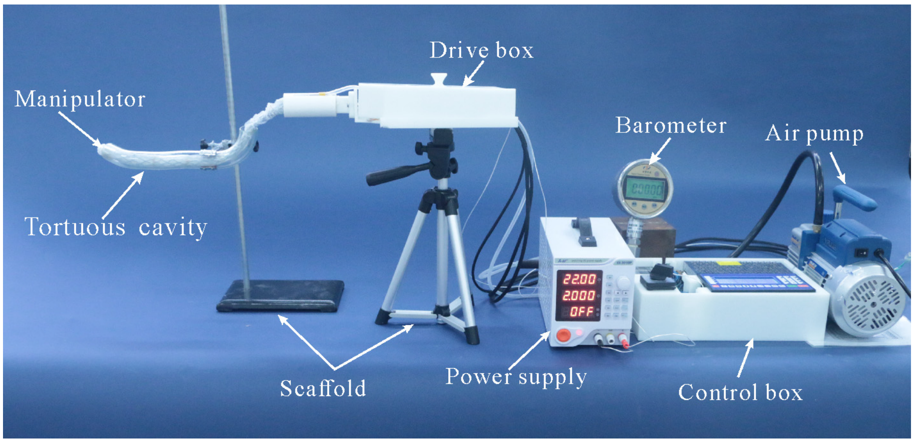

Figure 5-3 The manipulator prototype and its control system.

5.2.3 Workflow

Based on the analysis before, the proposed deployable manipulator tunes its stiffness through negative pressure and changes its diameter at electrical heating. Its skeleton is made of shape memory fibers, which is covered by sealing membranes. In application, it also has to combine the two mechanisms together to make it functional.

A control strategy of the integrated deployable manipulator has been proposed as shown in Figure 5-4. In the normal state, both negative pressure and heating are off, and thus the manipulator demonstrates a flexible state and presents a small diameter. In this state, the manipulator can be easily inserted into the body cavity via the body orifice because of its ideal stiffness and size. When arriving at the lesion, the manipulator starts to be heated and deploy, taking on an increasing diameter. When the outline of the profile reaches the maximum, the negative pressure should be turned on and the heat can be cancelled. The manipulator turns to be rigid by the negative pressure. In fact, the negative pressure method restricts the deformation of the fibers at any configuration of the manipulator. As a result, it helps not only in stiffening function but also in shape-locking. Even though the skeleton tends to be slim when the heat is off, profile of the manipulator can still be maintained by the negative pressure. The manipulator can stay in the larger-diameter, rigid state without current. In this way, the manipulator need not be charged during surgical operation. Finally, after the surgical operation, the negative pressure is switched off. The membranes lose their locking capability to the skeleton, and the manipulator returns to normal state immediately, making it easy to be withdrawn.

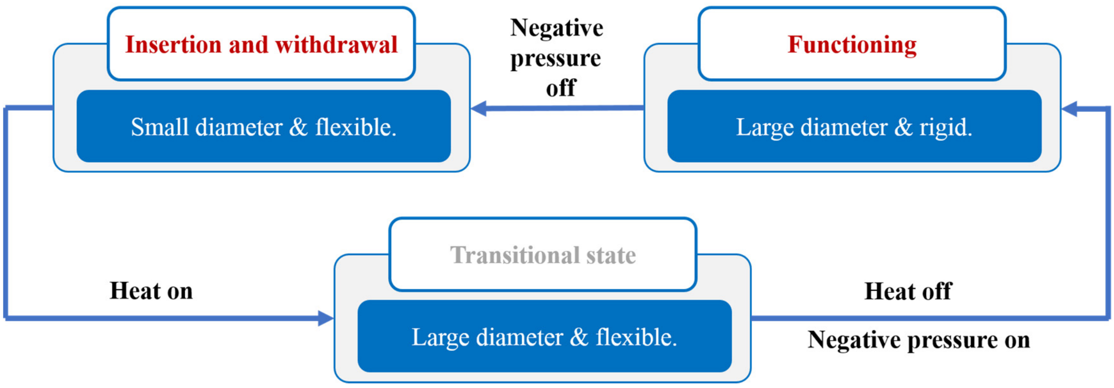

Figure 5-4 Control strategy of the manipulator with coupled tunable stiffness and tunable diameter.

5.3 Performance

This part gives the manipulator prototype together with its control system, which is put into demonstration test. The tunable properties are characterized with analytical models. In consideration of the performance in the test, comparison results with the commercial endoscopes, and the problems occurring during fabrication, the problems occurring during fabrication, strengths and limitations of the manipulator are summarized.

5.3.1 Demonstration Test

To validate the feasibility of the manipulator, a demonstration test which imitates the surgical process of a NOTES via mouth is conducted on the developed prototype. The whole process is presented in Figure 5-5. At the beginning, the tortuous orifice is fixed on a scaffold to provide a stable platform, and the posture of the orifice is carefully tuned. One curve of the orifice is in vertical plane and the other is set horizontally. In this way, the posture of the esophageal orifice of a patient lying on bed is resembled. Secondly, the braided manipulator is gradually inserted into the orifice by hand. The longitudinal stiffness of the manipulator is well suitable, and no unwanted deployment occurs during insertion. What is meaningful, thanks to the slim configuration, the manipulator passes through the orifice easily and arrives at the distal end, as shown in Figure 5-5(a). Considering the sealing membrane is not well transparent, in the third step, the negative pressure is applied to compress the membranes onto the skeleton. This is not a necessary procedure in surgery, but it clearly shows the slim contour of the manipulator, as shown in Figure 5-5(b). Fourthly, the negative pressure is cancelled, and the constant-current power supply is turned on. The manipulator skeleton expands to its large-diameter state at the electrical heating. When the manipulator is fully deployed, the power supply is turned off, while the negative pressure is applied again, under which the manipulator comes to the rigid state. After cancelling the electrical heating, the manipulator keeps the large-diameter rigid state for the friction brought by the membranes, as shown in Figure 5-5(c). The large-diameter, rigid state is the working state of the manipulator, during which following flexible instruments can be inserted into the patient body via the manipulator. After a while, the negative pressure is cancelled, and the cooled manipulator returns to the slim, flexible state. In this state, the manipulator does not have close contact with body orifice and can deform passively. As a result, the manipulator can be withdrawn easily by pulling its proximal end which is located outside the body. The withdrawal process is shown in Figure 5-5(d). The demonstration test strictly follows the surgical procedure. It verifies that the manipulator can successfully couple the deployability with the rigid-flexible conversion performance and has practical value.

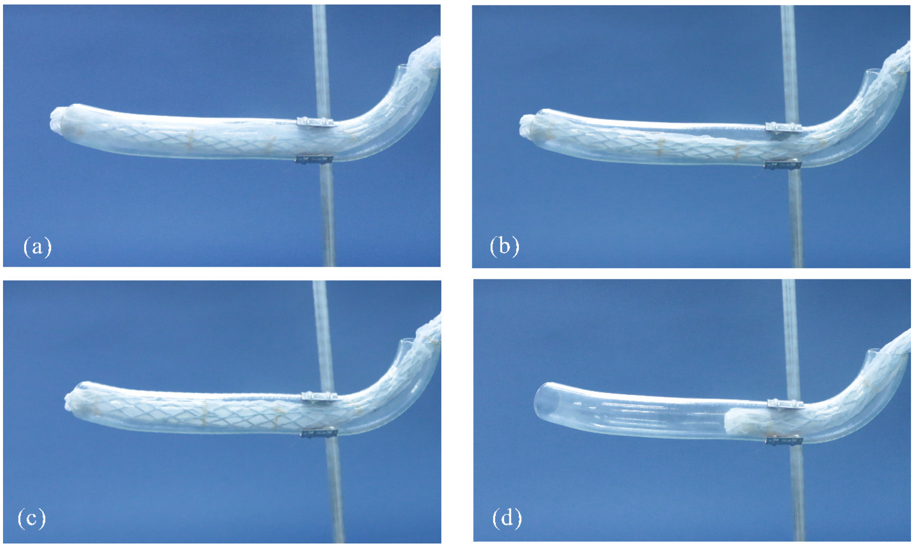

Figure 5-5 The process of the demonstration test: (a) insertion of the manipulator; (b) slim state at negative pressure, (c) large-diameter state at negative pressure and (d) withdrawal of the manipulator.

5.3.2 Tunable properties

1. Stiffness range

Concerning on a constant profile and linear material of the manipulator, the stiffness analysis in Chapter 3 pays attention to the effects of the negative pressure on the tunable stiffness merely. However, in the integrated prototype, it has deployed and tuned its outline before the stiffness transformation. Thus, the tunable diameter and its actuation, i.e., electrical heating, may also have effect on the overall stiffness.

Firstly, the effect of the tunable diameter is analyzed. According to the workflow of the manipulator introduced in Section 5.2.3, the manipulator diameter is not electrically actuated in the flexible state until the manipulator is ready to get into the rigid state. As a result, compared with the state, the manipulator presents a larger diameter in the rigid state. According to material mechanics, a large diameter at the same thickness can improve the bending stiffness of a cantilever beam. In addition, the tuned diameter also affects the braiding configuration of the tube, especially the braiding angle, thus exerting additional effects on the bending stiffness

Secondly, the heat effects increase the temperature of the manipulator, which may affect the material property. The NiTi material is heat sensitive, which changes its phase with temperature, thus varying the stiffness of the braiding fiber. When heated, the material changes to the austenite phase, presenting a higher stiffness. In contrast, the PTFE material used to fabricate the sealing membrane and the fiber coat is distinct for its good heat durability [117], and effect of the electrical heating on it can be ignored.

Based on these, the stiffness determination process should follow the surgical process and is reorganized as follows. First, the bending moment in the flexible state is calculated based on Eq. (3-2) with the skeleton parameters in the slim configuration. Next, according to Eqs. (1-2) and (1-3), geometrical configuration of the deployed manipulator skeleton can be determined. Using the new geometrical configuration and Eqs. (3-10) and (3-11), stiffness of the manipulator in the rigid state can be obtained. The stiffness determination process is presented as Figure 5-6.

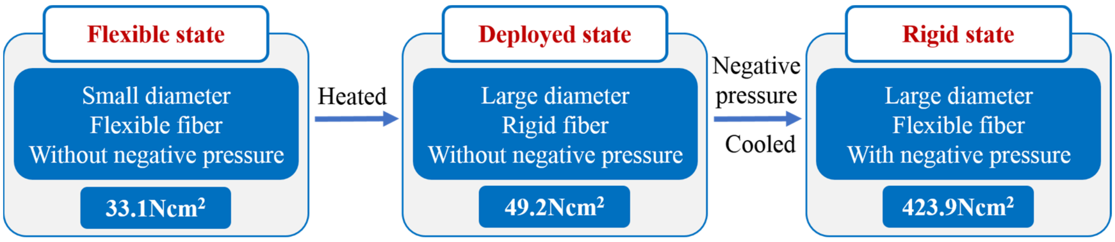

Figure 5-6 The stiffness determination process of the manipulator.

Regarding to the stiffness, the overall size, thickness and testing method vary greatly among different manipulator designs, making it hard to make a direct comparison of the stiffness among them. Therefore, this dissertation focuses on the endoscopes with a similar operation procedure, and their readily available bending stiffness data are adopted as benchmarks to evaluate the stiffness of the braided manipulator [65]. Currently, commercial endoscopes generally have a bending stiffness ranging from 160 to 240 Ncm^2 [118]. A manipulator, with a bending stiffness lower than 160 Ncm^2 in the flexible state, and much larger than 240 Ncm^2 in the rigid state, is viewed to satisfy both easy access and adequate support for surgical instruments.

Motivated by this objective, the bending stiffness of the manipulator prototype is calculated. Since there is a nonlinear relationship between moment and bending angle of the manipulator, the bending stiffness is calculated as the tangent stiffness at a bending angle of 30°, i.e.,

$$EI=M_{30}L/(\pi/6) \tag{5-1}$$

As for the previously developed theoretical model, the bending stiffness is 33.1Ncm^2 in the flexible state, only 20.7% of the most flexible commercial endoscope. In the rigid state, it reaches 423.9Ncm^2, which is 76.6% higher than that of the stiffest commercial endoscope. Hereby it is deemed suitable for NOTES.

2. Diameter range

The ideal diameter range of a surgical manipulator is determined based on the applications requirements. According to the Natural Orifice Surgery Consortium for Assessment and Research (NOSCAR) working group, considering the body orifice size, it is ideal for a manipulator to be compact in size and have a diameter of 20mm or less [23]. Table 5-2 compares the diameters of the existing surgical manipulators and platforms in NOTES, which vary in 18-22mm. With the proposed design method, the physical model can realize a diameter range of 14.7-21.4mm. Its diameter ratio is 1.46, which can be easily improved to 1.6 at an optimized rubber band configuration, as shown in Figure 4-6. On the whole, if the braided skeleton exhibits a diameter of 20mm at deployment state, it is likely to be folded to a profile of 20/1.6=12.5mm. It is similar to those of the commercial endoscopes at a range of 12.8-13.3mm [118], making the insertion process smoother.

Table 5-2 Outer diameter of the existing devices

Manipulator/Platform	Outer diameter
Layer Jamming [63]	22mm
Dragon Skin [65]	20mm
DDES [42]	22mm
IOP [119]	18mm

5.3.3 Discussions

The demonstration test has presented the working process of the braided manipulator. Together with the results in diameter and stiffness ranges, the promise of the manipulator has been successfully validated. However, there are still some challenges.

First and most importantly, the manipulator adopts the heat actuation method, leading to problems in response time. According to the test results shown in Figure 4-12, it takes about 20s to deploy the braided skeleton to a large-diameter state. In the test, it is heated from the room temperature. If a careful preheating is applied in advance to increase the temperature to slightly below the transition temperature, the deployment process will be greatly accelerated. In contrast, the response time to fold the manipulator is not significant. As the braided skeleton should get coupled with the tunable stiffness mechanism and form the final manipulator, it can stiffen under negative pressure to lock its large profile. In this regard, the skeleton does not need to be charged during the surgery, leaving enough time to cool down. It can still work properly without an active cooling element and return to slim state when the negative pressure is stopped after the surgical operation. However, if the posture of the manipulator should be tuned frequently during operation, the response time may be a barrier.

Another problem brought by the heat actuation is the high temperature. In this case, the phase change temperature of the NiTi fiber is 55°C, which is higher than the body temperature. The high temperature can cause tissue damage, becoming a threat to the safety of the patient. This is the major barrier of this prototype to an animal test, but it can be released by using a heat-insulated cover. In this prototype, the sealing membranes are only used to create negative pressure and obtain the tunable stiffness, which can be designed concerning both sealing and heat insulation. Also, a temperature feedback part can be included in the heat actuation system to avoid the excessive heat, thus releasing the safety risk.

Moreover, it is not so obvious but according to Eq. (1-3), the manipulator will shorten in length while deploying. This can generate a movement of the distal end thus leading to an inaccurate position. This can be released but never solved through a parametric selection. In this circumstance, a continuous insertion during deployment is needed. This requires a feedback system and good manipulating skills.

Besides, the manipulator does not fully deploy at the curves as shown in Figure 5-5(d). The normal and tangential forces between the manipulator and the orifice may have effects on the bending behavior, making the mechanism more complicated, and the deployment at a bent configuration may be different from that at a straight one. What’s more, the designed braiding angle is given at the memorized configuration of the skeleton. The angle gets larger after the manipulator covered with rubber bands. Therefore, a braiding angle smaller than that determined by the present analytical model should be adopted.

5.4 Conclusion

In this chapter, based on the analytical results from the former chapters, relationships between the design parameters and the manipulator properties have been established. By distinguishing the strong and weak relationships, the effects of the parameters have been decoupled, and thus the parameter determination process has been formed. In this process, a prototype together with its control system has been designed and fabricated. The workflow of the manipulator has been introduced, and the comprehensive integration of the two tunable properties allows it to operate during surgery without being charged. The performance of the manipulator has been characterized through prototype test and calculation. The demonstration test has successfully imitated the whole surgical procedure. The theoretical stiffness range and the experimental diameter range of the prototype are 33.1-423.9Ncm^2 and 14.7-21.4mm, respectively, which also meet the application requirements. All these have proven the feasibility of the manipulator. However, there are still imperfections and challenges facing the manipulator. A smart heat control system, a continuous insertion and a smaller braiding angle should be adopted to the manipulator functioning.

Chapter 6 Achievements and Future Work

The aim of this dissertation is to design a deployable manipulator with tunable stiffness and to characterize its performance. In this chapter, the main achievements and future work are summarized.

6.1 Main Achievements

- **Mechanics of the braided tube**

In the first place, mechanical behaviors of the braided tube have been systematically studied to support its function as the manipulator skeleton. Analysis about the deployment related to the force and geometry indicates that the largest reachable diameter ratio between the maximum diameter and the minimum diameter can be estimated as 1:0.37. Research on the bending collapse behavior reveals the bending deformation mechanism, discovering that the braiding angle and the number of fibers will affect the collapse. It also concludes that a braiding angle smaller than 48.5^{o} can guarantee a basically intact profile. A new braiding pattern named hybrid braiding has been proposed, which adopts different braiding angles in the tube. With the geometrical incompatibility, its longitudinal stiffness has been increased by 57.1%. The work in Chapter 2 helps optimize parameters of the braided skeleton towards the manipulator application.

- **Tunable stiffness mechanism based on negative pressure**

Next, a tunable stiffness mechanism based on negative pressure has been proposed. It takes a braided tube as the skeleton and uses negative pressure to change the friction between the membrane cover and the skeleton thus tuning the stiffness. On the basis of the spring theory, a membrane-fiber interaction model has been established, with which the bending stiffness of the manipulator in both rigid and flexible states can be theoretically calculated. The model has been validated by experiments and simulations. According to the experiments, the bending stiffness ratio between the rigid and flexible states can reach 6.85. Also, the radial stiffness at lateral indentation has been numerically and experimentally analyzed. It finds the strain energy of the skeleton and the friction dissipation contribute to the enhancement of the radial stiffness. The work in Chapter 3 helps understand the stiffness enhancing mechanism and provides guidance in stiffness design.

- **Two-way tunable diameter actuation based on shape memory fibers**

Then, a heat actuated tunable diameter mechanism has been proposed, which uses single-direction memory fibers and rubber bands to achieve a tunable diameter in double directions. The actuation method is validated with experiments. It takes 20s for the manipulator to deploy, which shows a diameter range of 14.7mm to 21.4mm. A theoretical model for the diameter range is also established through analysis of the load relationship between the tube and the bands. Heat response of the actuation method is studied through heat transfer analysis, which reveals that a preheating can shorten the response time to be less than 10s. The work in Chapter 4 enables the manipulator to vary its profile in double directions and provides references for diameter range design and heat response control.

6.2 Future Work

This dissertation contributes to the design and performance characterization of the braided manipulator. The analytical results and the prototype test validate the feasibility of the manipulator design. However, more work is needed to improve it and bring widespread adoption in surgery.

Above all, the heat actuation method for tunable diameter can cause problems in response time and patient safety. The temperature of the manipulator when heated is higher than the body temperature. A smart heat control system is needed to shorten the temperature range, thus speeding up the actuation and avoiding excessive heat. To establish the system, a feedback system with temperature sensor is supposed to be equipped; besides, phase change of the NiTi alloy and dynamic properties of the tube ought to be investigated to establish the links between heat generation and mechanical response. In addition, heat stability and insulation of the sealing membranes shall also be considered to protect the patient. The safety risk can be released by designing the heat control system and the heal-insulated membranes.

In addition, the stiffening capability of the manipulator will be further improved. According to the stiffness analysis in this dissertation, the friction between the membranes and the fibers plays a vital role in the stiffness enhancement. Therefore, the method to improve the roughness of the membranes will be focused. If rougher membranes are designed, the membranes will affect the deformation of the braided skeleton greatly. In this condition, the assumption that the deformation of the skeleton is pure bending under moment may not be correct. An improved theoretical model should be proposed to adapt to the condition of rough membranes.

Moreover, there exist some limitations in mechanical behaviors of the braided skeleton, which can be improved by the proposal of a new design or an improved theoretical model. When deployed, the tube will be shortened in length. Consequently, this will cause inconvenience since the manipulator needs to be continuously inserted into the body in this state. Additionally, the manipulator may suffer from indentation and bending simultaneously at the tortuous orifice, making it easier for the manipulator to collapse. With regard to this, the theoretical models need to be improved to explain the mechanical behaviors in a more complicated situation and new design is also needed to solve the problems.

What's more, the interaction between the prototype and the nature body will be looked into. The human esophagus is not a perfect tubular orifice, and the deployment of the manipulator under the compression of the esophageal tissue will be studied. In fact, the esophageal provides a support to the manipulator and improves the stability of the surgical instrument. The collective effect of the orifice and the manipulator on the performance of the surgical instrument will be analyzed.

Finally, an in vitro or animal experiment will be conducted to further validate the efficacy of the manipulator. Results with and without the manipulator will be compared and investigated. The interactions between the manipulator and the surgical instrument will be investigated.

References

[1] Moris D N, Bramis K J, Mantonakis E I, et al. Surgery via natural orifices in human beings: yesterday, today, tomorrow [J]. American Journal of Surgery, 2012, 204(1): 93-102.

[2] Richards W O, Rattner D W. Endoluminal and transluminal surgery: no longer if, but when [J]. Surgical Endoscopy and Other Interventional Techniques, 2005, 19(4): 461-463.

[3] Magrina J F, Kho R M, Weaver A L, et al. Robotic radical hysterectomy: Comparison with laparoscopy and laparotomy [J]. Gynecologic Oncology, 2008, 109(1): 86-91.

[4] Bouvy N D, Marquet R L, Jeekel H, et al. Impact of gas(less) laparoscopy and laparotomy on peritoneal tumor growth and abdominal wall metastases [J]. Annals of Surgery, 1996, 224(6): 694-700.

[5] Tracy C R, Raman J D, Cadeddu J A, et al. Laparoendoscopic single-site surgery in urology: where have we been and where are we heading? [J]. Nature Reviews Urology, 2008, 5(10): 561-568.

[6] Rangarajan M. Multiple port-site and subcutaneous metastases following palliative laparoscopic surgery for advanced gastric cancer [J]. Annals of the Academy of Medicine Singapore, 2007, 36(10): 875-876.

[7] Mcgee M F, Rosen M J, Marks J, et al. A primer on natural orifice transluminal endoscopic surgery: building a new paradigm [J]. Surgical Innovation, 2006, 13(2): 86-93.

[8] Zuo S, Wang S. Current and emerging robotic assisted intervention for NOTES [J]. Expert Review of Medical Devices, 2016, 13(12): 1095-1105.

[9] Strong A T, Rodriguez J, Kroh M, et al. Intramural surgery: a new vista in minimally invasive therapy [J]. Journal of the American College of Surgeons, 2017, 225(2): 339-342.

[10] Alhamyani SSA and Abdelrahman TM. Natural orifice transluminal endoscopic surgery: uses, advantages, complications and cost [J]. Journal of Research in Medical and Dental Science, 2020 8(4): 99-106.

[11] Fritscher-Ravens A, Patel K, Ghanbari A, et al. Natural orifice transluminal endoscopic surgery (NOTES) in the mediastinum: long-term survival animal experiments in transesophageal access, including minor surgical procedures [J]. Endoscopy, 2007, 39(10): 870-875.

[12] Bazzi W M, Wagner O, Stroup S P, et al. Transrectal hybrid natural orifice transluminal endoscopic surgery (NOTES) nephrectomy in a porcine model [J]. Urology, 2011, 77(3): 518-523.

[13] Sylla P, Willingham F F, Sohn D K, et al. NOTES rectosigmoid resection using transanal endoscopic microsurgery (TEM) with transgastric endoscopic assistance: a pilot study in swine [J]. Journal of Gastrointestinal Surgery, 2008, 12(10): 1717-1723.

[14] Zorron R, Filgueiras M, Maggioni L C, et al. NOTES. Transvaginal cholecystectomy: report of the first case [J]. Surgical Innovation, 2007, 14(4): 279-283.

[15] Cen K, Zhang B, Li H. Progress on natural orifice transluminal endoscopic surgery [J]. Basic & Clinical Medicine, 2019,39(05): 745-749. (in Chinese)

[16] Leung A L H, Cheung H Y S, Li M K W. Advances in laparoscopic colorectal surgery: a review on NOTES and transanal extraction of specimen [J]. Asian Journal of Endoscopic Surgery, 2014, 7(1): 11-16.

[17] Abbott D J, Becke C, Rothstein R I, et al. Design of an endoluminal notes robotic system [C]. In Intelligent Robots and Systems, IROS 2007, IEEE/RSJ International Conference, 2007, 410-416.

[18] Rattner D, Kalloo A. ASGE/SAGES working group on natural orifice translumenal endoscopic surgery [J]. Surgical Endoscopy and Other Interventional Techniques, 2006, 20(2): 329-333.

[19] Zhang Y, Lu M. A review of recent advancements in soft and flexible robots for medical applications [J]. International Journal of Medical Robotics and Computer Assisted Surgery, 2020, 16(3): e2096.

[20] Blanc L, Delchambre A, Lambert P. Flexible medical devices: review of controllable stiffness solutions [J]. Actuators, 2017, 6(3): 23.

[21] Bingener J and Gostout C J. Update on natural orifice translumenal endoscopic surgery [J]. Gastroenterology & Hepatology, 2012, 8(6): 384-389.

[22] Zhang G, Ren X, Li J, et al. Modified pre-stretching assembly method for cable-driven systems [J]. Chinese Journal of Mechanical Engineering, 2019, 32(1): 48.

[23] National Orifice Surgery Consortium for Assessment and Research (NOSCARTM). Working group summary on development of a multitasking platform [OL]. 2006.

http://www.noscar.org/presentations-2006/tasking-platform.

[24] Catherine J, Rotinat-Libersa C, Micaelli A. Comparative review of endoscopic devices articulations technologies developed for minimally invasive medical procedures [J]. Applied Bionics and Biomechanics, 2011, 8(2), 151-171.

[25] Rosenberg N. Submucosal saline wheal as safety factor in fulguration or rectal and sigmoidal polypi [J]. Archives of Surgery, 1955, 70(1):120-122.

[26] Waye JD, Rex D, Williams CB. Colonoscopy Principles and Practice: Malden [M]. Massachusetts: Blackwell Publishing, 2003: 420-442.

[27] Yip H and Chiu P. Recent advances in natural orifice transluminal endoscopic surgery [J]. European Journal of Cardio-thoracic Surgery, 2016, 49: 25-30.

[28] Kalloo A N, Kantsevoy S V, Singh V K, et al. Flexible transgastric peritoneoscopy: a novel approach to diagnostic and therapeutic interventions in the peritoneal cavity [J]. Gastroenterology, 2000, 118(4): A1039.

[29] Gettman M T, Lotan Y, Napper C A, et al. Transvaginal laparoscopic nephrectomy: development and feasibility in the porcine model [J]. Urology, 2002, 59(3): 446-450.

[30] Rao GV, Reddy N. Transgastric appendectomy in humans [C]. Society of American Gastrointestinal and Endoscopic Surgeons (SAGES), Dallas, 2006.

[31] National Orifice Surgery Consortium for Assessment and Research (NOSCARTM). About NOSCAR [OL]. 2005.

https://www.noscar.org/about-noscar/.

[32] Zhu J, Hu H, Ma Y, et al. Transumbilical endoscopic surgery: a preliminary clinical report [J]. Surgical Eendoscopy and Other Interventional Techniques, 2009, 23(4): 813-817.

[33] Hu S, Zhang Y, Li F. Successful implementation of China's first clinical NOTES operation [J]. Journal of Laparoscopic Surgery, 2009, 14(4): 320. (in Chinese)

[34] Wang X. Techniques of natural orifice specimen extraction surgery for colorectal cancer [J]. Chinese Journal of Operative Procedures of General Surgery (Electronic Edition), 2016, 10(2): 94-96. (in Chinese)

[35] Li Q, Wu Q, Zhang X, et al. Outcomes of per-oral endoscopic myotomy for treatment of esophageal achalasia with a median follow-up of 49 months [J]. Gastrointestinal Endoscopy, 2017, 87(6): 1405.

[36] Wang S. Creation and manufacturing of accurate minimally invasive surgical instrument [J]. Chinese Journal of Mechanical Engineering, 2018, 54(17): 1. (in Chinese)

[37] Zhang G. Design Method and Experimental Study of the Stiffness-controllable Instrument for Natural Orifice Transluminal Endoscopic Surgery [D]. Tianjin: Tianjin University, doctoral dissertation, 2018. (in Chinese)

[38] Li S, Wu H, Lv C et al. Feasibility and safety of gallbladder exploration by transgastric natural orifice transluminal endoscopic surgery [J]. Journal of Regional Anatomy and Operative Surgery, 2020, 29(4), 257-261. (in Chinese)

[39] Rattner D W, Hawes R, Schwaitzberg S, et al. The Second SAGES/ASGE White Paper on natural orifice transluminal endoscopic surgery: 5 years of progress [J]. Surgical Endoscopy and Other Interventional Techniques, 2011, 25(8): 2441-2448.

[40] Fuchs KH and Breithaupt W. Transgastric small bowel resection with the new multitasking platform EndoSAMURAITM for natural orifice transluminal endoscopic surgery [J]. Surgical Endoscopy, 2012, 26(8): 2281-2287.

[41] Yeung BPM and Gourlay T. A technical review of flexible endoscopic multitasking platforms [J]. International Journal of Surgery, 2012, 10(7): 345-354.

[42] Thompson CC, Ryou M, Soper NJ, et al. Evaluation of a manually driven, multitasking platform for complex endoluminal and natural orifice transluminal endoscopic surgery applications (with video) [J]. Gastrointestinal Endoscopy, 2009, 70(1): 121-125.

[43] Rex, D K, Khashab, M, Raju G S, et al. Insertability and safety of a shape-locking device for colonoscopy [J]. The American Journal of Gastroenterology, 2005, 100(4): 817-820.

[44] He G, Fan Y, Su T, et al. Variable impedance control of cable actuated continuum manipulators [J]. International Journal of Control, Automation and Systems, 2020, 18(7): 1039-1052.

[45] Kim YJ, Cheng S, Kim S, et al. A stiffness-adjustable hyperredundant manipulator using a variable neutral-line mechanism for minimally invasive surgery [J]. IEEE Transactions on Robotics, 2013, 30(2): 382-395.

[46] Tamadon I, Huan Y, Groot AGD, et al. Positioning and stiffening of an articulated/continuum manipulator for implant delivery in minimally invasive surgery [J]. The International Journal of Medical Robotics and Computer Assisted Surgery, 2020, 16(2): 10.1002/rcs.2072.

[47] Zhao R, Yao Y, Luo Y. Development of a variable stiffness over tube based on low-melting-point-alloy for endoscopic surgery [J]. Journal of Medical Devices, 2016, 10(2): 303-310

[48] Chautems C, Tonazzini A, Floreano D, et al. A variable stiffness catheter controlled with an external magnetic field [C]. IEEE/RSJ International Conference on Intelligent Robots and Systems (IROS), Vancouver: IEEE, 2017: 181-186.

[49] Cao Y, Ju F, Zhang L, et al. A novel variable-stiffness flexible manipulator actuated by shape memory alloy for minimally invasive surgery [J]. Proceedings of the Institution of Mechanical Engineers, Part H: Journal of Engineering in Medicine, 2018, 232(11): 1098-1110.

[50] Jiang S, Chen B, Qi F, et al. A variable-stiffness continuum manipulators by an SMA-based sheath in minimally invasive surgery [J]. The International Journal of Medical Robotics and Computer Assisted Surgery, 2020, 16(2): e2081.

[51] Loeve A J, Bosma J H, Breedveld P, et al. Polymer rigidity control for endoscopic shaft-guide 'Plastolock'-a feasibility study [J]. Journal of Medical Devices, 2010, 4(4): 045001.

[52] Zhang G, Ma J, Shang Z, et al. Deployable manipulator with tunable stiffness for natural orifice transluminal endoscopic surgery [J]. Chinese Journal of Mechanical Engineering, 2018, 54(17): 28-35. (in Chinese)

[53] Le HM, Phan PT, Lin C, et al. A temperature-dependent, variable-stiffness endoscopic robotic manipulator with active heating and cooling [J]. Annals of Biomedical Engineering, 2020, 48(6): 1837-1849.

[54] Le HM, Cao L, Do TN, et al. Design and modelling of a variable stiffness manipulator for surgical robots [J]. Mechatronics, 2018, 53: 109-123.

[55] Rao A, Srinivasa AR, Reddy JN, Design of shape memory alloy (SMA) actuators [M]. Berlin: Springer International Publishing, 2015, ch. 1.

[56] Amend J R, Brown E, Rodenberg N, et al. A positive pressure universal gripper based on the jamming of granular material [J]. IEEE Transactions on Robotics, 2012, 28(2): 341-350.

[57] Wei Y, Chen Y, Ren T, et al. A novel variable stiffness robotic gripper based on integrated soft actuating and particle jamming [J]. Soft Robotics, 2016, 3(3): 134-143.

[58] Jiang P, Yang Y, Chen M, et al. A variable stiffness gripper based on differential drive particle jamming [J]. Bioinspiration & Biomimetics, 2019, 14(3): 036009.

[59] De Falco I, Cianchetti M, Menciassi A. A soft multi-module manipulator with variable stiffness for minimally invasive surgery [J]. Bioinspiration & Biomimetics, 2017, 12(5): 056008.

[60] Cianchetti M, Ranzani T, Gerboni G, et al. STIFF-FLOP surgical manipulator: mechanical design and experimental characterization of the single module [C]. IEEE/RSJ international conference on intelligent robots and systems. Tokyo: IEEE, 2013: 3576-3581.

[61] Yagi A, Matsumiya K, Masamune K, et al. Rigid-flexible outer sheath model using slider linkage locking mechanism and air pressure for endoscopic surgery [C]. International Conference on Medical Image Computing and Computer-Assisted Intervention, Copenhagen: MICCAI, 2006, 503-510.

[62] Loeve A J, Plettenburg D H, Breedveld P, et al. Endoscope shaft-rigidity control mechanism: "FORGUIDE" [J]. IEEE Transactions on Biomedical Engineering, 2012, 59(2): 542-551.

[63] Kim YJ, Cheng S, Kim S, et al. A novel layer jamming mechanism with tunable stiffness capability for minimally invasive surgery [J]. IEEE Transactions on Robotics, 2013, 29(4): 1031-1042.

[64] Li DCF, Wang Z, Ouyang B, et al. A Reconfigurable Variable Stiffness Manipulator by a Sliding Layer Mechanism [C]. International Conference on Robotics and Automation (ICRA), Montreal: IEEE, 2019: 3976-3982.

[65] Zuo S, Iijima K, Tokumiya T, et al. Variable stiffness outer sheath with "dragon skin" structure and negative pneumatic shape-locking mechanism [J]. International Journal of Computer Assisted Radiology and Surgery, 2014, 9(5): 857-865.

[66] Kim J, Choi W Y, Kang S, et al. Continuously variable stiffness mechanism using nonuniform patterns on coaxial tubes for continuum microsurgical robot [J]. IEEE Transactions on Robotics, 2019, 35(6): 1475-1487.

[67] Ren X, Zhang G, Shang Z, et al. A variable stiffness spring-sponge composite tube with fast response and shape recovery [J]. Macromolecular Materials and Engineering, 2018, 303(10): 1800185.

[68] Pellegrino S. Deployable structures [M]. Vienna: Springer, 2001.

[69] De BM, Van CS, Mortier P, et al. Virtual optimization of self-expandable braided wire stents [J]. Medical Engineering & Physics, 2009, 31(4): 448-453.

[70] Hu J. 3-D fibrous assemblies: properties, applications and modelling of three-dimensional textile structures [M]. Boca Raton: CRC Press, 2008.

[71] Harte AM, Fleck NA, Ashby MF. Energy absorption of foam-filled circular tubes with braided composite walls [J]. European Journal of Mechanics A-Solids, 2020, 19(1): 31-50.

[72] Rial D, Tiar A, Hocine K, et al., Metallic braided structures: the mechanical modeling [J]. Advanced Engineering Materials, 2015, 17(6): 893-904.

[73] Seok S, Onal CD, Cho KJ, et al. Meshworm: a peristaltic soft robot with antagonistic nickel titanium coil actuators [J]. IEEE-ASME Transactions on Mechatronics, 2013, 18(5): 1485-1497.

[74] Boxerbaum AS, Shaw KM, Chiel HJ, et al. Continuous wave peristaltic motion in a robot [J]. International Journal of Robotics Research, 2012, 31(3): 302-318.

[75] Heller L, Vokoun D, Ittner P, et al., 3D flexible NiTi-braided elastomer composites for smart structure applications [J]. Smart Materials and Structures, 2012, 21(4): 317-321.

[76] Santulli C, Patel SI, Jeronimidis G, et al. Development of smart variable stiffness actuators using polymer hydrogels [J]. Smart Materials and Structures, 2005, 14(2): 434-440.

[77] Yuksekkaya ME, Adanur S. Analysis of polymeric braided tubular structures intended for medical applications [J]. Textile Research Journal, 2009, 79(2): 99-109.

[78] Maetani I, Shigoka H, Omuta S, et al. What is the preferred shape for an esophageal stent flange? [J]. Digestive Endoscopy, 2012, 24(6): 401-406.

[79] Jedwab MR, Clerc CO. A study of the geometrical and mechanical properties of a self-expanding metallic stent-theory and experiment [J]. Journal of Applied Biomaterials, 1993, 4(1): 77-85.

[80] Wahl AM. Mechanical Spring [M]. New York: McGraw-Hill, 1963.

[81] Singh C, Wong CS, Wang X. Medical textiles as vascular implants and their success to mimic natural arteries [J]. Journal of Functional Biomaterials, 2015, 6(3): 500-525.

[82] Ma D, Dargush GF, Natarajan SK, et al. Computer modeling of deployment and mechanical expansion of neurovascular flow diverter in patient-specific intracranial aneurysms [J]. Journal of Biomechanics, 2012, 45(13): 2256-2263.

[83] Jamshidi M, Rajabian M, Avery MB, et al. A novel self-expanding primarily bioabsorbable braided flow-diverting stent for aneurysms: initial safety results [J]. Journal of Neurointerventional Surgery, 2020, 12(7): 700-705.

[84] Zamiri P, Kuang Y, Sharma U, et al. The biocompatibility of rapidly degrading polymeric stents in porcine carotid arteries [J]. Biomaterials, 2010, 31(31): 7847-7855.

[85] Chen S, Lotan C, Jaffe R, et al. Pericardial covered stent for coronary perforations [J]. Catheterization and Cardiovascular Interventions, 2015, 86(3): 400-404.

[86] Nuutinen J P, Clerc C, Tormala P. Theoretical and experimental evaluation of the radial force of self-expanding braided bioabsorbable stents [J]. Journal of Biomaterials Science Polymer Edition, 2003, 14(7): 677-687.

[87] Wang R and Ravichandar K. Mechanical response of a metallic aortic stent-part I: pressure-diameter relationship [J]. Journal of Applied Mechanics, 2004, 71(5): 697-705.

[88] Ma D, Dargush GF, Natarajan SK, et al. Computer modeling of deployment and mechanical expansion of neurovascular flow diverter in patient-specific intracranial aneurysms [J]. Journal of Biomechanics, 2012, 45(13): 2256-2263.

[89] Ma D, Dumont TM, Kosukegawa H, et al. High fidelity virtual stenting (HiFiVS) for intracranial aneurysm flow diversion: in vitro and in silico [J]. Annals of Biomedical Engineering, 2013, 41(10): 2143-2156.

[90] Bouillot P, Brina O, Ouared R, et al. Geometrical deployment for braided stent [J]. Medical Image Analysis, 2016, 30: 85-94.

[91] Kim JH, Kang TJ, Yu WR. Mechanical modeling of self-expandable stent fabricated using braiding technology [J]. Journal of Biomechanics, 2008, 41(15): 3202-3212.

[92] Fu W, Cheng G, Yan R, et al. Numerical investigations of the flexibility of intravascular braided stent [J]. Journal of Mechanics in Medicine and Biology, 2017, 17(2):1750075.

[93] Xue W, Gao J, Lin J, et al. Deformation mechanisms of prototype composite braided stent-grafts in bending fatigue for peripheral artery application [J]. Journal of the Mechanical Behavior of Biomedical Materials, 2018, 78: 74-81.

[94] Garbey M, Salmon R, Fikfak V, et al. Esophageal stent migration: Testing few hypothesis with a simplified mathematical model [J]. Computers in Biology and Medicine, 2016, 79: 259-265.

[95] Ni X, Zhang Y, Zhao H, et al. Numerical research on the biomechanical behaviour of braided stents with different end shapes and stent-oesophagus interaction [J]. International Journal for Numerical Methods in Biomedical Engineering, 2018, 34(6): e2971.

[96] Boxerbaum AS, Horchler AD, Shaw KM, et al. Worms, waves and robots[C]. IEEE International Conference on Robotics & Automation, Minnesota: IEEE, 2012: 3537-3538.

[97] Boxerbaum AS, Chiel HJ, Quinn RD. A new theory and methods for creating peristaltic motion in a robotic platform[C]. IEEE International Conference on Robotics & Automation, Anchorage: IEEE, 2010: 1221-1227.

[98] Shanahan C, Tiernan P, Tofail SAM. Looped ends versus open ends braided stent: A comparison of the mechanical behaviour using analytical and numerical methods [J]. Journal of the Mechanical Behavior of Biomedical Materials, 2017, 75:581-591.

[99] Suk KT, Kim JW, Kim HS, et al. Human application of a metallic stent covered with a paclitaxel-incorporated membrane for malignant biliary obstruction: multicenter pilot study [J]. Gastrointestinal Endoscopy, 2007, 66(4): 798-803.

[100] Uitdehaag MJ, Siersema PD, Spaander MCW, et al. A new fully covered stent with antimigration properties for the palliation of malignant dysphagia: a prospective cohort study [J]. Gastrointestinal Endoscopy, 2010, 71(3): 600-605.

[101] Moon T, Hong D, Chun H J, et al. Analytical models for predicting mechanical properties of mesh-type self-expandable metal stents with cover membrane [J]. Current Applied Physics, 2009, 9(1): 92-100.

[102] Sharma U, Concagh D, Core L, et al. The development of bioresorbable composite polymeric implants with high mechanical strength [J]. Nature Materials, 2018, 17(1): 96.

[103] Alherz AI, Tanweer O, Flamini V. A numerical framework for the mechanical analysis of dual-layer stents in intracranial aneurysm treatment [J]. Journal of Biomechanics, 2016, 49(12): 2420-2427.

[104] Ni X, Pan C, Prusty BG. Numerical investigations of the mechanical properties of a braided non-vascular stent design using finite element method [J]. Computer Methods in Biomechanics and Biomedical Engineering, 2015, 18(10): 1117-1125.

[105] Hawes RH, Rattner DW, Fleischer D, et al. NOTES: where have we been and where are we going? [J]. Surgical Endoscopy, 2008, 67(6): 779-780.

[106] Esophagus [OL]. Wikipedia.
https://en.wikipedia.org/wiki/Esophagus.

[107] Abaqus Analysisi Users Manaul, Abaqus documentation version 6.14-1, dassault systems SIMULA Corp. Providence, RI, USA, 2014.

[108] Alpyildiz T. 3D geometrical modelling of tubular braids [J]. Textile Research Journal, 2012, 82(5):443-453.

[109] Zheng Q. Finite element analysis of the mechanical behavior of braided stent for the treatment of intracranial aneurysms [D]. Taiyuan: Taiyuan University of Technology, Master Thesis, 2015. (in Chinese)

[110] Shi Y and Zhou Y. ABAQUS finite element analysis: example and detailed explanation [M]. Beijing: China Machine Press, 2006. (in Chinese)

[111] The elastic modulus, Poisson's ratio and density of commonly used materials [OL]. (in Chinese)
https://wenku.baidu.com/view/26786a04e87101f69e319544.html

[112] Simons JW and Shockey DA. Mechanical testing devices for characterizing stents [C]. International Conference on Shape Memory and Superelastic Technologies, Pacific Grove: Asilomar Conference Center, 2006: 721-730.

[113] Zhang Y. Spring [M]. Beijing: China Machine, 1982. (in Chinese)

[114] Yang S. Fundamentals of heat transfer 2nd [M]. Beijing: Higher Education Press, 2003. (in Chinese)

[115] Nitinol [OL]. Baidu Baike. (in Chinese)
https://baike.baidu.com/item/%E9%95%8D%E9%92%9B%E8%AF%BA/10209744?fr=aladdin

[116] Zheng Y and Zhao L. Biomedical nickel-titanium alloys [M]. Beijing: Science Press, 2004. (in Chinese)

[117] Fluoroplastic [OL]. (in Chinese)
https://wenku.baidu.com/view/d9e2cb160b4e767f5acfceb5.html

[118] Hellier D, Albermani F, Evans B, et al. Flexural and torsional rigidity of colonoscopes at room and body temperatures [J]. Proceedings of the Institution of Mechanical Engineers Part H - Journal of Engineering in Medicine, 2011, 225(4): 389-399.

[119] Swanstrom LL, Whiteford M, Khajanchee Y. Developing essential tools to enable transgastric surgery [J]. Surgical Endoscopy, 2008, 22(3): 600-604.

Appendix

A. *MATLAB* code to calculate the bending stiffness of the manipulator in the rigid state

main.m

```
clear
H=127.26;D=21.46;d=1.07;r=(D-2*d)/2;num=12;p=84.86;
a=atan(p/pi/2/r);a2=pi/2-a;
b=0.04;E=300;P=0.067;u=0.3;
n1=H/2/p*num;e001=P*pi/2*d/cos(a)*u/E/b;
emax1=e001*n1;e01=0.001;s1=H/2;
n2=num/4;e002=P*pi/2*d/cos(a2)*u/E/b;
emax2=e002*n2;e02=0.001;s2=pi*r/2;
do=0.001;o=0:0.001:pi/3;R=H./o;oo=0:0.1:pi;
s=size(R);n=s(1,2);
s=size(oo);nn=s(1,2);
for i=2:1:n
    e=r*sin(oo)/R(i);
    [dE(i),DE(i)]=strain(E,e001,e,e01,emax1,s1);
    ds=pi*r/nn;
    Energy1(i)=dE(i)*ds*b;
    EN1(i)=DE(i)*ds*b;
end
for i=2:1:n
   e1=r*sin(oo)/R(i);
   e2=e1*tan(a);
   [dE(i),DE(i)]=strain(E,e002,e2,e02,emax2,s2);
    ds=H/nn;
    Energy2(i)=dE(i)*ds*b;
    EN2(i)=DE(i)*ds*b;
end
Energy=4*(Energy1+Energy2);
EN=4*(EN1+EN2);
M1(1)=0;
for i=1:1:n-1;
  M1(i+1)=(Energy(i+1)-Energy(i)-M1(i)*do)/do;
end
M1=M1*2;
```

```
E=3498.6;In=pi*d^4/64;Ib=In;Ip=2*In;G=E/2.56;n=H/p;
D=2*r;oo=o;
M=oo.*(1./num/E/In*(1+In/Ib*(sin(a))^2+E*In/G/Ip*(cos(a))^2)*pi*n*D/2/cos(a)).^(-1);
M1=M+M1;oo=oo/pi*180;
plot(oo,M1,'r-')
hold on
plot(oo,M,'r-')
```

strain.m

```
function [dE,DE] = strain(E,e00,e,emin,emax,H)
s=size(e);n=s(1,2);h=0:1:H;
e0=(emax-emin)*h/H;
  for i=1:1:n;
      if (e(i)<emin)
          de(i)=0.5*E*e(i)^2*H;
          De(i)=de(i);
      else if (e(i)>emax)
        fun=@(x)0.5*E*x.^2+E*x.*(e(i)-x);
        fun2=@(x)0.5*E*x.^2;
          de(i)=quad(fun,emin,emax)*H/(emax-emin);
          De(i)=quad(fun2,emin,emax)*H/(emax-emin);
          else
          h0=(e(i)-emin)/(emax-emin)*H;
          fun=@(x)0.5*E*x.^2+E*x.*(e(i)-x);
          fun2=@(x)0.5*E*x.^2;
          de1(i)=quad(fun,emin,e(i))*h0/(e(i)-emin);
          De1(i)=quad(fun2,emin,e(i))*h0/(e(i)-emin);
          de2(i)=0.5*E*e(i)^2*(H-h0);
          De2(i)=de2(i);
          de(i)=de1(i)+de2(i);
          De(i)=De1(i)+De2(i);
          end
      end
  end
    dE=sum(de);
    DE=sum(De);
end
```

B. *MATLAB* code to calculate the diameter range

main.m

```
clear
n=24;d=0.5;d0=1.6;L0=144.8;
D0=26;Dm=D0-2*d0;
phi0=47.8;p0=pi*Dm*tan(phi0/180*pi);
E=41556;G=E/2.7;
I=pi*d^4/64;jd=1000;
%%%%%%%%
D=Dm-14:14/jd:Dm;
phi=acos(cos(phi0/180*pi)*D/Dm)/pi*180;
p=tan(phi/180*pi)*pi.*D;
L=p/p0*L0;
K1=sin(2*phi0/180*pi)/Dm; K2=2*(cos(phi0/180*pi))^2/Dm; K3=Dm/cos(phi0/180*pi);
F=2*n*(G*2*I*cos(phi/180*pi)/K3.*(2*sin(phi/180*pi)/K3-K1)-
E*I*tan(phi/180*pi)/K3.*(2*cos(phi/180*pi)/K3-K2));
P=2*F./D./p./tan(phi/180*pi)*10^6;
plot(D+2*d0,P)
%%%%%%%%%
Ew=0.77;C0=32;
C=(D+2*d0)*pi;
ee=C/C0-1;
pw=4*Ew*ee*2./L./(D+2*d0)*10^6;
hold on
plot (D+2*d0,pw)
for i=1:1:jd;
    if (pw(i+1)-P(i+1))*(pw(i)-P(i))<=0;
        nn=i;
        break;
    end
end
D1=D(nn);
Dmax=D1+2*d0;
phi1=acos(cos(phi0/180*pi)*D1/Dm)/pi*180;
p1=tan(phi1/180*pi)*pi.*D1;
E=7761;G=E/2.7;
K1=sin(2*phi1/180*pi)/D1; K2=2*(cos(phi1/180*pi))^2/D1; K3=D1/cos(phi1/180*pi);
F1=2*n*(G*2*I*cos(phi/180*pi)/K3.*(2*sin(phi/180*pi)/K3-K1)-
E*I*tan(phi/180*pi)/K3.*(2*cos(phi/180*pi)/K3-K2));
P1=2*F1./D./p./tan(phi/180*pi)*10^6;
```

```
for i=1:1:jd;
    if(pw(i+1)-P1(i+1))*(pw(i)-P1(i))<=0;
        nn=i;
        break;
    end
end
D2=D(nn);
Dmin=D2+d0*2;
plot(D+2*d0,P1)
axis([12,26,0,3000])
```

中文大摘要

器械通过口腔、肛门、阴道等人体自然孔口到达病灶并完成相关操作的新型自然腔道手术因创口微小（甚至无创），具有疼痛轻、恢复快、住院时间短和术后不易感染等优点，近些年得到了快速的发展。其中，经口腔-食道的入路由于良好的清洁性、通用性及心理可接受性，被认为最具有研究与应用价值。为顺利完成自然腔道手术，其器械需要具备足够的刚度以保障稳定性与操作力输出，同时也需要具有一定的柔性以适应狭长曲折的人体入路环境。设计出高性能的自然腔道器械是该手术走向临床的必经之路。

柔性会使器械的刚度降低，造成稳定性与操作力问题，可使用器械臂对手术器械进行导引与支撑来解决。手术前，首先将器械臂插入人体腔道中；到达病变处后，手术器械再由器械臂内腔进入并开始手术操作；手术结束后，依次撤出手术器械及器械臂。一方面，器械臂在插入和撤出过程中，需具有较小径向尺寸、良好柔顺性，以通过狭小曲折的腔体并避免组织损伤，从而减少患者不适感。另一方面，器械臂到达病灶处后，需呈现大轮廓和高刚度，为后续手术器械提供充足空间及有效支撑。因此，为了同时满足这两方面的要求，需要设计一款具有可控刚度、可调尺度的器械臂。

目前，国内外学者已提出几种变刚度器械臂设计方案。（1）丝驱动法：调整丝张紧力以控制离散关节间的相互作用力，进而改变整体刚度。然而，过大的张紧力要求结构有足够的承载力，因而难以制成紧凑结构。（2）采用相变材料制作器械臂来实现刚度转化。因使用热响应型材料，响应时间是设计时需要额外考虑的因素。（3）颗粒阻塞法，即离散颗粒在气压作用下运动相互限制方法。该设计方案常需要足够量的颗粒，占用体积较大，降低可提供给后续器械的空间。（4）借助流体压强控制摩擦力、型锁合力的设计方法。其中采用负压的方法更是具有响应快、安全性高的特点，具有更好的应用前景与价值。尽管上述各设计方案实现了刚度可控，但其自身轮廓不可调，仍不能满足器械臂在尺寸设计上的需求。

作为一种典型的折展结构，管状编织结构由多股螺旋线交错形成，其具有柔顺性好、径向折展性佳、结构稳定等优点，已被广泛应用于血管支架、食道支架、人工肌肉、爬行机器人等领域。该结构因可改变几何尺寸，有望作为基体结构设计成刚度和尺度均可调的折展式变刚度器械臂。编织式支架与器械臂在功能上有相似之处，均需要通过复杂的腔道环境到达体腔内部并完成径向展开。现有的支架展开方法主要分为两类：（1）主动展开式：用超弹合金丝制作的支架被压缩在细导管中并伸入人体，到达指定位置后从导管中释放并自然弹开；（2）被动

撑开式：向支架内部放置气球，在病灶处向气球内部充气来撑起支架。这两种方法虽都能改变几何尺寸并完成展开过程，但无法实现结构径向的收缩，不便于器械臂的撤出，因而不能直接用于器械臂的设计中。

因此，本文旨在以编织结构为基体，设计具有刚度可控、直径双向可调的自然腔道手术用器械臂，并对其进行性能分析与样机测试。根据编织结构已知特性以及自然腔道手术应用环境，若将编织结构用作器械臂骨架，可能存在以下失效模式。首先为折展性能不足，即器械臂无法呈现足够的大直径来为后续器械提供空间。其次，编织结构在通过拐角处发生轮廓垮塌，使径向尺寸受损减小。再次，编织结构轴向刚度低，在轴向阻力下可能提前展开，增加继续插入阻力。最后，不充足的变刚度效果会导致刚态下的抗弯刚度、径向刚度不足，造成器械臂对器械的支撑不足或被径向压垮。以上的潜在失效模式将指引本文分析工作的展开。首先，对用作骨架的编织结构进行力学分析，研究其折展特性、弯曲行为及编织模式，建立其面向器械臂应用的力学理论体系。其次，提出负压控制的器械臂刚度调控方案，并对其抗弯刚度、径向刚度的提升机制进行揭示。再次，设计器械臂直径双向驱动方法，建立其直径变换范围的理论计算公式，并研究其热响应特性。最后，提出该编织式器械臂的设计准则，并据此开发器械臂样机并进行演示实验。

根据上述研究内容，本论文章节设置如下：

第二章对用作器械臂骨架的编织结构的力学性能进行分析，建立面向器械臂设计的编织结构力学理论框架。

研究了编织结构的径向折展特性。基于 *Abaqus* 有限元软件并采用欧拉梁单元，建立了编织结构的数值仿真模型。采用实验及数值仿真方法，分析编织结构在轴向拉力作用下的形变及受力规律。根据直径变化与所施加驱动力间的映射关系，并考虑丝线间几何约束及驱动力大小限制，得到适应手术应用环境的实际直径可达区间，最大最小直径比约为 1:0.37。

分析了编织结构的弯曲行为。已知编织结构在大曲率弯曲时，轴向中间截面可能会发生垮塌，因而无法提供完整通路。采用实验及数值仿真方法分析其形变规律，确定关键位置编织丝，并发现形变过程中存在临界弯曲角度，当变形量超过该值后垮塌现象明显加剧；基于数值仿真方法进行正交试验，确定编织角度为垮塌行为最关键影响因素，编织股数次之，而其余参数影响不显著；着重对编织角度的影响进行分析，发现在编织股数为 12 股的条件下，小于 48.5º 的编织角度可保证基本完整的弯曲轮廓。

提出了一种混合编织模式，实现轴向刚度的提升。该编织模式下，左右旋编织丝采用不同的编织角度，在轴向力作用下两方向编织丝的变形不协调，进而增加结构内应变能的积聚、实现刚度的提升。对多种混合比的编织结构进行轴向拉

伸测试，根据实验结果，混合编织结构的轴向刚度提升了 57.12%。此外，通过数值仿真，发现混合编织角度增加了编织丝交叉点处的接触力，限制了编织丝的形变，进而导致应力的增大。该结果进一步验证了轴向刚度提升机制的理论分析模型。此外，对混合编织结构弯曲性能进行数值仿真分析，发现其与普通编织结构有接近的弯曲刚度与变形模态，混合编织模式不会减损结构的弯曲性能。

第三章提出了一种变刚度设计方案，建立所使用的丝、膜间受力模型，揭示了器械臂的抗弯刚度、径向刚度的提升机制。

变刚度设计方案：将编织结构作为器械臂骨架并对其进行封装，使密封膜包覆于结构内外表面并形成密封腔，构成编织式变刚度器械臂。对密封腔进行抽气，使其内部内形成负压。外界大气压将薄膜压紧于编织结构表面，薄膜与编织线间摩擦力限制两者间的相对运动，进而实现整体结构的刚度提升。调整负压值可改变膜与丝之间的摩擦作用的大小，实现刚度的无级调控。

采用实验、数值仿真及理论建模方法研究了器械臂的抗弯刚度。设计可将拉力转化为纯弯矩的加载装置，并在水平拉力平台上对器械臂加载；在编织结构数值模型中添加内外薄膜，并施加均匀压强模拟负压，得到器械臂的数值仿真模型。实验结果表明，刚态下器械臂割线抗弯刚度提升至柔态时的 6.85 倍。器械臂在实验及数值仿真中呈现相同的变形模态，弯矩-转角曲线呈现相同趋势，弯曲角度为 60 度时刚柔两态下力矩结果的误差为 14.03%和 8.95%，实验与数值仿真相互验证。根据数值仿真结果总结器械臂形变规律，并提出理论模型假设条件：（1）编织骨架变形为纯弯曲；（2）膜只承受张力；（3）膜张力较小时，摩擦力平衡膜张力；（4）膜张力超过摩擦力时，丝、膜之间出现滑动。根据此假设及编织结构变形机理，建立丝-膜力学模型，并基于能量法推导出器械臂抗弯刚度显式计算表达式。理论刚度计算结果与实验结果误差为 4.85%，验证理论模型的准确性。基于理论模型进行参数分析，发现提升摩擦力及膜刚度是提升器械臂刚态刚度的最有效手段，而编织结构参数更适于柔态刚度的调控。

采用实验与数值仿真方法，研究器械臂在侧向载荷下的径向刚度。实验结果表明，刚态下器械臂径向刚度提升至柔态时的 3.9 倍。基于数值仿真，器械臂的刚度提升主要依赖于以下两种机制。其一，膜对编织骨架的作用力限制了交叉点处编织丝的相对转动，增加了结构应变能；其二，丝、膜间的相对滑动形成大量的摩擦耗散能。此外，对器械臂的参数分析表明，更大的杨氏模量、丝径、编织股数、薄膜刚度、摩擦力，及更小的编织角，利于器械臂径向刚度的提升。

第四章提出了双向变直径驱动设计方法，研究器械臂骨架的变直径能力，建立了直径范围计算式，同时，基于传热学原理，分析了器械臂的热响应行为。

变直径设计：采用单程形状记忆合金丝制作编织结构。进行热处理使编织结构记忆形状为具有大直径的径向展开状。编织结构外表面沿轴向均匀布置有橡胶

圈以提供回复力。室温下，材料刚度低，在橡胶圈的作用下结构呈现小直径状态；加热后，编织结构趋于所记忆形状，且刚度变大，结构可承受橡胶圈作用力，整体呈现大直径状态；冷却后，材料变软，结构在橡胶圈的作用下恢复到小直径状态。

采用实验与理论方法研究器械臂骨架的变直径范围。首先，制作了器械臂骨架物理模型并进行实验。选取镍钛形状记忆合金丝并将其定型于大直径螺旋状态，在其外表面套上铁氟龙毛细管作为绝缘层；缠绕制成编织骨架并将各股编织丝首尾相连，形成单一通路；在骨架外表面布置橡胶圈；通过电热驱动实现器械臂径向展开，自然冷却后器械臂径向折叠；对器械臂持续通电、断电自然冷却，测得直径变化范围为 14.7-21.4mm。其次，建立变直径范围的理论计算式。忽略相变过程的影响，将两种相态下的形状记忆材料视为具有不同弹性模量的线弹性材料。根据已知的编织结构力学公式和胡克定律，确定编织骨架以及橡胶圈的直径-载荷映射关系，建立了编织骨架-橡胶圈交互力学模型，确定了器械臂直径变化范围的理论计算公式，从理论上揭示了变直径机理。计算求得实验参数下的器械臂直径变化范围为 13.9-21.7mm，最小及最大直径误差分别为 5.44%和 1.40%，验证了理论模型的准确性。进一步地，利用所得理论计算式对橡胶圈的布置进行参数分析，发现在优化的参数下，最大、最小直径比可达 1.6 倍。

对器械臂的热响应进行研究。在悬臂梁力加载条件下测试响应时间，加载过程中开始对器械臂通电，根据力-位移曲线变化趋势确定器械臂的展开响应时间为 20s。基于传热学原理，推导编织丝截面内的稳态温度分布规律，将不同电流下的稳态温度与材料相变温度作对比，确定最小可用电流为 1.1A。建立数值模型研究瞬态温度变化规律，将编织丝到达相变温度所需时间作为展开响应时间，研究不同电流下的响应速度，并将其与实验结果作对比，验证了模型可靠性。基于数值仿真模型，研究用前预热对响应时间影响，发现预热温度越高，响应越迅速，预热至 37 摄氏度时，响应时间可降至 10s 以下。

第五章提出器械臂设计准则并试制物理样机，完成样机演示实验及性能测算，验证器械臂设计的可行性。

结合第二至四章对编织骨架性能、刚柔转化机理、直径双向驱动的研究结论，并基于实际应用要求，提出器械臂的设计准则。归纳出弯曲垮塌、折展极限、器械臂厚度、变刚度范围、变直径范围共五个性能指标，总结出密封膜、负压、形状记忆效应、橡胶圈、编织结构共五个设计对象。建立性能指标与设计对象之间的关联关系并区分其关联强度，实现设计参数间的解耦，并据此确定器械臂各组成部分的设计顺序与依据。

根据上述设计准则，试制样机系统。该系统共包括器械臂样机、自然腔道模型、丝驱动系统、电热系统及负压系统五个部分。器械臂样机采用第四章编织骨

架参数设置及聚四氟乙烯薄膜，折叠时长度为 340mm；自然腔道模型模拟人体食道形状并具有两个明显转角，并固定于支架来模仿患者平躺时食道的位姿；丝驱动系统用于控制器械臂末端摆动；电热系统采用恒流电源，用于热驱动器械臂展开；负压系统用于实现器械臂刚柔转化与形状锁合。

基于变刚度、变尺度的性能特点及控制特征，提出器械臂工作流程，实现这两种可变特性的有机结合。器械臂常态为柔顺、小直径状态，在该状态下插入体腔；通过电热驱动展开至大直径状态；施加负压实现刚度提升并锁住大直径形状，取消电热后器械臂仍保持在大直径刚态，在此状态下可插入后续器械并进行手术操作；术后取消负压，锁形能力丧失，器械臂自动恢复到柔顺、小直径状态并顺利撤出。

利用所设计样机系统进行插入、径向展开、刚化保形、软化折叠、撤出共五部分操作演示，验证了器械臂的可行性。对样机的变刚度、变尺度范围进行测算，并将结果与商业内窥镜指标作对比，验证器械臂可变性能的优越性。根据实验效果及理论分析结果，指出器械臂的局限性，包括热驱动的响应时间与人体安全性、展开过程中的轴向收缩以及转角处未完全展开，讨论了解决或减轻这些问题的方法。

本文致力于折展变刚度器械臂的性能分析与设计方法研究，针对器械臂潜在的失效模式，建立了编织结构的力学行为理论框架；以编织结构为基体，提出了基于负压的刚度转换方法；采用单程形状记忆合金与橡胶圈，实现了器械臂双向折展；根据应用环境要求与器械臂性能特征，提出该器械臂的设计准则并进行样机试制与演示，得到良好的实验效果。

此外，本文的研究工作还可以在如下几方面进行进一步的深入研究：

首先，用于调节直径变化的电热驱动方法，在响应时间和患者安全上存在隐患。因此，需要设计一个具有热反馈的智能控制系统，来精准控制升温范围，以避免产生过多的热量来缩短响应时间、降低最高温度。为建立此系统，一方面，需要研究形状记忆材料的相变过程及编织结构的热动态特性，确立产热量与力响应之间的映射关系。另一方面，也需要考虑密封膜的热稳定性和绝热性。

其次，更强的刚柔转化能力，可更大地提升器械臂的支撑效果，更好地保证后续器械的精准度与操作力输出。根据分析结果，增加编织丝与密封膜之间的摩擦力是提升刚度效果最有效手段。因此，后续将研究增加丝、膜粗糙度的方法。然而，更大的摩擦力使密封膜对骨架形变的影响不能再忽略，因此还需对理论模型进行相应的改进。

再次，编织骨架在实验过程中也表现出来一定的局限性。首先，展开过程中器械臂的轴向长度发生缩短，因此需要同时进行器械臂插入以补偿该缩短量，这

增加了操控难度。将设计新型编织结构或进行参数优化以减少长度损失量。此外，器械臂在转角处出现截面尺寸损失。在压痕和弯曲共同作用下，编织结构垮塌机理更为复杂，且展开过程会使编织角度发生变化，需要提升理论模型来解释编织结构在复杂作用下的弯曲响应行为。

最后，将进行体外操作实验或动物实验以进一步验证器械臂的有效性。对使用和不使用器械臂的实验结果进行比较研究，并探讨器械臂与手术器械之间的相互作用。

关键词：自然腔道手术，器械臂，编织管结构，可变刚度，可变直径，负压方法，形状记忆方法

Publications and Research Projects during PhD's Study

Papers:

Seven journal papers (six SCI indexed, one EI indexed) and one conference paper (EI indexed) have been published. Representative ones are listed as follows.

[1] Shang Z, Ma J, You Z, and Wang S, A foldable manipulator with tunable stiffness based on braided structure [J]. Journal of Biomedical Materials Research Part B-Applied Biomaterials, 2020, 108(2): 316-325.

[2] Shang Z, Ma J, You Z, and Wang S, Lateral indentation of a reinforced braided tube with tunable stiffness [J]. Thin-walled Structures, 2020, 149: 106608.

[3] Shang Z, Wang S, You Z, and Ma J, A hybrid tubular braid with improved longitudinal stiffness for medical catheter [J]. Journal of Mechanics in Medicine and Biology, 2019, 19(3): 1950003.

[4] Shang Z, Ma J, You Z, and Wang S, A braided skeleton surgical manipulator with tunable diameter [C], IEEE/RAS-EMBS International Conference on Biomedical Robotics and Biomechatronics, New York, 2020, 223-228.

[5] Shang Z, Ma J, Li J, Zhang Z, Zhang G, and Wang S, Self-forcing mechanism of the braided tube as a robotic gripper [J], Journal of Mechanisms and Robotics, 2019, 11(5): 051002.

Patents:

Four Chinese patents have been authorized. Three PCT patents and one Chinese patent are in application. Representative ones are listed as follows.

[1] Wang S, Shang Z, Ren X. Expandable serpentine carrier with variable rigidity for natural orifice transluminal endoscopic surgery and method for using same, international application number: PCT/CN2018/088647, PCT patent, international filing date: 2018.05.28.

[2] 王树新，尚祖峰，任旭阳．一种自然腔道手术用可展变刚度蛇形载体，授权号: ZL201710578595.2，发明专利，申请日: 2017.07.17.

[3] 王树新，马家耀，尚祖峰，由衷．一种用于自然腔道手术的折展变刚度器械臂，授权号: ZL201710628109.3，发明专利，申请日: 2017.07.27.

[4] 王树新，刘开元，尚祖峰，李进华．一种用于自然腔道手术的变刚度保护鞘及其应用方法，授权号: ZL201710579699.5，发明专利，申请日: 2017.07.17.

Research Projects Participated in:

[1] 《精准微创手术器械创成与制造基础》, 国家自然科学基金（重大项目）, 项目号: 51290290.

[2] 《面向精准微创手术器械的折展编织机构理论与刚柔转化机理研究》, 国家自然科学基金（面上项目）, 项目号: 51575377.

Acknowledgements

My deepest gratitude goes foremost to my supervisor Prof. Shuxin Wang. In addition to the valuable guidance towards my work, his encouragement really helped me go through my difficult time. His devotion to research also impresses me a lot. What I have learned from him is the most valuable wealth.

I would also like to thank Prof. Jiayao Ma. He helped me in the very details of my work. Appreciations also go to Prof. Jinhua Li and Prof. Yuan Xing. Thanks a lot for the help in both research work and daily matters. Appreciation also goes to Prof. Yan Chen for providing nice research conditions and atmosphere. I appreciate the academic suggestions from Prof. Jianmin Li, Prof. Zhong You and Prof. Hongbo Yu.

Next, I will say thank you to Prof. Lieva Van Langenhove and Dr. Benny Malengier for providing me the chance to study abroad and enjoy the new research atmosphere. The critical thinking, I will never forget. I also thank my colleagues including Ziyuan Li, Hassan Riaz, and Anto Hardianto for their help in work and life.

My colleagues in Medical Lab and MOST Lab also contributed greatly to my work. Apperications go to Liu Ma, Fufu Yang, Guokai Zhang, Xiao Zhang, He Su, Kang Kong, Dezhong Gao, Yuyang Sun, Weng Ma, Xuyang Ren, Rui Peng, Huijuan Feng, Xiangyun Ren, Zhenxuan Hu, Zemin Zhang, Jichao Song, Mengchao Cui, Jianchen Wang, Yuanqian Gao, Yuncheng Cui, Ke Liang, Yingkan Yang, Ze Chen, Huaifeng Zhang, Ruilin Yang, Peng Liu, Xiang Liu and Junjie Gao.

I'd like to thank my teachers from Tianjin University and Nankai University. Appreciations specifically go to Fei Guo, Weimin Ge, Lu Feng, Hulun Guo, Huayue Zhang, Lei Wang, Na Zhao, Yurong Lin, Shengmin Zhao, Zengwei Zhang, Yimin Song.

I'd like to thank my teachers from Anshan No.1 Middle School. Appreciations specially go to Shihai Liu, Lin Wang, Gangqing Yu, Ling Chen, Liang Dong, Shukai Cao, Kan Gao and Qi Wang.

I'd like to thank my teachers from Niuzhuang Middle School. Appreciations specially go to Ping Zhang, Chun Tian, Shujie Hou, Hao Zhang, Zhiqiang Ma, Guang Li, Junbo Gong, Dezhong Pang and Sukun Shi. They helped me walk out from the small town.

It is long ago but I can still remember my life in Beiguan Primary School. Thank my teachers including Mingming Zhang, Baicang Li, Lixia Jiang and Yuping Zhang.

Thank my friends who showed care to my safety during the global coronavirus pandemic. Appreciations specially go to Renna Li, Minghe Fan, Jiayao Ma, Wenzhao Lin, Xinpei Liu, Yilin Pan, Yugang Ren, Benyu Ge, Yuan Xing, Yuncheng Cui and Ling.

Thank my parents and Liwei Fan.